Karim Haroud

Band 419

Light Sources and Lasers based on Rare-Earth Doped Fibers: Design and Sensor Applications

UFO Atelier für Gestaltung & Verlag

L'expérience fait l'art, l'inexpérience la fortune. On fait des découvertes en cherchant et des trouvailles par hasard.

Joseph Jouber

Université de Neuchâtel

Institut de Microtechnique

Light Sources and Lasers based on Rare-Earth Doped Fibers: Design and Sensor Applications

Thèse

Présentée à la faculté des sciences
pour obtenir le grade de docteur ès sciences
par

Karim Haroud

Neuchâtel, Avril 2001

UFO Dissertation Band 419

Die Deutsche Bibliothek – CIP-Einheitsaufnahme
Ein Titeldatensatz für diese Publikation ist bei
Der Deutschen Bibliothek erhältlich.

Dissertation der Universität Neuchâtel
Datum der mündlichen Prüfung: 10.04.2001
Referenten: Prof. Dr. R. Dändliker
Prof. Dr. H.-P. Herzig
Prof. Dr. W. Lüthy
Prof. Dr. R. P. Salathé

UFO Atelier für Gestaltung & Verlag GbR · D-78476 Allensbach
Internet: www.ufo-verlag.de

ISBN 3-935511-20-5

IMPRIMATUR POUR LA THESE

Light Sources and Lasers based on Rare-Earth Doped Fibers: Design and Sensor Applications

de M. Karim Haroud

UNIVERSITE DE NEUCHATEL

FACULTE DES SCIENCES

La Faculté des sciences de l'Université de Neuchâtel sur le rapport des membres du jury,

MM. R. Dändliker (directeur de thèse), H.P. Herzig, W. Lüthy (Berne) et R.P. Salathé (Lausanne)

autorise l'impression de la présente thèse.

Neuchâtel, le 11 mars 2002

Le doyen:

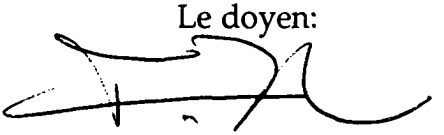

F. Zwahlen

Abstract

In this thesis, broadband superfluorescent fiber-laser sources and fiber laser sensors are investigated. Basic materials for understanding light amplification and light interaction in active fibers are provided first. The theoretical model of gain is focused on four-level system, for which predictions of the fluorescence emission spectra are illustrated in an example.

Low temporal coherence or broadband light sources are useful sources for white light interferometry and for addressing distributed sensor systems. The required broad spectrum is difficult to obtain from single doped fibers because of the narrowing introduced by the amplification of the spontaneous emission. The use of different types of doped fiber, besides spectral filtering are interesting approaches which overcome partially the unwanted effect of the narrowing. Practical examples using neodymium (Nd^{3+}), ytterbium (Yb^{3+}) and erbium (Er^{3+}) doped fiber are illustrated in double pass or in a dual-stage configuration. Such cascaded configurations generate emission spectra that profit of combined amplification effects, which could not be obtained with a mere superposition of independent contributions.

Sensing is a domain that requires narrow line sources. Fiber Fabry-Pérot lasers are realized first and the experimental results are compared with theoretical prediction in terms of efficiency loss, and polarization. Fiber laser sensors employing fiber Bragg gratings (FBGs) have been a subject of considerable interest because of their inherent advantages such as their frequency-encoded output, potential for high resolution, high signal to noise ratio and small diameter in-line design. Commonly, fiber lasers operate on two orthogonal polarizations. In the so-called polarimetric fiber laser sensor, the parameter to be measured changes the birefringence of the fiber laser. The associated differential phase shift can be observed as a change in the beat frequencies of the orthogonal longitudinal laser modes. Polarimetric fiber laser sensors have been realized to that end. Finally, the effect of the chromatic dispersion of the FBGs on the beat signal is investigated. It is shown experimentally and theoretically that the wavelength dependent phase shift of a chirped FBG can be employed in a polarimetric Fabry-Pérot fiber laser to simultaneously measure the pressure and the temperature.

Table of contents

1 Introduction

Although the studies on light date back almost 500 years, the latest spectacular scientific advancements have been inextricably linked to the first successful laser action in the visible spectrum, constructed by Maiman in 1960 [1]. The laser consisted of a ruby crystal surrounded by a helicoidal flash. The ruby cylinder ends were polished, and coated by evaporated silver, forming a Fabry-Pérot cavity. Infrared and visible laser action has earlier been predicted in a paper titled "Infrared and Optical Masers," published in 1958 by Arthure L. Schawlow and Charles H. Townes.

A short while after the first laser, another optical laser, operating at 1.06 μm, was demonstrated in 1961, with a trivalent Neodymium in alkali-alkaline earth silicate [2]. Many different rare-earth ions implemented in many different substrates as Yttrium Aluminum Garnet (YAG), glass, CaF2, have been tried successfully as laser materials. Nowadays the concept of stimulated emission postulated by Albert Einstein in 1917 is recognized as a fundamental concept in the field of the quantum electronics and lasers.

The discovery of the rare-earth elements starts in 1803, with the cerium and the remainder of the elements was identified over almost the next century. At that time, one could never imagine the variety of different areas of application, these elements could find. Ytterby is a small village near Vaxholm, in Stockholm's archipelago, which has play an important role in the history of rare earth element, since many of them were discovered there and were named after Ytterby; Ytterbium, Yttrium, Terbium, and Erbium, while Holmium ensues from the Latin of Stockholm.

Few years after the invention of the laser, C. J. Koester and E. Snitzer carry out experiments between 1963 and 1964, and have shown the first wave-guide amplifier [3]. These experiments used a neodymium (Nd)-doped glass with a core-cladding wave-guide structure, which enables light confinement.

Since the 60's, worldwide efforts have been spread out to reduce optical fiber transmission losses. Modified chemical vapor deposition (MCVD) technology, developed by Mac Chesney and his Bell Labs colleague P.B. O'Connor in the early 1970s, made possible the fabrication of very low-loss fibers [4]. MCVD involves heating chemical vapors and oxygen that are flowing inside a silica glass tube to deposit an

inner glass layer that is fused with the outer layer of higher index of refraction. The tube is collapsed forming the so-called preform. The preform is heated again and stretched to make up the core of the hair-thin, which strands and guides the photonic signals. This new development has marked the outset of a new era of information and communication. Today, optical fiber communication technology stands out as an inescapable transmission tool for this information. Another tremendous breakthrough in optical fiber communication technology came in 1987, when a group from Southampton University reported a high-gain fiber amplifier operating at 1.55 μm [5].

Studies of quantum mechanical properties of the material have led to a more accurate description of the behavior of atoms and molecules. These studies have demonstrated the good potential of oxide and fluoride hosts, incorporating other rare-earth ions, to generate laser emission in a wide range of wavelength, starting from 0.45 μm to nearly 3.5 μm.

Background

Beside telecommunication aspects, where the well-established Er^{3+}-doped fiber amplifiers operate in the important third telecommunication window, other efficient radiative transitions provide now very useful light sources. These sources are optically pumped and operated by amplification of stimulated emission (ASE). They are known as superfluorescent fiber sources (SFS) and exhibit broad emission even at relatively high pump power. Currently, doped-fiber ASE emissions are challenging broadband semiconductor superluminescent diodes as the source of choice for many commercially important applications. They are used for optical fiber gyroscopes, medical tomography and for distributed fiber Bragg grating (FBG) sensors as addressing broadband source.

Fiber Bragg gratings are, without doubt, important fiber-optical devices, which have boosted the telecommunication and the sensor market. They were first reported in the late 1970s, but have only recently begun to be commercially important. In the future, FBGs will play a important role in sensors market, which will overtake the networks sector in terms of growth rate [6]. Now, FBGs act as remote sensors in so-called smart structures, where FBGs are embedded in concrete forms, such as bridges and buildings. They also find applications in harsh environment, such as oilfield monitoring in petrochemical industry.

Combined with doped fibers, fiber Bragg grating reflectors allow single frequency and single polarization mode operation in so-called distributed feed-back (DFB) fiber lasers, with a current record in the kilohertz range. The DFB fiber lasers with strongly-doped Ytterbium (Yb^{3+}) fibers, provide efficient and powerful emission at 1 μm and could replace, for some applications, the well know Nd:YAG bulk crystal ring lasers.

Thesis outline

The present dissertation is organized as follows:

Chapter 2 provides the basic materials for understanding the principle of light amplification and light interaction in active fiber devices. The theoretical model of gain is focused on four-level system, for which predictions of fluorescence emission are illustrated in an example.

Chapter 3 proposes interesting approaches with which the fluorescent emission can be enlarged. We discuss the possibility to combine different types of doped fibers and to use spectral filtering within the fiber source.

Chapter 4 provides background information of birefringence property of doped fiber and theoretical modeling of fiber Bragg gratings (FBG) used for the elaboration of a single frequency (single polarization) fiber Fabry-Pérot laser source. Experimental results are compared with theoretical predictions, in terms of efficiency, loss, and polarization. In addition, the emission linewidth of a distributed feedback (DFB) laser is also investigated under different pumping conditions.

The discrimination between the effect of strain (or pressure) and temperature on the resonance wavelength of FBGs is a subject of considerable interest with regard to FBG sensors, and a number of approaches to discriminating between these two effects have been proposed. We discuss in chapter 5 the application of a Fabry-Pérot fiber laser as a simultaneous pressure and temperature sensor. A narrow linewidth uniform-FBG and a large linewidth chirped-FBG form the cavity. This configuration enables simultaneous pressure and temperature measurement with a direct RF frequency readout by measuring simultaneously the axial mode and the polarization mode beat frequencies.

This work was supported by the Swiss Priority Program Optics II (PPOII) in collaboration with Contraves Space AG, Zürich, and the ABB Corporate Research Center, Baden-Dättwil.

2 Basic concepts of doped fiber lasers

Unlike the following chapters, which treat the actual work of this thesis, this chapter provides a basic introduction to rare-earth ion-doped glass fiber lasers and amplifiers. We describe first the formalism used for modeling light amplification in the particular case of a four-level laser system. This model, which corresponds to a simplified representation of the neodymium (Nd^{3+})-glass system, can be straightforwardly applied to a three-level system representing for instance, the erbium (Er^{3+})-glass system. Ytterbium (Yb^{3+}) is another important and widely used rare-earth element, which can be described by a two- and quasi-three-level system.

This first section is completed with an example comparing theoretical and experimental amplified stimulated emission (ASE) spectra, for different values of pump power. Modeling light amplification requires the accurate knowledge of physical and chemical parameters of the fiber, like absorption/emission cross-sections, dopant distribution profiles and concentrations. The methods and procedures for the characterization of these parameters are not developed in this chapter, since they are well treated in many books dealing with doped fiber lasers and amplifiers [7] [8] [9].

The second section of this chapter presents the energy diagrams and the transitions for the Nd^{3+}, Er^{3+}, Yb^{3+}, and Tm^{3+} -doped silica-glass fiber. Up-conversion transitions, which can occur efficiently at 550 nm and 490 nm in Er^{3+} and the praseodymium (Pr^{3+}) ions in fluoride host material, will not be considered in this thesis dissertation.

2.1 Theoretical modeling of light amplification in single-mode fibers

Modeling light amplification using population dynamics analysis in the so-called atomic rate equations is presented in his section. In addition, a propagation equation is established to describe the pump and signal propagation down the fiber, taking into account the pump and signal mode overlap. The effect of the pump and signal modes overlap with the dopant distribution in the fiber has been proposed by Digonet et al. [10] and they have extended later this concept to superfluorescent fiber lasers in [11].

Today, a relatively large number of papers are devoted, not surprisingly, to the analysis and modeling of Er^{3+}-doped fiber amplifiers [8], and dedicated software is commercially available for fiber amplifiers and lasers [12]. The model proposed in this section treats a four-level system, which is well adapted for the specific case of Nd^{3+}-doped fibers.

2.1.1 Basic considerations

The spectral absorption and emission properties of rare-earth elements in glass host materials differ slightly from those in crystals, since glasses have by definition a random distribution of the internal electric field. This electric field splits each energy level, which is characterized by a total momentum J, into different sets of degeneracy sublevels. This Stark effect is schematically shown in Fig. 2.1 for two energy levels

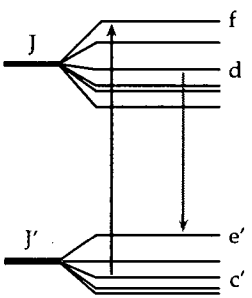

Fig. 2.1: Stark splitting of two energy levels.

Although the position of stark levels in rare earth-doped glass and the associated transition cross section can be accurately determined by low temperature spectroscopy [13], the resultant, of the spontaneous and the stimulated emission and pumping rates, are in general experimentally measured from fiber samples [14] [15]. Despite the fact that these measured parameters correspond to averaged quantities, they provide in most cases a sufficiently precise description of the laser systems allowing good theoretical prediction. These measured parameters may not be sufficiently accurate to model systems where radiation transitions are predominantly inhomogeneously broadened. Nevertheless, it has been established from experimental results, that in most cases, fiber lasers and amplifiers behave like having a

homogeneously broadened gain. It is indeed reasonable to think that in glass hosts, the large number of Stark levels are equally populated, and tend to overlap, forming a quasi-continuum transition. Based on this remark, the model developed in the next section assumes homogeneous broadening of the gain medium.

2.1.2 Rate equations for a four-level system

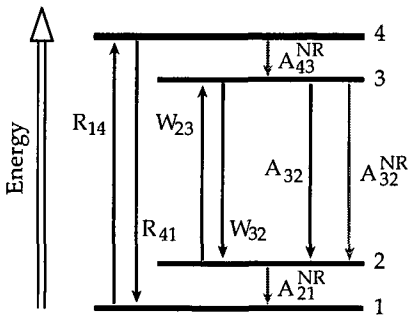

Fig. 2.2: Energy level diagram of a basic four-level laser system

The rate equations describe the rates of change of the population densities as a result of absorption and emission rates. From the basic four-level energy diagram in Fig. 2.2 we define: R_{14} and R_{41}, the stimulated absorption and emission rate for the pump transition; W_{23} and W_{32}, the stimulated absorption and emission rate for the signal transition; A_{32}, A_{32}^{NR}, A_{43}^{NR} and A_{21}^{NR}, the radiative and nonradiative spontaneous emission rate, respectively.

Let N_1, N_2, N_3 and N_4 be the population density in the energy state 1, 2, 3 and 4, respectively. The rate equations for these population densities are then

$$\frac{dN_1}{dt} = R_{41}N_4 + A_{21}^{NR}N_2 - R_{14}N_1, \tag{2.1}$$

$$\frac{dN_2}{dt} = W_{32}N_3 + A_{32}N_3 + A_{32}^{NR}N_3 - W_{23}N_2 - A_{21}^{NR}N_2, \tag{2.2}$$

$$\frac{dN_3}{dt} = W_{23}N_2 - A_{32}N_3 - A_{32}^{NR}N_3 - W_{32}N_3 + A_{43}^{NR}N_4, \tag{2.3}$$

$$\frac{dN_4}{dt} = R_{14}N_1 - R_{41}N_4 - A_{43}^{NR}N_4. \tag{2.4}$$

In the steady state regime, the populations are constant, i.e. $dN_i/dt = 0$ for i=1, 2, 3 and 4. In most four-level systems, the nonradiative decay component in the transition between 3 and 2 is typically negligible $A_{3x} >> A_{3x}^{NR}$, x =1,2, and $A_{32} >> A_{31}$. Since the sum of the radiative and non-radiative decay rates from the level 3 is related to the lifetime of that excited level, by

$$\tau_{32} = \left(A_{32} + A_{32}^{NR} + A_{31} + A_{31}^{NR}\right)^{-1}, \tag{2.5}$$

the lifetime of the transition becomes $\tau_{32} \cong \left(A_{32}\right)^{-1} = \tau_{fluo}$, where τ_{fluo} is the fluorescence lifetime.

Solving Eqs. (2.1) and (2.4), for N_1 and N_3 yields

$$N_1 = \rho \frac{\left(W_{32}\tau_{fluo}+1\right)\left(\frac{R_{41}}{A_{43}^{NR}}+1\right)}{\left(\frac{W_{23}+W_{32}+A_{32}}{A_{21}^{NR}}+1\right)R_{14}\tau_{fluo}+\left(W_{32}\tau_{fluo}+1\right)\left(\frac{R_{14}+R_{41}}{A_{43}^{NR}}+1\right)}, \tag{2.6}$$

$$N_3 = \rho \frac{R_{14}\tau_{fluo}}{\left(\frac{W_{23}+W_{32}+A_{32}}{A_{21}^{NR}}+1\right)R_{14}\tau_{fluo}+\left(W_{32}\tau_{fluo}+1\right)\left(\frac{R_{14}+R_{41}}{A_{43}^{NR}}+1\right)}, \tag{2.7}$$

with the total population density $\rho = N_1 + N_2 + N_3 + N_4$. It is usually assumed that the non-radiative decay rates A_{43}^{NR} and A_{21}^{NR} predominate the pumping rates $R_{14,41}$ and the stimulated and the spontaneous rates $W_{23,32}$ and A_{32}. This assumption leads to the simplified versions

$$N_1 = \rho \frac{W_{32}\tau_{fluo}+1}{\left(W_{32}+R_{14}\right)\tau_{fluo}+1}, \tag{2.8}$$

$$N_3 = \rho \frac{R_{14}\tau_{fluo}}{\left(W_{32}+R_{14}\right)\tau_{fluo}+1}, \tag{2.9}$$

of Eqs. (2.6) and (2.7).

It is straightforward to find from the above result that N_2 and N_4 are under these assumptions equal to zero. This means that the levels 2 and 4, characterized by an extremely short lifetime, are promptly depopulated.

Mode envelope

It is useful to define both pump and signal light intensity distribution over the finite transverse plane of the fiber core. Following Desurvire [8], we define the intensity distribution $I_{s,p}(r,\theta)$ of the optical power for the signal (P_s) and the pump (P_p) in the guided modes of the fiber as

$$I_{s,p} = P_{s,p}\frac{\psi_{s,p}(r,\theta)}{\int_S \psi_{s,p}(r,\theta)rdrd\theta} = P_{s,p}\overline{\psi}_{s,p}(r,\theta), \tag{2.10}$$

where (r,θ) represent the transverse cylindrical coordinates, $\psi_{s,p}$ the mode envelopes, and $\overline{\psi}_{s,p}$ the normalized mode envelopes for the signal and the pump.

We consider in the following weakly guiding step-index fibers. The fiber modes are well approximated by the *LP* solutions, defined through Bessel functions [16]. For a

single-mode fiber, the mode profiles are therefore given by the LP_{01} power-mode envelope [8]

$$\psi_{01}(\lambda_{s,p},r)=\begin{cases} J_0^2\left(\mathcal{U}_{s,p}\dfrac{r}{a}\right) & \text{for } r\le a \\ \dfrac{K_0^2\left(\mathcal{W}_{s,p}\dfrac{r}{a}\right)}{K_0^2\left(\mathcal{W}_{s,p}\right)}J_0^2\left(\mathcal{U}_{s,p}\right) & \text{for } r>a, \end{cases} \tag{2.11}$$

where J_0 and K_0 are the zero order Bessel and Hankel functions, respectively. a is the core radius, $\mathcal{U}$ and $\mathcal{W}$, are the core and the cladding modal parameters defined in [16] with the waveguide parameter $V^2=(kaNA)^2=\mathcal{U}^2+\mathcal{W}^2$. k is the wave number and NA the numerical aperture. The effective mode power radius corresponding to the Bessel solution is defined as

$$\omega_{s,p}^{01}=\left\{\frac{1}{\pi}\int_0^{2\pi}\int_0^{\infty}\psi_{s,p}^{01}(r)rdrd\theta\right\}^{\frac{1}{2}}=\left\{2\int_0^{\infty}\psi_{s,p}^{01}(r)rdr\right\}^{\frac{1}{2}}, \tag{2.12}$$

from which we find

$$\omega_{s,p}=\frac{V_{s,p}K_1\left(\mathcal{W}_{s,p}\right)}{\mathcal{U}_{s,p}K_0\left(\mathcal{W}_{s,p}\right)}J_o\left(\mathcal{U}_{s,p}\right). \tag{2.13}$$

Finally, Eq. (2.10) for the intensity distributions becomes

$$I_{s,p}=P_{s,p}\frac{\psi_{s,p}(r,\theta)}{\pi\omega_{s,p}^2}=P_{s,p}\overline{\psi}_{s,p}(r,\theta). \tag{2.14}$$

Fluorescence lineshape and cross-section

The concept of stimulated emission or absorption cross-section is introduced to describe the strength of the atomic transitions. Since the transitions are not strictly monochromatic, we define a function describing the spectral distribution of the emitted intensity. This function is referred to as the lineshape function g(ν) of the atomic transition and it is normalized according to

$$\int_0^{+\infty}g(\nu)d\nu=1, \tag{2.15}$$

where ν is the optical frequency. The value g(ν)dν can be considered as the differential spontaneous decay probability of a photon in the frequency interval between ν and ν+dν .

The fundamental result of the *Judd-Ofelt* theory [17] allows determining the cross-section from the experimental characterization of the absorption transition and the spontaneous emission probability, i.e. the lifetime. The ratio between the measured fluorescent lifetime and the spontaneous radiative lifetime, also called branching ratio, is given in [18] for some Nd^{3+}-doped glass fibers. If we assume that the measured lifetime τ_{mes} is essentially the spontaneous radiative lifetime τ_{spont}, so that $\tau_{mes} = \tau_{spont} = \tau_{fluo}$, we can deduce for the emission cross-section $\sigma_s(\lambda)$ that

$$\int_{band} \sigma_s(\lambda)d\lambda = \frac{\langle\lambda\rangle^4}{8\pi n^2 c\tau_{fluo}} = \sigma_s^{peak}\Delta\lambda_s^{eff}. \tag{2.16}$$

The Eq. (2.16), which gives a relation between the peak cross-section σ_s^{peak} and the experimental values of the fluorescent lifetime τ_{fluo}, the mean wavelength $\langle\lambda\rangle$ and the effective line width $\Delta\lambda_s^{eff}$, is referred to as the *Fuchtbauer-Ladenburg* relation [19].

If we assume that the emission cross section has the same lineshape as the fluorescent emission spectrum $f(\lambda)$, we can define the normalized lineshape function

$$g_s(\lambda) = \frac{f(\lambda)}{\int_0^{+\infty} f(\lambda)d\lambda} = \frac{f(\lambda)}{f\left(\lambda^{peak}\right)\Delta\lambda^{eff}}. \tag{2.17}$$

Combining Eqs. (2.16) and (2.17) we find

$$\sigma_s(\lambda) = \sigma_s^{peak}\frac{f(\lambda)}{f\left(\lambda^{peak}\right)}. \tag{2.18}$$

From Eqs. (2.16) and (2.18), the lineshape function becomes

$$g_s(\nu) = \frac{8\pi n^2\tau_{fluo}}{\lambda_s^2}\sigma_s(\nu). \tag{2.19}$$

Absorption and emission rates

We shall express now the absorption and emission rates in explicit terms of pump and signal intensity distribution. The stimulated emission rate W_{32} at the fiber coordinate (r,z), where z is axial coordinate, is related to the signal intensity I_s(r,z) by ([19], pp. 168)

$$W_{32}(r,z,\nu) = \frac{\lambda_s^2}{8\pi n^2 h\nu_s\tau_{fluo}} I_s(r,z)g_s(\nu). \tag{2.20}$$

Using Eq. (2.19), we get from Eq. (2.20)

$$W_{32}(r,z) = \frac{I_s(r,z)}{h\nu_s}\sigma_s. \tag{2.21}$$

The dependence of the emission cross-section on the optical frequency through $\sigma_s = \sigma_s(\nu)$ will be implicitly considered in the following. Using Eq. (2.14), we can express the stimulated rate in terms of the optical power $P_s(z)$ coupled into the signal mode, with envelope $\psi_s(r)$ and radius ω_s, as

$$W_{32}(r,z) = \frac{P_s(z)\psi_s(r)}{h\upsilon_s \pi\omega_s^2}\sigma_s = \frac{P_s(z)\overline{\psi}_s(r)}{h\upsilon_s}\sigma_s. \tag{2.22}$$

Similarly, we introduce for the pumping rate

$$R_{14}(r,z) = \frac{P_p(z)\psi_p(r)}{h\upsilon_p \pi\omega_p^2}\sigma_p = \frac{P_p(z)\overline{\psi}_p(r)}{h\upsilon_p}\sigma_p, \tag{2.23}$$

where $\sigma_p = \sigma_p(\nu)$ is the pump cross-section and $P_p(z)$ is the power coupled into the pump mode with envelope $\psi_p(r)$ and radius ω_p.

Intensity saturation

We consider now the interaction of the signal wave with the amplifying medium. For strong enough input-signal intensity, the stimulated emission rate may dominates the pumping rate and thus reduces the population difference, i.e. the gain of the laser transition. This effect is referred to as gain saturation, and sometimes also as self-saturation, if the saturating signal is the ASE itself.

The derivation of the saturation intensities is treated in [20] (pp. 176), and [21] (pp. 206). For a basic laser system with homogeneous atomic transition, the saturation intensities are generally defined as

$$I_{s,p}^{sat} = \frac{h\nu_{s,p}}{\sigma_{s,p}\tau_{fluo}}, \tag{2.24}$$

from which we can define the saturation power as $P_{s,p}^{sat} = I_{s,p}^{sat}\pi\omega_{s,p}^2$. With these definitions, we can reformulate Eqs. (2.22) and (2.23) of the emission and absorption rate as

$$W_{32}(r,z)\tau_{fluo} = \frac{P_s(z)}{P_s^{sat}}\psi_s(r), \tag{2.25}$$

$$R_{14}(r,z)\tau_{fluo} = \frac{P_p(z)}{P_p^{sat}}\psi_p(r). \tag{2.26}$$

Substituting Eqs (2.25) and (2.26) in (2.8) and (2.9), we get for the population density in level 1

$$N_1(r) = \rho\frac{1+s(z)\psi_s(r)}{1+\left[p(z)\psi_p(r)+s(z)\psi_s(r)\right]}, \tag{2.27}$$

and in level 3

$$N_3(r) = \rho \frac{p(z)\psi_p(r)}{1+\left[p(z)\psi_p(r)+s(z)\psi_s(r)\right]}, \tag{2.28}$$

where $p(z) = P_p(z)/P_p^{sat}$ and $s(z) = P_s(z)/P_s^{sat}$ are introduced as normalized pump and signal power, respectively.

Pump and signal propagation

Now, we write the equation governing the optical power evolution along the axis z of the fiber. The intensity change over a slice of thickness dz of the gain medium is given by [8]

$$\frac{dI_{s,p}}{dz} = \sigma_{s,p} N_{3,1}(z) I_{s,p}(z). \tag{2.29}$$

According to Eqs. (2.14) and (2.29), the optical power signal evolves as

$$\frac{dP_s}{dz} = 2\frac{\sigma_s P_s}{\omega_s^2}\int_S N_3(r,z)\psi_s(r)rdr. \tag{2.30}$$

The total amplified spontaneous emission (ASE) generated along the fiber is assumed to be the amplification of one spontaneous photon decay per bandwidth $\delta\nu$. This randomly polarized photon is generally considered as an equivalent input noise of power $P_0 = h\nu\delta\nu$. Including now the ASE for the two eigen-polarization modes in (2.30), we obtain

$$\frac{dP_s}{dz} = 2\pi\sigma_s\left[P_s + 2P_0\right]\int_S N_3(r,z)\overline{\psi}_s(r)rdr. \tag{2.31}$$

We introduce a similar equation for the evolution of the pump power coupled into the guided mode LP_{01}, along the z-axis of the fiber. We get

$$\frac{dP_p}{dz} = 2\pi\sigma_p P_p \int_S N_1(r,z)\overline{\psi}_p(r)rdr. \tag{2.32}$$

After substituting the population density $N_{1,3}$ from Eqs. (2.27) and (2.28) in Eqs. (2.31) and (2.32), and introducing the normalized input noise $s_o = P_0 / P_s^{sat}$, the dopant density profile $\rho(r)$, and the peak dopant density ρ_0 (ions/cm^3, see definitions in [8] pp. 242 - 243), we obtain finally

$$\frac{ds^{\pm}}{dz} = \pm 2\pi\rho_0\sigma_s\left[s(z)+2s_0\right]p(z)\int_S\left\{\frac{\rho(r)}{\rho_0}\overline{\psi}_s(r)\frac{\psi_p(r)}{1+p(z)\psi_p(r)+s(z)\psi_s(r)}\right\}rdr, \tag{2.33}$$

$$\frac{dp^{\pm}}{dz} = \mp 2\pi\rho_0\sigma_p p(z)\int_S\left\{\frac{\rho(r)}{\rho_0}\overline{\psi}_p(r)\frac{1+s(z)\psi_s(r)}{1+p(z)\psi_p(r)+s(z)\psi_s(r)}\right\}rdr. \tag{2.34}$$

In the above, the set of two equations describes the signal and the pump evolution along the z-axis for both directions (±). The first equation describes the amplification of the signal and the ASE. The second equation shows the pump absorption, the right-hand side is always negative. In this set of equations, we have assumed for both absorption and emission cross-sections (σ_p and σ_s) constant values over the interval of wavelengths considered. This is equivalent to assume homogeneous broadening of the gain medium. The saturation effect is taken into account through the normalized signal, noise (ASE) and pump powers. The overlap between the dopant distribution, the signal and pump mode envelopes, appears in the integrals. Finally, these two differential equations are nonlinearly coupled and require numerical integration.

General equation

In the most general case, the input signal, including ASE, can be considered to be spread over a set of k optical channels, which can be interpreted as a continuous signal spectrum. We get now k non-linear coupled differential equations for the signal and pump evolution.

In order to model the quasi-continuous signal spectrum evolution along the fiber, we can approximate the stimulated rate by the sum of the independent channels ([8], pp. 24), characterized by independent signal power $P_{sj}(z)$, saturation power P_{sj}^{sat}, and mode envelop $\psi_{sj}(r)$. We obtain then, using Eq. (2.25),

$$W_{32}(r,z,\nu)\tau_{fluo} = \sum_{j}^{k} \frac{P_{sj}(z)}{P_{sj}^{sat}} \psi_{sj}(r) = \sum_{j}^{k} s_j(z)\psi_{sj}(r). \tag{2.35}$$

We assume, in a first approximation, that the pump is monochromatic with a central frequency of ν_p, and a mode envelope $\psi_p(r)$. The pump can be launched in either or both directions in the fiber. We consider here only the case where the pump propagates in the positive z-direction ($P^- = 0$), which will be referred to in the following as the *forward pump*.

Let $s_j^{\pm}(z)$ be the normalized signal power at ν_j and $p^+(z)$, the normalized pump power. For simplicity we write $s_j^{\pm}(z) = s_j^{\pm}$ and $p^+(z) = p^+$. We can now generalize Eqs. (2.33) and (2.34) for the four-level laser system to

$$\frac{ds_i^{\pm}}{dz} = \pm 2\pi\rho_0\sigma_s(\upsilon_i)\left[s_i + 2s_{0i}\right]p^+ \int_S \left\{ \frac{\rho(r)}{\rho_0} \overline{\psi}_{si} \frac{\psi_p(r)}{1 + p^+\psi_p(r) + \sum_{j}^{k}\left[\left(s_j^- + s_j^+\right)\psi_{sj}(r)\right]} \right\} rdr, \tag{2.36}$$

$$\frac{dp^+}{dz} = \pm 2\pi\rho_0\sigma_p(\upsilon_p)p^+\int_S\left\{\frac{\rho(r)}{\rho_0}\overline{\psi}_p\left[\frac{1+\sum_j^k\left[\left(s_j^- + s_j^+\right)\psi_{sj}(r)\right]}{1+p^+\psi_p(r)+\sum_j^k\left[\left(s_j^- + s_j^+\right)\psi_{sj}(r)\right]}\right]\right\}rdr. \qquad (2.37)$$

The theoretical model developed above is based on the main assumption of homogeneous gain broadening and does not take into account the imperfection of the gain medium.

2.1.3 Numerical solutions

Solving Eqs (2.36) and (2.37) requires obviously a numerical implementation. There are only some particular cases, when the ASE is ignored, for which analytical solutions can be found. These simplified solutions correspond to a noise-free amplifier analysis. In the most general case, there are mainly two ways to solve this complex set of coupled differential equations: the shooting method and the relaxation method. The descriptions of theses two methods are developed in [22].

The relaxation method consists of an iterative approach to the solution. In a first time, the backward ASE is set to zero and only the forward integration from z = 0 to z = L is performed. The forward ASE obtained in this manner is used as starting condition for the backward integration. After a second integration, one has obtained a set of quasi-solutions for the forward and backward ASE. After some additional iteration, the quasi-solutions are progressively refined. After every two trials, the successive solutions are compared and the computation is stopped at a pre-set minimal error. The relaxation method is generally considered to be faster and less complex than the shooting method. Therefore, only the relaxation method has been implemented and tested.

The accuracy of the results depends strongly upon the experimental characterization of the physical and chemical parameters of the fiber, such as the mode envelopes, the dopant profiles, the dopant concentrations and the cross-sections. A brief review of the experimental techniques to characterize doped-fibers will be given in the next section.

Example

We compare in this example the theoretical and the experimental ASE spectra obtained from a Nd^{3+}-doped fiber for different pump values. In the first place, the program will include and acquire all the parameters of the fiber needed for the computation. These fiber parameters will be detailed in Tab. 2.2 (next section) and correspond to those of the Nd-doped fiber labeled Nd-060592.

The estimated cross-section for the laser transmission at 1.06 μm shown in Fig. 2.3 has been deduced from the measured fluorescence emission, using the *Fuchtbauer-Ladenburg* relation (Eq. (2.16)). For computation purpose, it is convenient to use an analytical expression for this estimated cross-section, so that the wavelength steps for the calculation can be chosen independently of the acquisition steps used for the measurements. We have chosen to fit the emission cross section to a linear superposition of Lorentzian functions given by

$$\sigma(\lambda) = \sum_i \left(\sigma_i Lor(\lambda_{0i}, \Delta\lambda_i)\right), \tag{2.38}$$

Where σ_i is the peak cross-section and

$$Lor(\lambda_{oi}, \Delta\lambda_i) = \left\{1 + \left[2(\lambda - \lambda_i)/\Delta\lambda\right]^2\right\}^{-1} \tag{2.39}$$

with λ_{0i} and $\Delta\lambda_i$ the central wavelength and the full width at half maximum (FWHM), respectively.

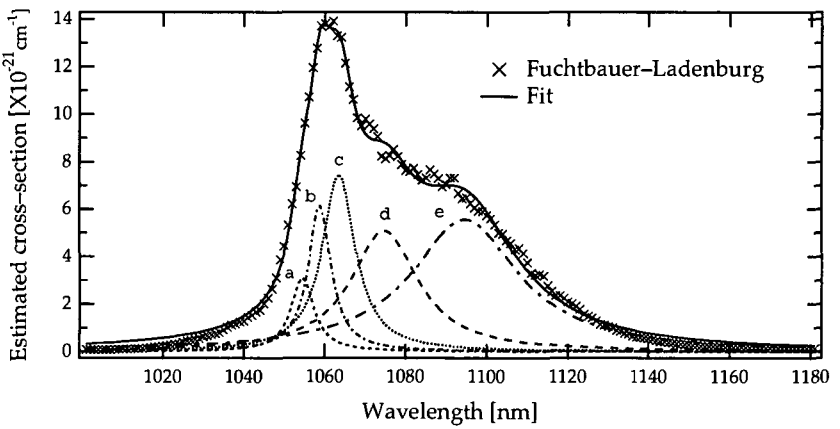

Fig. 2.3 Estimated cross-section from the experimental fluorescence lineshape at 1.06 μm of a Nd^{3+}-doped fiber (crosses) and the best fit (solid line) using five Lorentzian functions (a to e).

We have to point out, that the decomposition is arbitrary and not unique, and that the Lorentzian lines have no physical meaning and do not represent partial cross-sections of Stark levels of the transition. A sum of Gaussian functions could also be used for the fit. However, fewer Lorentzian functions are required for the fit and they are more suitable for the wings of the spectrum. In our example, five Lorentzian lines give a

quite good result. The measured and the fitted lineshapes, as well as the composing Lorentzian lines are shown in Fig. 2.3.

The program includes also input statements such as boundary conditions, number of iterations and the resolution steps, and also some output statements essential for monitoring the convergence of the computation, the ASE spectra and the pump evolution along the fiber. We use the 4^{th}-order Runge-Kutta algorithm to integrate the set of Eqs. (2.36) and (2.37). The main integration parameters used in this simulation are summarized in Tab. 2.1.

Fiber type	Axial range	Axial steps	Spectral range	Spectral steps	iterations
Nd-060592	0 - 600 mm	1 mm	1020 - 1180 nm	2 nm	30

Tab. 2.1 Range and integration step parameters used for the simulation

Computing the ASE represents actually the most difficult case. When the saturation is essentially caused by the amplification of a strong input signal, only few iterations are required for the convergence. However, a lot of iterations are required, when the ASE is dominant.

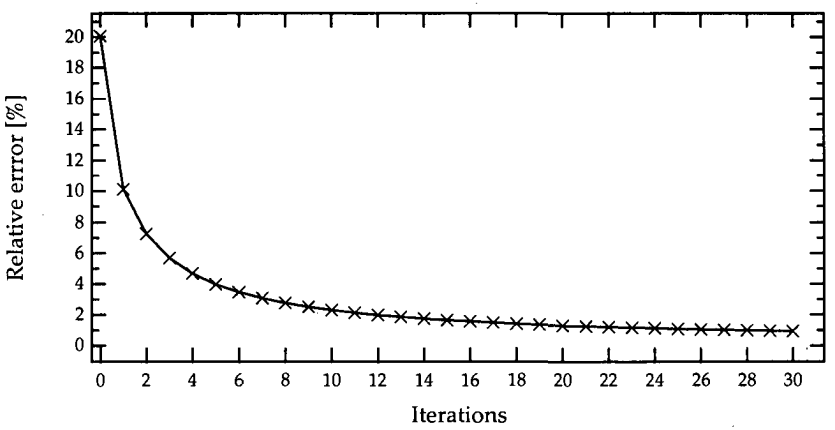

Fig. 2.4 Convergence versus number of iterations for the integration process. The convergence is expressed as the relative error of the forward ASE between two successive iterations.

The convergence depends strongly on the boundary conditions, on the pump value and on the resolution steps used for the integration over the fiber length and the emission spectrum. In the first integration, the backward ASE is neglected leading to an over estimation of the forward ASE. In the next iteration however, the saturation by the

backward ASE is taken into account and the cumulated saturation leads to accurate values for both forward and backward ASE.

The Fig. 2.4 shows the convergence of the forward ASE versus the number of iterations. The convergence is expressed as the maximum relative error between the successive ASE spectra of two successive iterations. The criterion upon which one decides to stop the iteration of the integration process is arbitrary. The convergence should tend asymptotically to zero and therefore, the amplitude of the forward ASE spectrum after 30 iterations remains still slightly over estimated.

We report in Fig. 2.5 a) and b), the normalized experimental and theoretical forward ASE spectra for different values of launched pump power. For best matching the measured ASE, the values of the pump powers used in the simulation have been slightly reduced. The differences between the theory and the experiment are about 20 % and 15% for the lowest and the highest value of pump, respectively.

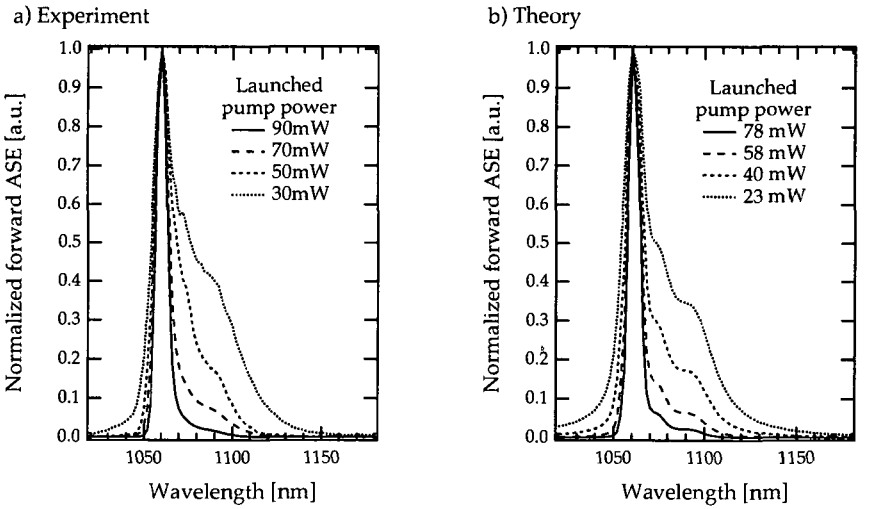

Fig. 2.5. Normalized forward ASE spectra obtained theoretically and experimentally in a Nd-doped fiber of 0.6 m length for different pump powers.

We found also a difference of the ASE output power between theory and experiment. The theoretical values are greater than the measured ones by about 20% and 25% for the highest and the lowest value of pump, respectively. After adjusting the theoretical pump power, as described above, we have reduced this gap to 5% and 12%, respectively.

The difference between the theory and the experiment can be attributed first to the fact, that we have considered a homogeneously broadened system for the simulation, which tends to emphasize the narrowing of the spectrum around the strongest emission. Also, the transitions at 930 and 1320 nm, with the excited state absorption (ESA) transition, have not been considered. In the second place, the calculated values of the cross-section, using the Fuchtbauer-Ladenburg relation are in general over estimated. Less important, the error of 3 to 5% in the estimation of the launched pump power and the homogeneity of the dopant distribution along the fiber length can also be considered for the interpretation of the results. Nevertheless, the theoretical ASE spectra are in very good qualitative agreement with the experimental results.

We observe a narrowing of the bandwidth as the pump power increases. When the system is homogeneously broadened, the ions characterized by the strongest probability of decay can interact with all the ions in the upper level and can extract all the energy stored in the population inversion. This effect tends to be amplified as the pump power increases, leading to a spectral narrowing around the strongest stark level transition.

2.1.4 Unsaturated gain regime

We define the unsaturated gain regime by the fact that the normalized signal power $s(z) = P_s(z)/P_s^{sat} < 1$. In this regime, Eq, (2.33) for the normalized signal power reduces to

$$\frac{ds^{\pm}}{dz} = \pm 2\pi\rho_0\sigma_s s(z)p(z)\frac{1}{A_s}\int_r \frac{\rho(r)}{\rho_0}\psi_s(r)\frac{\psi_p(r)}{1+p(z)\psi_p(r)}rdr \tag{2.40}$$

and Eq. (2.34) for the normalized pump power becomes

$$\frac{dp^{+}}{dz} = \pm 2\pi\rho_0\sigma_p p(z)\frac{1}{A_p}\int_r \frac{\rho(r)}{\rho_0}\psi_s(r)\frac{\psi_p(r)}{1+p(z)\psi_p(r)}rdr \tag{2.41}$$

In both cases the relation $\psi(r) = \psi(r)/A$ has been used, where A is the corresponding integrated area for the field distribution. The equation for the normalized pump power is independent of the signal s(z), and therefore Eq. (2.41) can be integrated independently of Eq. (2.40), at least numerically. The result $p(p_0,z)$ will depend on the initial pump power $p_0 = p(0)$ and can be used to calculate (numerically) the amplified signal s(z) with Eq. (2.40).

An analytical solution for the coupled Eqs. (2.40) and (2.41) can be found, if we assume that the field distribution $\psi_s(r)$ of the signal power is nearly constant ($\psi_s(r) \cong 1$) over the doped zone $\rho(r)$, which is in general limited to the core of the fiber. Under this

assumption, the integrals in Eqs. (2.40) and (2.41) are identical, and Eq. (2.40) can be expressed as

$$\frac{ds^{\pm}}{dz} = \mp \frac{\sigma_s}{\sigma_p}\frac{A_p}{A_s}\frac{dp^{+}}{dz}s(z) = \pm\gamma_0(z)s(z), \tag{2.42}$$

which means that the small signal gain coefficient $\gamma_0(z)$ is proportional to the locally absorbed pump power dp/dz. Equation (2.42) can now be integrated as

$$\int_{s(0)}^{s(L)} \frac{ds}{s} = \pm\frac{\sigma_s}{\sigma_p}\frac{A_p}{A_s}\int_{p(0)}^{p(L)} dp, \tag{2.43}$$

which yields

$$\ln\left(\frac{s(L)}{s(0)}\right) = \frac{\sigma_s}{\sigma_p}\frac{A_p}{A_s}\left[p(0) \pm p(L)\right] = \frac{\sigma_s}{\sigma_p}\frac{A_p}{A_s}\frac{P_{abs}}{P_p^{sat}} = \Gamma_0(L) \tag{2.44}$$

The integrated small signal gain $\Gamma_0(L)$ is therefore proportional to the total absorbed pump power $P_{abs} = P_p^{sat}(p(0) - p(L)$. From Eq. (2.44) we see that the gain factor

$$G_0(L) = \frac{s(L)}{s(0)} = \exp(\Gamma_o L) \tag{2.45}$$

expressed in dB becomes

$$G_0\big|_{dB} = 10\log(G_0) = 10\log(e)\Gamma_0 L = 10\log(e)\frac{P_{abs}}{P_p^{sat}}. \tag{2.46}$$

Doped fiber amplifiers are therefore often specified by the small signal gain factor G_0 (in dB) per total absorbed pump power P_{abs}.

2.2 Laser transitions in rare-earth doped glass fibers

In contrast to glass hosts, in rare-earth doped crystals sharp and individual line transitions, even at room temperature, are usually observed. The broader emission and absorption spectra provided by rare-earth doped glass led to use optical fibers for many applications involving broadband interaction.

This section glances through the transition diagrams of the rare-earth elements used in doped fibers, which will be considered and employed in this thesis. The description is therefore limited to diagrams of neodymium (Nd^{3+}), erbium (Er^{3+}), ytterbium (Yb^{3+}) and thulium (Tm^{3+}). These cases represent four, three and two level laser systems.

2.2.1 Neodymium

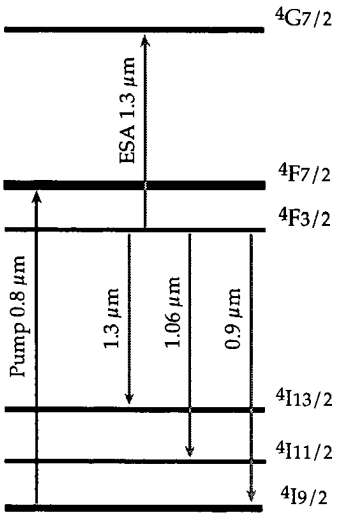

Fig. 2.6: Energy levels in Nd^{3+}-doped silica glass

The Nd^{3+} exhibit three bands where radiative emissions can take place. The $^4F_{3/2}$ -> $^4I_{11/2}$ transition at 1.06 μm, illustrated in Fig. 2.6, is probably the most studied transition for both glass and crystalline hosts. This four-level operation band provides very efficient and powerful laser emissions, with a possible up-conversion operation towards the green region. Because of the importance of 1.3 μm region for fiber communication, the $^4F_{3/2}$ -> $^4I_{13/2}$ transition became potentially attractive. However this transition suffers from large losses, attributed to the exited state absorption (ESA) which occurs on the same levels [23] [24].

The last transition at 0.9 μm, which operates in a three level regime, is not of great interest and has not been profoundly investigated. Finally, the Nd^{3+} can be optically pumped at 0.51 μm and 0.8 μm with Ar^{3+} laser and laser diodes, respectively

2.2.2 Erbium

Erbium (Er^{3+}) is the most extensively studied rare-earth laser ion after neodymium. Most of the discussions concern the $^4I_{13/2}$ -> $^4I_{15/2}$ transition at 1.55 μm, since this

wavelength corresponds to the commercially important third optical communication window. More recently, the advent of fluoride glass host has led to demonstrate several laser transitions that do not originate from the $^4I_{13/2}$ level (see Fig. 2.7).

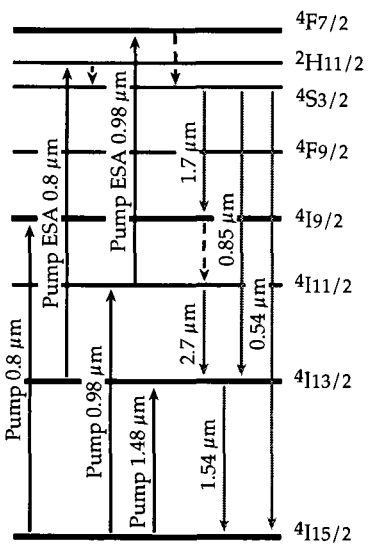

Fig. 2.7: Energy level of Er^{3+} in glass hosts

Excited state absorption (ESA) at the pump wavelengths 800 and 980 nm allows emission at 1.7 μm and 2.7 μm [25], and up-conversion operations at 540 nm. The $^4I_{11/2}$ -> $^4I_{13/2}$ transition at 2.7 μm presents actually more interest, since it corresponds to the peak absorption of the hydroxyl OH and thus finds application in surgery. There are six absorption bands between 480 nm and 1500 nm, but bands which match the emission of laser diodes are preferred nowadays. In general, 980 and 1480 nm bands are the best for pumping 1.55 μm devices, while the strong pump ESA at 800 nm is exploited for up-conversion operations.

2.2.3 Ytterbium

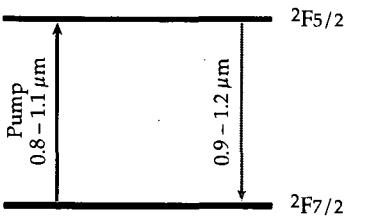

Fig. 2.8: Energy levels of Yb^{3+} in glass hosts

The ytterbium (Yb^{3+}) energy level structure is very simple and consists of two manifolds of overlapping sublevels; the ground state manifold $^2F_{7/2}$ and the excited state manifold $^2F_{5/2}$. The large energy gap between the two manifolds prevents non-radiative decay via multiphonon emission from $^2F_{5/2}$, even in silica glass.

The spectroscopy reveals broad absorption and emission bands, which allow pumping from 800 nm to 1064 nm and exploiting a wide emission range between 970 nm and 1200 nm.

Although the Yb^{3+} has been for a long time neglected for the benefit of the efficient Nd^{3+}, very efficient laser action, with slop efficiencies of up to 90%, have been

demonstrated more recently between 1020 nm and 1140 nm [26]. The particular laser actions at 1020 nm and 1140 nm allow up-conversion laser action in Pr^{3+}-doped ZBLAN fibers and Tm^{3+}-doped fluoride fibers, respectively. Lasers emission at 1020 nm is also useful for pumping the 1300 nm Pr^{3+}-doped fluoride fiber amplifiers.

Finally, Yb^{3+} ions are used as sensitizer ions, absorbing pump photon and then transferring the energy, via cross- relaxation, to acceptor ions, such as Er^{3+}. This process improves pumping absorption in Er^{3+}-doped fibers and helps short cavity design with efficient laser operation [27], [28].

2.2.4 Thulium

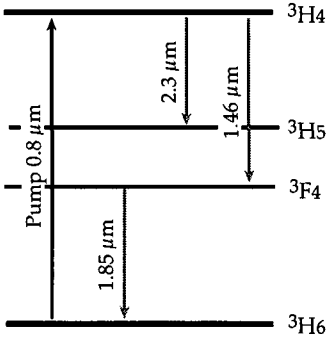

Fig. 2.9: Energy levels of Tm^{3+} in glass hosts

Figure 2.3 shows the partial diagram of Tm^{3+}-doped glass fibers. We report the useful emissions observed in Tm^{3+}-doped glass fiber, which can operate at wavelengths ranging from 1700 to 2056 nm [29] [30]. Although silica fibers perform quite well on the $^3H_4$ -> $^3F_4$ and the $^3F_4$ -> $^3H_6$ transitions, at 1.46 μm and 1.85 μm respectively, the relaxation form $^3H_4$ and $^3F_4$ levels are predominantly nonradiative.

The small energy gap of the $^3H_5$ level causes multi-phonon emission with an extremely short lifetime. Tm^{3+} has two other important states, $^1G_4$ and $^1D_4$, which are metastable in most glasses. In silica glass, the radiative decay rate for the $^1G_4$ is larger than for the $^3F_4$ and has an efficiency close to 50%. Direct pumping to the $^1G_4$ and $^1D_4$ levels requires 460 nm and 350 nm, respectively. These short wavelengths are not available from laser diodes, but up-conversion pumping via inter-mediate states can overcome this impediment. Finally, the $^3H_4$ level can be efficiently pumped at 800 nm, even though this level is dominated by nonradiative relaxation.

2.3 Fiber parameters summary

The values of the physical parameters for the different doped silica fibers used in the work of this thesis, are given in Tab. 2.2.

Fiber Type	Dopant: co-dopant	Concentration (ppm-wt)	Transition	Lifetime (μs)	Attenuation (dB/m)
Nd-160491	Nd^{3+}: Al^{3+}	Nd^{3+}: 10700	$^4F_{3/2}$ -> $^4I_{11/2}$	336	470 @ 800 nm
Nd-100192B	Nd^{3+}: Cs^{1+}	Nd^{3+}: 10000	$^4F_{3/2}$ -> $^4I_{11/2}$	330	440 @ 800 nm
Nd-060592	Nd^{3+}: Cs^{1+}	Nd^{3+}: 930	$^4F_{3/2}$ -> $^4I_{11/2}$	507	41 @ 800 nm
Nd-95020E*	Nd^{3+}: Ge^{4+}	Nd^{3+}: 295	$^4F_{3/2}$ -> $^4I_{11/2}$	472	13 @ 800 nm
Yb133**	Yb^{3+}:Al^{3+} / Ge^{3+}	Yb^{3+}: 1800 Al^{3+}: 2100	$^2F_{5/2}$->$^2F_{7/2}$	–	177 @ 980 nm
EY304**	Er^{3+}: Yb^{3+}/Ge^{4+} /P^{5+}	Er^{3+}: 2200 (Yb^{3+}: 2.4%)	$^4I_{13/2}$-> $^4I_{15/2}$	9800	540 @ 978 nm 9.7 @ 1538 nm
EY105**	Er^{3+}: Yb^{3+}/Ge^{4+} /Al^{3+}/P^{5+}	Er^{3+}: 4100 (Yb^{3+}: 3.2%)	$^4I_{13/2}$-> $^4I_{15/2}$	9600	900 @ 978 nm 30 @ 1538 nm
Er123**	$Er^{3+}Ge^{4+}$/ Al^{3+}/P^{5+}	Er^{3+}: 4100	$^4I_{13/2}$-> $^4I_{15/2}$	9700	27 @ 978 nm
Er-300393	Er^{3+}: –	Er^{3+}: 500	$^4I_{13/2}$-> $^4I_{15/2}$	10200	4.3 @ 794 nm
Tm-050493	Tm^{3+}: –	Tm^{3+}: 500	$^3H_4$ -> $^3F_4$ $^3F_4$ -> $^3H_6$	~455 ~870	97.5 @ 786 nm

The fibers have been manufactured by the Swiss Center for Electronics and Microtechnology (CSEM), by (*)York®, and by (**) the National Institute of Optics (INO), Québec.

Tab. 2.2 Physical parameters for samples of Nd^{3+}, Er^{3+}, Yb^{3+}, and Tm^{3+}-doped silica fibers

3 Broadband light sources

Rare earth-doped fibers still receive a large attention for their applications as superfluorescent fiber laser (SFL) sources and amplifiers in a manifold of optical systems. Many of these devices are efficient enough to be pumped with diode lasers and thus they are potentially compact, and low cost. Applications are currently concentrated on the telecommunication and networks, where Er^{3+}-doped fiber amplifiers (EDFA) have stimulated the largest interest because of their near-term commercial returns. In second order, broadband ASE operations found also applications in sensing and metrology.

Low temporal coherence or broadband light sources are useful sources for white light interferometry and for addressing distributed sensor systems. Lot of work has been devoted to the fiber-optic gyroscope (FOG), for which 10 nm spectral bandwidth are broad enough to reduce noise factors from Rayleigh back-scattering and optical Kerr effect [31] [32].

Broadband sources are available from light emitting diodes (LED's), superluminescent diodes (SLD's), and superfluorescent doped fiber. Compared to LED's and SLD's, rare earth monomode doped-fibers exhibit higher brightness and greater spectral stability with temperature [33]. For applications requiring coupling into single-mode fibers, only high radiant pigtailed SLD's provide equivalent characteristics of those obtained with doped fibers.

As we have seen in 2.1.3, the required broad spectrum is difficult to obtain from a single doped fiber because of the narrowing introduced by the amplification of the spontaneous emission at increasing pump power levels. This narrowing is obviously more important, if we use a configuration, with one end-mirror called double-pass configuration. This current chapter proposes interesting approaches, which can overcome partially the unwanted effect of narrowing. The use of different types of doped fiber [34], besides spectral filtering, in double pass or a dual-stage configuration, will be illustrated in the following by some examples.

3.1 Broadband fiber source design

We outline in this section the important issues necessary for efficient broadband SFL source elaboration. We first discuss laser and pumping characteristics of widely used Erbium and Neodymium-doped fibers. Next, we briefly expose the commonly used SFL configurations.

3.1.1 Nature of the transition

Rare-earth doped fiber source design will depend on the nature of the transition under consideration. In two and three-level systems, the lower state manifold of laser transitions are the ground state manifold. Therefore, the inversion is more easily accomplished for longer wavelength transitions, and in the same way shorter wavelengths are preferentially absorbed. Consequently, the emission spectrum from both fiber-ends is a complex function of the fiber length, the pump power and the pump wavelength. In general, from three-level systems, backward ASE (traveling toward the pump), and forward ASE spectrum shapes are different.

In four-level systems instead, excepting ESA re-absorption, the lower laser manifolds is continuously depopulated, exhibiting net gain even at low pump intensities, and there is no signal re-absorption. Therefore, designing ASE sources with such transitions becomes less complex. In single-pass configurations, the output power and the ASE spectra are almost identical at both fiber-ends.

3.1.2 Pumping

In order to show the emission spectrum evolution with the pump power in three-level systems, 2.5 m of 500-ppm Er^{3+}-doped fiber (Er-300393) has been pumped at 980 nm in a single-pass configuration. The attenuation at this pump wavelength is 10 dB/m. Thus, we assume that the totality of launched pump power is absorbed. Forward emission spectra as a function of absorbed pump power are shown in Fig. 3.1.

For high pump power values (> 50 mW), almost all dopant ions are excited (100% inversion) and forward and backward ASEs have their maximum gain at 1530 nm. At low population inversion (pump power < 30 mW), ground level absorption in the unpumped fiber length still dominates from 1520 to 1540 nm, leading to the suppression of the peak at 1530 nm of the forward emission as it propagates. On the other hand, backward ASE is amplified as it propagates toward the pump, since the ground state absorption is bleached in the pumped fiber region. Thus, the peak at 1530 nm is always present in the backward emission spectra. In the low inversion

regime, the differences between backward and forward ASE spectra are more important in the case of long fiber length.

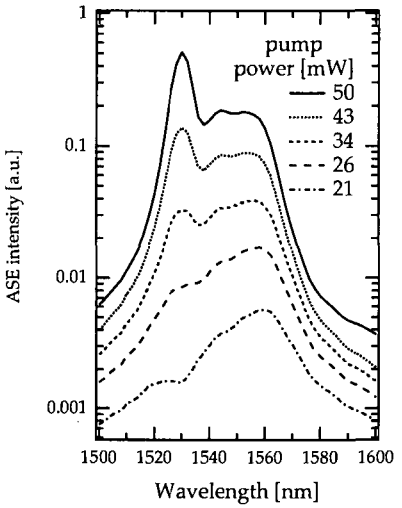

Fig. 3.1 Er^{3+}-doped fiber forward ASE for different absorbed pump powers.

Pumping doped fibers outside of the peak absorption add a degree of freedom to ASE output power and spectrum shaping. Tuning the pump wavelength, by several nanometers toward shorter wavelengths, is readily accomplished by cooling the pump laser diodes. Spectral shaping in four level systems with pump wavelength shifts is useless, since only the absorbed pump power is modified. On the other hand, pump power redistribution along the fiber, which arise from this shift, could be an advantage for avoiding quenching effects due to ion clustering, particularly when high pump power is launched in highly doped fiber.

In three and two laser systems, pump distribution, modulated by the pump wavelength, has a great influence on the ASE emission shape. Figure 3.2 shows simulated pump power distribution in a 5 m-long Er^{3+}-doped fiber and the corresponding ASE output for different pump wavelengths.

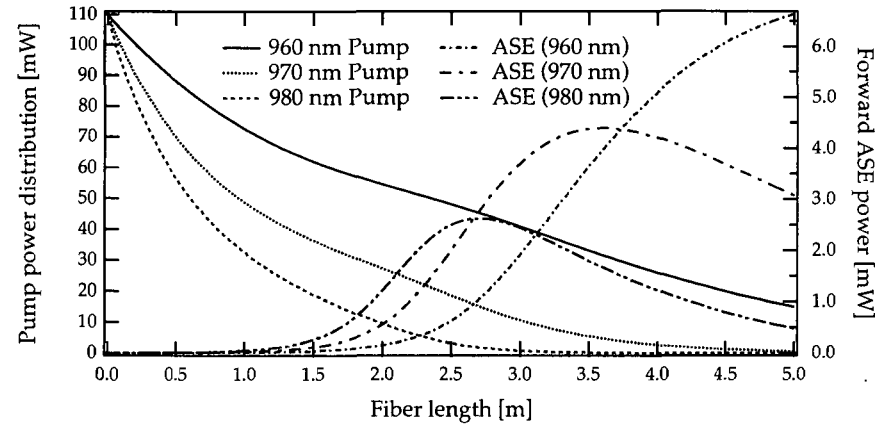

Fig. 3.2 Simulated forward ASE output power and pump power distribution as a function of fiber length for different pump wavelengths.

The fiber, which absorbs 8 dB/m at 980 nm, was pumped at 960, 970, and 980 nm, with a fixed input pump power of 110 mW. The optimal output power versus fiber length, when pumping at 980 and 970 nm, are 2.5 mW at 2.7 m, and 4.4 mW at 3.6 m, respectively. The optimal pump wavelength, for the total length, should be located between 960 and 970 nm. Although the pump power was not totally absorbed, when pumping at 960 nm, the signal has the largest output power with a value of 7 mW.

At 980 nm, nearly all the pump is absorbed in the first 3 m, and the last 2 meter unpumped fiber reabsorbs the forward ASE signal around 1530 nm. Shifting the pump wavelength outside the peak absorption distributes the pump power over a longer fiber length. Therefore, background absorption at 1530 nm is partially bleached. Figures 3.3a, shows that backward ASE spectra are nearly equal, while forward ASE spectra, in Fig. 3.3b, are pump wavelength dependent. Ground state absorption, together with pump wavelength tuning, will be exploited later in § 3.3.1 for ASE spectral shaping.

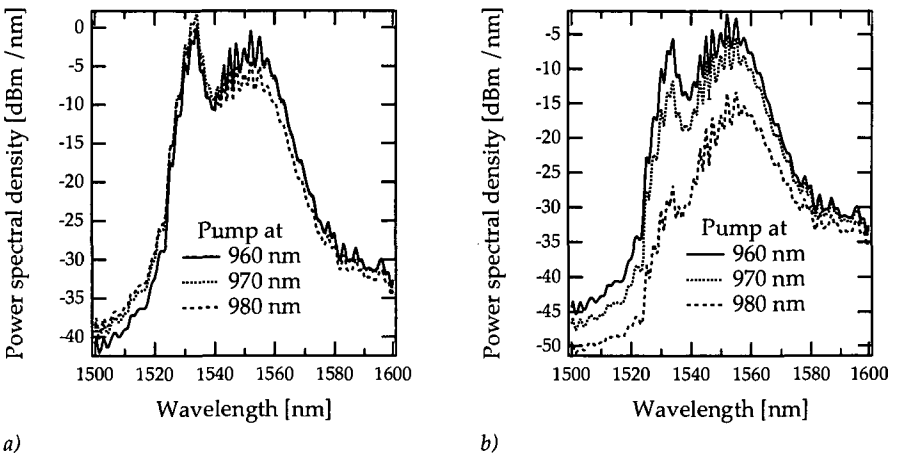

Fig. 3.3 Simulated backward a) and forward b) ASE spectra from a 5-m Er^{3+}-doped fiber (500 ppm), for different pump wavelengths.

3.1.3 Pump sources

In general, most absorption bands of rare earth doped fibers are covered by the large variety of pump sources. Ti:saphir lasers and dye lasers are useful tunable and powerful pump sources for laboratory investigations and prototyping. However, their use outside the laboratory is not conceivable, since they are large and require themselves optical pumping. Semiconductor laser diodes are preferred when compact and low cost solutions are needed. Powerful GaAlAs pump diodes, with several W of power, are available at 800 nm for pumping Nd^{3+}-doped fibers. More recently, GaAlAs

diodes at 980 nm, and InGaAsP diodes at 1480 nm, became commercially available for pumping Er^{3+} and Yb^{3+}-doped fibers. They provide up to 100 mW output power, as free space or pigtailed sources. Pigtailed laser diodes with coupling efficiencies, close to 70%, avoid bulk five-axis bench-alignment, reducing thus the cost of the fiber source devices.

3.1.4 Spectrum and band-pass limitation

For a given fiber source, the detected emission spectrum depends on the spectral sensitivity of the photodiode used for the detection. Indium–Gallium-Arsenide (InGaAs) and Germanium (Ge) photodiodes cover the detection of the near-infrared region from 0.8 μm to almost 2 μm. We have used these photodiodes, since their detection bands match quite well with Nd^{3+}, Yb^{3+}, and Er^{3+}-doped fibers radiative transitions. For Tm^{3+}-doped fibers, the fluorescence at 1.8 μm is truncated by the sharp decrease of the spectral sensitivity of InGaAs photodiodes at this wavelength. Ge photodiode with a cooling element are preferred, since the smooth decrease of its sensitivity extends beyond 1.8 μm. The typical spectral sensitivities of these common photodiodes can be found in the corresponding datasheets. For absolute measurements, the emission spectrum can be normalized by the spectral response of the detector, removing all ambiguities concerning the detection. Nevertheless, we have preferred to keep the detected emission spectra unchanged and to indicate the type of photodiode used for the detection.

Recently developed fiber couplers and Bragg gratings have replaced bulk dichroic and dielectric out-coupler and reflectors, enabling all-fiber designs. Nevertheless, compared to dichroic reflectors, the commercially available signal band-passes of fiber output-couplers are generally limited, exceeding rarely 60 nm. All-fiber designs, using fiber couplers, are not recommended when broadband emission (> 60 nm) is required.

3.1.5 Common practical configurations

We report in Fig. 3.4, the simplest SFL source structure. This configuration consists of non-reflecting angled fiber-ends. The fiber-end surfaces are generally cleaved or polished at 9°, reducing Fresnel reflections. Parasite reflections are responsible of modal structures and reduce the bandwidth of the emission. In this configuration, forward and backward ASE travels through the fiber in opposite directions in the so-called single-pass configuration. A dichroic mirror allows extraction of the backward emission. Single-pass configurations are the least efficient devices, but generate ASE with a quite large band emission. For neodymium doped fibers, we have typically 40 nm bandwidth (FWHM) and 50 μW output for 50 mW of absorbed pump power.

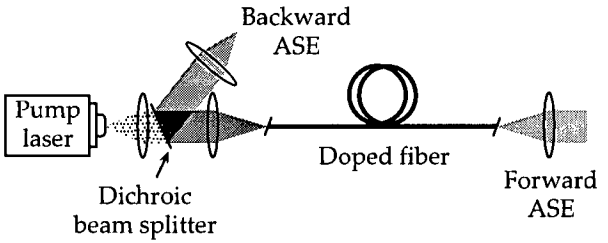

Fig. 3.4 Single-pass configuration of a superfluorescent doped fiber source.

Figures 3.5 a) and b) illustrate both double-pass configurations. In Fig. 3.5 a), the backward signal traveling toward the pump is totally reflected and re-amplified through a second pass along the fiber. The backward photon generated at the right fiber-end will be emitted in the forward direction, after two passes through the gain medium. In Fig. 3.5 b), the forward ASE is reflected toward the pump and the double-pass ASE is emitted in the backward direction.

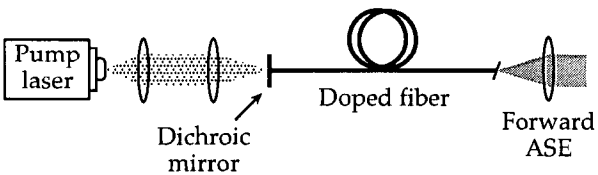

a)

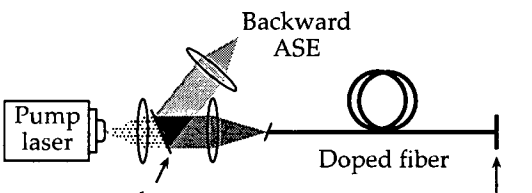

b)

Fig. 3.5 Configuration of superfluorescent fiber sources: a) double-pass with forward signal output, b) double-pass with backward signal output.

Both double-pass configurations are efficient enough to provide high power with pump conversion slope efficiencies of 10 to 15%. Since one of the fiber-ends is reflective, particular care must be taken to avoid optical resonance, especially at high pumping levels. Of course, scanning with a Fabry-Pérot analyzer enables to verify whether any modal resonances occur, but simple analysis of the output power evolution versus the pump power near the threshold is also revealing. Low and abrupt threshold transitions are the result of a resonant laser activity.

3.2 Broadband sources combining different types of fibers

The incorporation of additional chemical elements as co-dopant into doped fibers is now fully exploited. Co-dopants are mostly used as sensitizer or as quencher. Quencher help to depopulate the lower level of self-terminating laser transitions or other metastable levels from where unwanted excited-state absorption occurs. An important effect of glass host composition is the change in energy separation between stark levels. Such a change in energy separation causes a shift in the peak wavelength of the absorption and emission spectra. The combination of different fibers having their fluorescence spectrum displaced one with respect to the other by several nm allows to obtain a cumulative broad emission spectrum. The simplest way to realize such combinations consists of connecting different types of fibers together. However, this requires optimization of several parameters, such as the length of the fibers, the absorption rate, the gain of each fiber, the pump wavelength availability, and pump mixing if different. Monitoring the contributions of each fiber independently through individual pumps would be ideal. As it will be shown below, we used a dual-stage SFL and then an additional amplifier stage. These cascaded configuration profits of combined amplification effects, which could not be obtained with a mere superposition of independent contributions.

3.2.1 Single-pass in dual stage configuration

In a first experiment, we have combined two kinds of single mode Nd-doped silica fibers. The presence of germanium in the first fiber (Nd:Ge) shifts the emission peak to 1088 nm [23]. The second fiber, which is co-doped with cesium (Nd:Cs) has the maximum emission at 1064 nm. For the convenience of the experiment, we have fusion-spliced a wavelength division multiplexing coupler (WDM) between 1-meter long pieces of each fiber. It was therefore possible to monitor carefully the pump power launched into each fiber and to achieve the desired shape of the spectrum at the output.

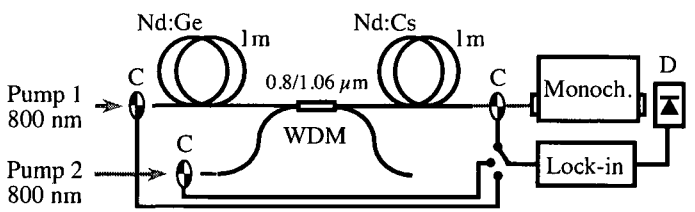

Fig. 3.6 Combined SFL using two types of Nd^{3+}-doped fibers. The fluorescence spectra are optically modulated with choppers (C) and measured through a grating monochromator using a single photo-diode (D) and synchronous detection (Lock-in).

Although the fibers have not the same host composition, the absorption wavelengths are approximately the same and centered around 805 nm. Thus, two identical pump sources have been used. The Fig. 3.6 shows the experimental setup for a forward single-pass configuration. The pump1 and the pump2, together with the wavelength division multiplexer coupler (WDM), allow to pump the Nd:Ge and the Nd:Cs fiber independently. The coupler has a flat transmission curve for wavelengths greater than 1 μm, therefore the Nd:Ge emission spectrum is not modified. We assume that the attenuation of the transmitted signal through the unpumped second fiber is negligible. By the amplification and the super-fluorescence emission of the Nd:Cs doped fiber we expect to get an enlarged spectral emission.

Synchronous detection between pump source modulation and output modulation, using optical choppers allows the extraction of different spectra. To measure the emission spectrum of the Nd:Ge, we have modulated pump1 while pump2 was switched off. Vice versa, modulation of pump2 and pump1 switched off gives the emission spectrum of the Nd:Cs fiber. These two spectra are shown as dashed and dashed-dotted lines in Fig. 3.7 respectively.

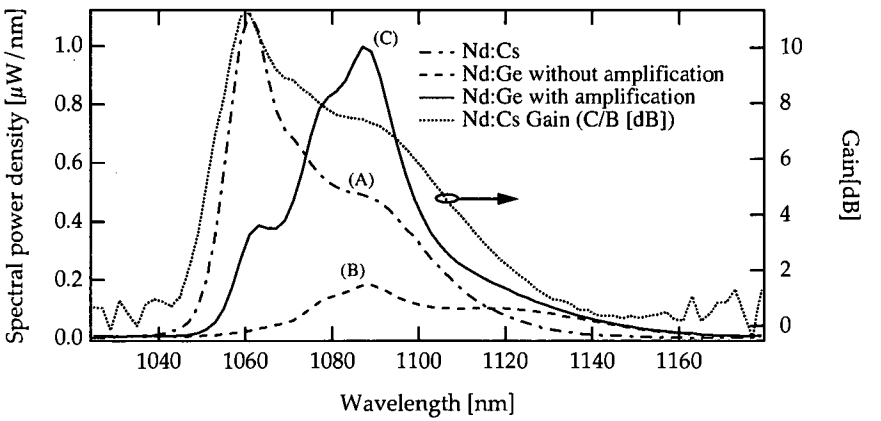

Fig.3.7 Nd:Cs and Nd:Ge doped fiber emission spectra (dashed curves). The solid curve represents the amplified Nd:Ge emission spectrum and the doted curve represents the Nd:Cs gain spectrum in dB.

In order to measure the amplification of the Nd:Ge emission through the pumped Nd:Cs fiber (solid curve in Fig. 3.7), both pump sources are switched on and the modulation is applied to pump1. The gain of the Nd:Cs fiber is therefore given by the ratio between the amplified and non-amplified Nd:Ge emission spectra. This gain, expressed in dB, is represented as doted curve in Fig. 3.7.

In the experiment (Fig. 3.6), the power of pump2 was 65 mW, the length of the Nd:Cs fiber was L = 1m and the attenuation of this fiber at the pump wavelength was 35 dB/m. With an estimated coupling efficiency of the pump source to the fiber of 45% and 2% losses in the coupler we get for the total absorbed pump power $P_{abs}(z=L) \approx 28.5$ mW. In a previous experiment [24], the small signal gain $g_L(\lambda)$ as a function of the wavelength has been measured for the same Nd:Cs fiber in dB/mW of absorbed pump power. According to the Eq. (2.43), the spectral gain G(L) of the Nd:Cs fiber (Fig. 3.7), which represents the ratio between the amplified and non-amplified Nd:Ge emission spectra, can be estimated using the small signal gain $g_L(\lambda)$ of [24] and the absorbed pump power P_{abs} (28.5 mW).

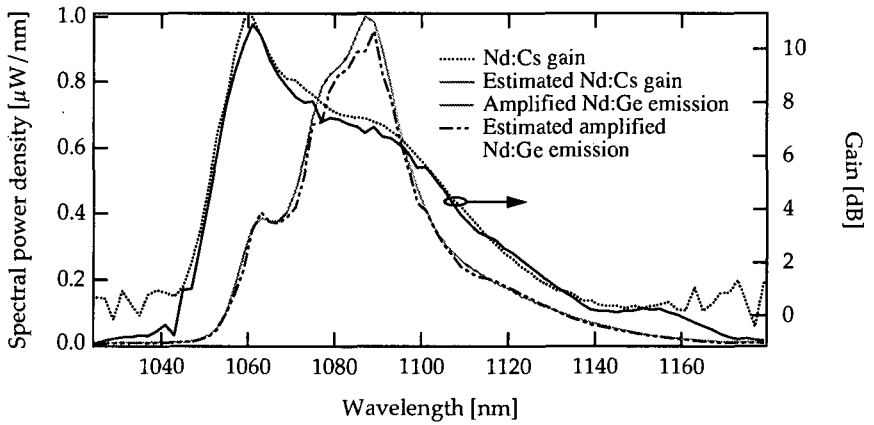

Fig. 3.8 Comparison between the measured and the estimated Nd:Cs and between the measured and the estimated spectrum of the amplified Nd:Ge emission

For comparison, the result is shown as solid line in Fig. 3.8, together with the measured spectral gain of Nd:Cs fiber from Fig. 3.7. The agreement between the two curves is very good over the whole range of the measurement.

Moreover, using the values for the spectral gain of the Nd:Cs fiber and the non-amplified Nd:Ge from Fig. 3.7, the amplified Nd:Ge emission can be calculated. For comparison, the result is shown as dashed-dotted line in Fig. 3.8, together with the measured curve (C) from Fig. 3.7. The small difference of about 4% is probably due to the underestimation of the absorbed pump power in the Nd:Cs fiber.

The measured SFL spectrum of the total contribution of the combination (Nd:Cs and Nd:Ge) is represented by the solid line in Fig. 3.9. The spectrum is centered at 1078 nm and it has a nearly flat top shape with 1.3 dB ripple peak to peak. The total output power was 75 μW and the full-width at half-maximum (FWHM) was greater than 45

nm. It is interesting to see that the sum of the independently measured Nd:Cs emission (A) and the amplified Nd:Ge emission (C), reported in dotted line in Fig. 3.9, gives the same shape as the measured SFL of the combined fiber output.

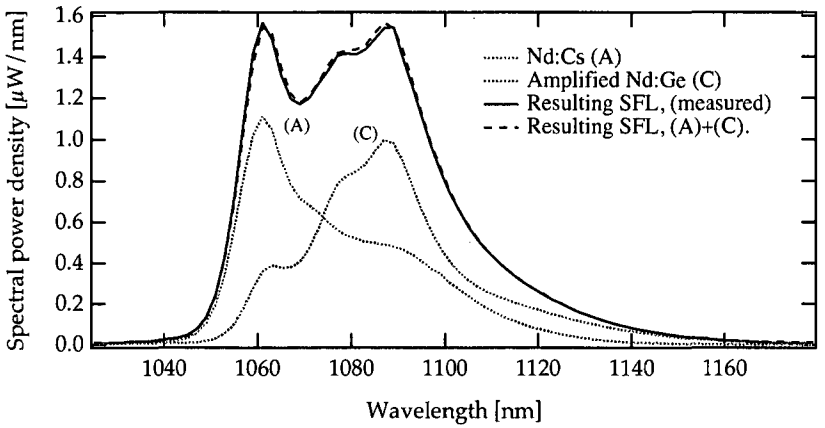

Fig. 3.9 SFL emission using Nd:Cs and Nd:Ge doped fibers as shown in Fig. 3.6.

We have shown that an appropriate combination of different kinds of doped fibers allows to achieve of super-fluorescent broadband emission. In the unsaturated gain regime, the total emission spectrum can be deduced from the known spectral distribution of low signal gain and the absorbed pump power for each fiber.

3.2.2 Single-pass in tripartite fiber configuration

In the second experiment, shown in Fig. 3.10, we tried to extend the emission bandwidth to shorter wavelengths by adding an Yb-doped fiber.

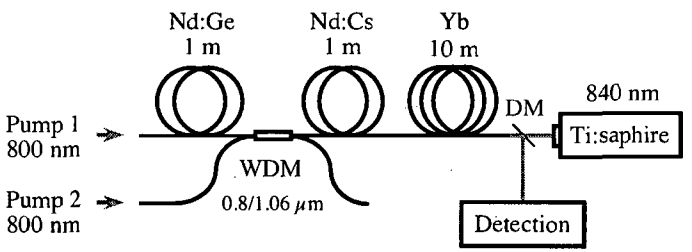

Fig. 3.10 Setup with three fibers. With respect to Fig.3.6, an Yb-doped fiber is added and pumped by a Ti:saphire laser through a dichroic beam-splitter (DM).

For this purpose, a 10-meter long single mode Yb-doped fiber was spliced at the end of the Nd:Cs fiber. The 840 nm pump beam from a Ti:saphire laser was launched through a dichroic mirror (DM) into the Yb-doped fiber.

Backward emission from a 10 m-long Yb-doped fiber provides an emission peak at 1040 nm, close to the Nd-emission spectra. Indeed, for a pump wavelength of 840 nm and for relatively low pump power (50 mW launched), the gain appears mainly at long wavelengths around 1050 nm. At higher pump power, the gain moves to shorter wavelengths around 976 nm [26].

As we have shown above, we can expect amplification of the combined Nd-spectra by the gain and the superfluorescence of the Yb-doped fiber. Figure 3.11 shows the final result of the configuration shown in Fig. 3.10. By adjusting the pump power from the Ti:saphire laser, it was possible to achieve a flat-top spectrum with ripples of less than 0.9 dB peak-to-peak (the vertical scale in Fig. 3.11 is linear). The total measured power exceeds 100 μWatt at the output of the single mode fiber. The full-width at half-maximum (FWHM) is larger than 70 nm.

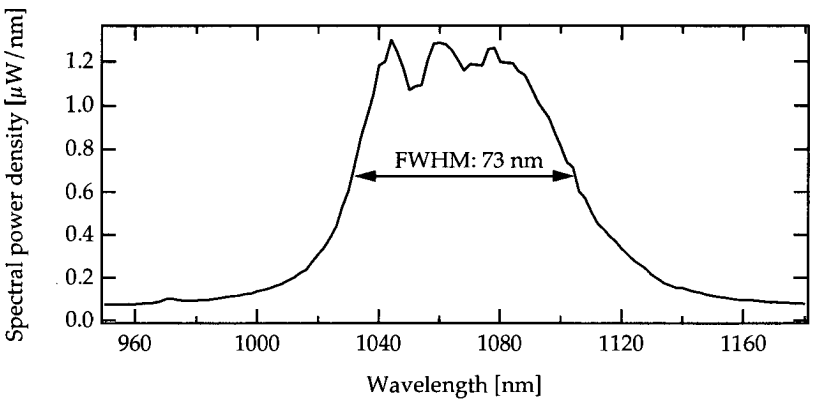

Fig. 3.11 SFL emission using Nd:Cs, Nd:Ge and Yb doped fibers as shown in Fig. 3.10. The emission peak of the Yb doped fiber is around 1042 nm.

At higher pump levels the emission of Yb becomes dominant, with a narrow peak at 1042 nm. A similar behavior occurred in the first experiment when the pump power was increased: a dominant peak from the Nd:Cs fiber appears around 1064 nm The narrow emissions of the dominant transitions generate therefore dips in the SFL spectrum. We propose to introduce passive loss-filters to reduce the influence of the dominant transitions in order to maintain a flat top emission spectrum even at increased pump power. This kind of passive optical band rejection filters is already

used in fiber amplifiers for telecommunication systems in order to achieve spectral gain equalization [35].

Such combination of differently doped-fiber could be applied as well to other dopands like a pair of Er^{3+} and Tu^{3+}-doped fiber. We have pumped simultaneously a pair of Tu^{3+}:Er^{3+}-doped fibers at 798 nm, using a Ti:saphir laser. At this wavelength both erbium and thulium are absorptive, we could therefore use the same pump source. Note that pumping thulium and erbium-doped fibers at 800 nm is not efficient because of the presence of pump ESA. For more efficiency, erbium could be pump at 980 nm using an adequate WDM coupler. The pump was launched through 6 cm-long Tu^{3+}-doped fiber, which is fusion spliced to a 20 cm-long Er^{3+}-doped fiber. The residual pump, which was not absorbed by Tu^{3+}-doped fiber, was used for pumping the second fiber. Thulium exhibits two lobes: one at 1450 nm, and the second at 1800 nm. Erbium is partially reabsorbed, exhibiting a peak at 1550 nm rather than at 1530 nm. This basic construction, which connects two complementary emissions, allows very broad emission spectrum as shown in Fig.3. The FWHM of the emission spectrum extends over 350 nm, from 1500 nm to almost 1850 nm. However, the interest of such sources, exceeding several hundreds of nano-meter, must be put in perspective.

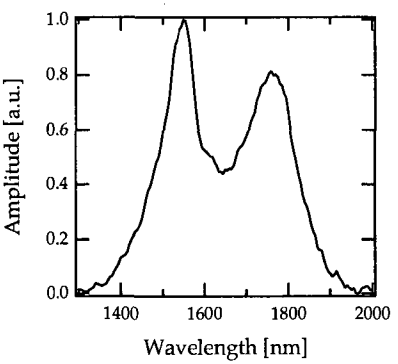

Fig. 3.12 Extended doped fiber source, using Er and Tu-doped fiber combination

The transparent window in silica glass is bounded by Rayleigh scattering on the short-wavelength side and by infrared absorption on the long-wavelength side. Sources emitting beyond 1.7 μm, are useless for application using long distance measurement and interrogation. In the other hand, for applications requiring low temporal coherence, sources at short wavelengths are preferable, since the coherence time is inversely related to the optical frequency bandwidth of the emission. We have shown that appropriate combinations of different fiber types allow the realization of SFL broadband emission. In the unsaturated regime, the total emission spectrum can be deduced from known spectral distribution of the low gain regime and the absorbed pump power for each fiber. Two kinds of Nd^{3+}-doped fibers and a Yb^{3+}-doped fiber have been tested in a single-pass configuration. A bandwidth as large as 70 nm with a single mode output power greater than 100 μW was achieved. The form of the source spectrum can be partially tailored by controlling the pump powers.

3.3 Broadband fiber sources using spectral filtering

ASE spectral filtering, before high power amplification rather than at the output, constitutes the unique approach to achieving broadband emission with high power. Passive long period gratings (LPG's) generate losses by coupling the propagating mode to unguided cladding modes [35]. However, ASE control with passive components limits the range of the use of the fiber source. The most convenient solution consists of the use of adjustable loss filters. All fiber acousto-optic tunable notch filter with electronical control of the spectral profile was proposed by Kim *et.al.* for WDM optical communication systems [36]. A very efficient fiber source was realized in an interesting approach consisting of spatial filtering in the spectrum of the ASE obtained by a diffraction grating [37]. In the following, we illustrate the effect of spectral filtering with two examples; the first one uses an unpumped Yb^{3+}-doped fiber as saturable absorber, the second one uses a metal-coated LPG tunable filter.

3.3.1 Ground state absorption as spectral filter

As described in section 3.1, three and two level laser systems reabsorb the emitted light in the part of medium without inversion, i. e. the unpumped part of the fiber. Since the re-absorption is wavelength dependent, we tried to use the unpumped fiber as spectral filter. The experimental setup is illustrated in Fig. 3.13. The 980 nm pump from two laser diodes was launched from both sides through a WDM coupler and a dichoic beam splitter, respectively, into 10 m-long ytterbium doped fiber (type Yb113).

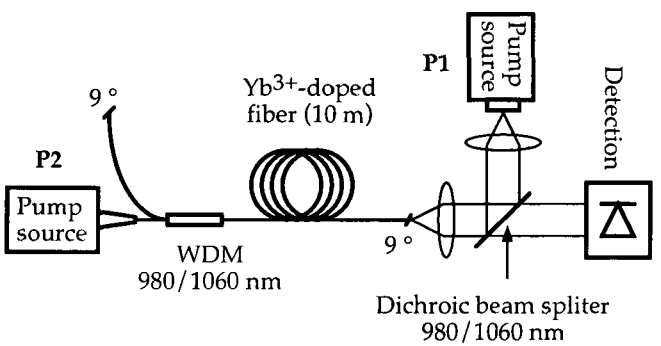

Fig. 3.13 Double side pumping configuration using 10-m ytterbium doped fiber

An ytterbium-doped fiber was chosen mainly because of its broad amplification bandwidth. This construction could be applied as well with other dopant, e.g. erbium. The fiber-ends were cleaved at 9° to avoid back reflections. The dicroic beam splitter has a high reflectivity at 980 nm (90%) and relatively broad and flat transmission (95%)

in the range of 1020 nm to 1200 nm. The output signal was detected after the dicroic mirror using synchronous detection through a grating monochromator.

With the help of Fig. 3.13, the principle of the experience can be summarized as follows. By setting pump 2 on and pump1 off, the forward ASE will undergo in the unpumped fiber region spectral filtering. This filtering occurs at the shorter wavelengths of the ASE emission, due to the two-level nature of the ytterbium laser transition. At the output end of the fiber, near the pump 1, the filtered ASE exhibits then maximum emission at longer wavelengths. This filtered ASE constitutes the input signal which feeds the last meter of the unpumped fiber, before the output end fiber near the pump1. Setting now pump1 and pump2 on, the filtered ASE will be amplified by the gain provided in the fiber by pump1 near the output end of the fiber. The amplification of the forward feed occurs obviously at the longer wavelengths of the spectrum, while shorter wavelengths of the backward ASE, resulting from pump1, saturate the gain at these wavelengths. The resulting spectrum with a FWHM of more than 90 nm is the solid line shown in Fig. 3.14. As explained in § 1.2.1, synchronous detection with pump source modulation and output modulation allows the decomposition of the different contributions to the output. The measured backward (A), forward (C), and amplified forward (B) ASEs are presented in Fig. 3.14. Summing backward (A) and amplified forward ASE (B) gives the combined spectrum (dotted line), which is in good agreement with the measured spectrum.

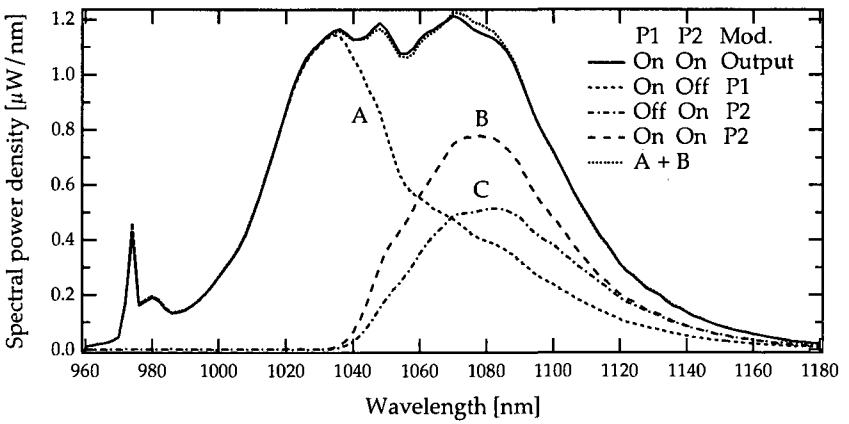

Fig. 3.14 ASE broadening using an umpumped region of the ytterbium doped fiber as spectral filter. The 10 m long fiber was pumped from both sides using two 980-nm laser diodes. (A), (B), and (C), represent the backward, the amplified forward, and forward ASE, respectively.

Individual control of the currents of the pump laser diodes allowed shaping the output spectrum. In the other hand, changing the pump wavelength by temperature monitoring of the pump 2 adds a degree of freedom for the forward ASE spectral shape. Ytterbium has a weak absorption bandwidth of the ytterbium-doped (10 nm) around the peak absorption at 976 nm. Small variations of the pump wavelength change fairly the absorption in the fiber. As a consequence, the fluorescent spectrum shape will change, as discussed in § 3.1.2. Setting pump 2 on and pump1 off, we measured the forward emission spectra for different pump wavelengths (see Fig. 3.15). The temperature of the pump diode was changed from 5°C to 28°C, shifting the pump wavelength from 970.2 nm to 977.1 nm.

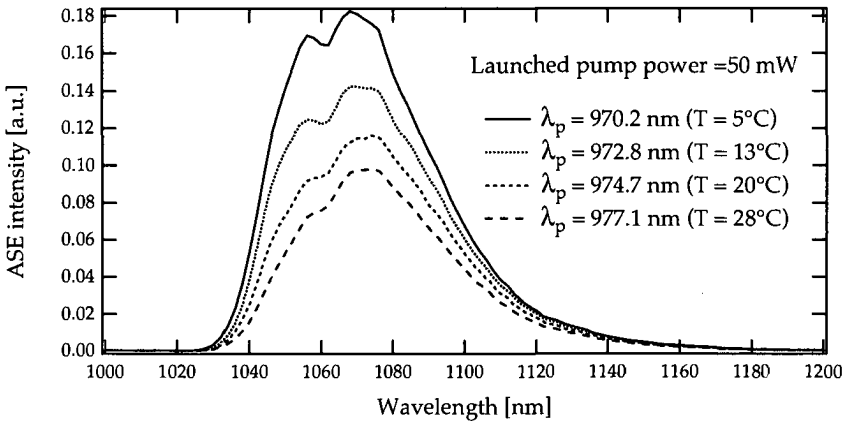

Fig. 3.15. Forward ASE spectra obtained from 10 m-long Yb^{3+}-doped fiber for different pump wavelengths λ_p.

The drive current was adjusted in order to keep the output pump power close to 50 mW for all settings of the temperature. At 977.1 nm, the absorption is 120 dB/m, and decreases to almost 50 dB/m at 970 nm, leading to a longer pump power distribution along the fiber. As a consequence, the signal output power increases, as shown in Fig. 3.15 and Fig. 3.2.

3.3.2 Long period grating as spectral loss-filter

Gain equalization is needed in communication system with cascaded fiber amplifiers. Equalization can be achieved by the use of integrated tunable Mach-Zehnder optical filters [38] [39]. As an alternative, Vengsakar *et. al.* [35] describe long periodic structure that couple guided fundamental mode to forward cladding modes. Since the coupling is wavelength selective, long period gratings (LPG's) act as wavelength-dependent loss elements. The most common use of LPGs is as spectral band-rejection filters for fiber

amplifier ASE and gain equalization [40] [41]. They are also used to remove high Stokes' orders in cascaded Raman amplifiers [42].

Tuning the spectral positions of the grating resonance peaks is possible by bending or heating the grating. Electrically tunable LPGs have been proposed as band-rejection filters [43]. The gratings are first coated with a thin metallic film of Ti/Pt or Ti/Al. An electric current applied on the external metallic layer heats the fiber cladding, modifying its refractive index. Consequently, the spectral transmission properties of the grating are modified, exhibiting linear wavelength shift of the resonance peaks.

We propose in this section a classical approach for spectral ASE broadening using a tunable band-rejection filter. The experimental setup consisting of a 1-m Er^{3+}-doped fiber as ASE source, the tunable LPG and a 1.5-m Er^{3+}-doped fiber as amplifier is shown in Fig. 3.16. The setup is similar to the dual-stage erbium doped fiber amplifier configuration with a passive filter, described in [44]. This experiment was realized in collaboration with the Institute of Applied Optics (IOA) of the Federal Institute of Technology in Lausanne (EPFL).

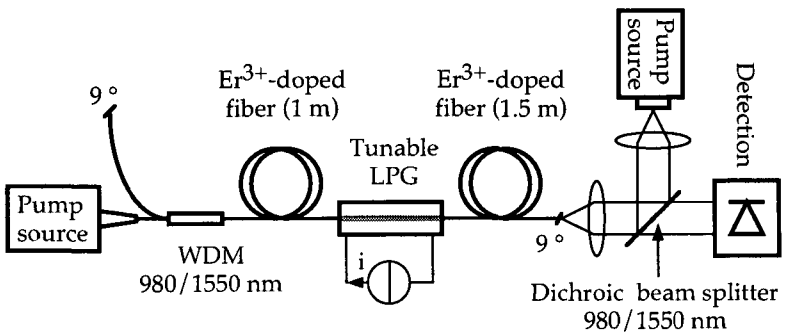

Fig. 3.16 Experimental set-up for a dual-stage Erbium-doped fiber source using a tunable metal-coated long period fiber grating (LPG) as wavelength-dependent loss filter.

The input-stage ASE source (left side of the LPG), forwardly pumped at 980 nm through a WDM coupler, exhibits an ASE emission spectrum with peak at 1530 nm. This spectrum is represented as solid line in Fig. 3.17. We spliced the LPG filter at the end of the fiber source and we measured the transmitted spectrum for different tunings. Transmitted spectra for 0 and 250 mW of applied electrical power are also reported in Fig. 3.17, as dotted and dashed line, respectively. As expected, the emission peak at 1530 nm of the input-stage source was strongly attenuated. The attenuation spectra of the LPG filter were calculated from the ratio between the transmitted emission spectra and the emission input spectrum (without the filter). These

attenuation spectra, which are reported in Fig. 3.17 as dashed-doted lines, reveal an effective loss of –4.6 dB at the resonant peak. The background loss of –4.2 dB is attributed to the field mismatch between the Er^{3+}-doped fiber and the fiber containing the LPG filter.

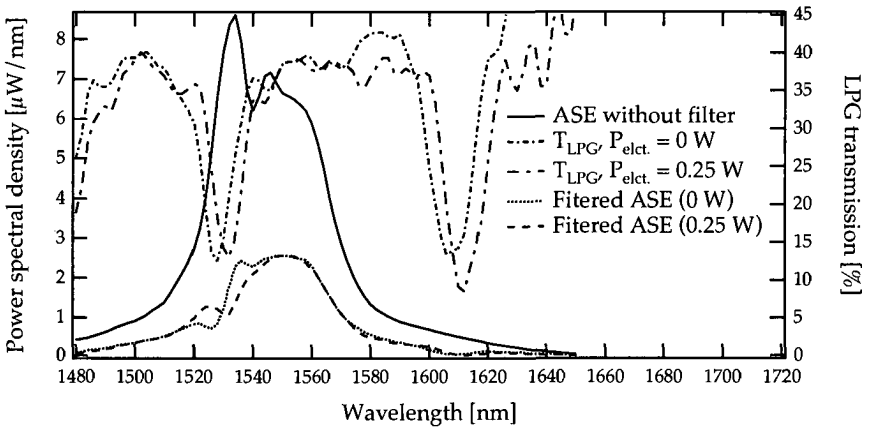

Fig. 3.17 ASE spectra before and after the grating for two different tunnings (0 mW and 250 mW electrical power). The corresponding attenuation spectra exhibit peak resonances around 1530 nm and 1610 nm.

The filtered ASE was then amplified through the 1.5 m long fiber on the right side of the LPG in Fig. 3.16. For more efficiency, this fiber was backward pumped through a dicroic beam splitter [45]. The resulting ASE was measured through a grating monochromator using synchronous detection. We report in Fig. 3.18 the spectrum resulting from the amplification of the filtered emission (solid line). The dashed line represents the filtered input ASE, for the grating tuned with 250 mW of electric power, taken from Fig. 3.17. The dotted line is the ASE from the backward pumped 1.5 m fiber without input signal from the first fiber (pump switched off).

Feeding the output stage by the filtered ASE stimulates the emission outside of the peak region at 1530 nm. Monitoring carefully the pump sources together with the tunable LPG allows to build up more output power and a larger spectrum of 40 nm FWHM centered at 1548 nm. The result presented in Fig. 3.18 was obtained by launching
30 mW of pump power in the input stage (left fiber) and almost 40 mW in the output stage (right fiber). These values correspond to the best compromise of large output power (0.83 mW) and small ripple (1.1 dB peak-to-peak).

We have shown that a tunable LPG filter between two pieces of erbium-doped fibers allows spectral emission shaping. In fiber communication systems, individual equalization of cascaded fiber amplifiers, improves the transmission distances, but increases the system complexity [46]. Active feedback control of the output spectrum by the tunable LPG could be also an advantage for some applications needing stable emission spectra, like interferometric fiber optic gyroscopes.

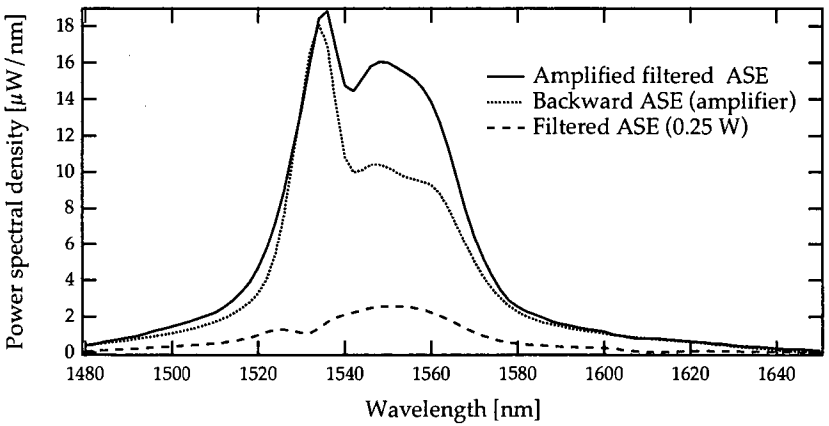

Fig. 3.18 Output spectra from the second (1.5 m long) fiber, with and without ASE input from filtered from input from the first (1m long) fiber. (the filtered input signal taken from Fig. 3.17 is indicated as dashed line).

3.4 Summary

Nd^{3+}-doped, Er^{3+}-doped and Yb^{3+}-doped broadband fiber sources have been demonstrated. Appropriate doped-fiber combinations have been tested, using ytterbium and neodymium. They have produced an emission with a FWHM of about 70 nm and single transverse mode power as high as 100 μW. Spectral filtering, before high power amplification rather than at the output, is another interesting approach to achieve broadband emission with high power density, even in single-pass regime. In the first approach, a long Yb^{3+}-doped fiber was pumped from both fiber-ends. The unpumped fiber length, located approximately in the midway of the fiber, was acting as spectral filter. In the second approach, a long period fiber grating was used as filter between two Er^{3+}-doped fibers. Both structures have been tested in single-pass configuration, and have produced quite large bandwidth. With the first approach, we obtained about 90 nm with a single transverse mode output power up to 120 μW. With the second approach, using the loss filter, we reached an output power of 0.85 mW with a spectral width of 50 nm.

Light emitting diodes (LEDs) have broadband emission spectra, but are spatially extended sources compared to mono-mode fiber light sources. More recently, commercially available fiber-pigtailed superluminescent diodes (SLDs) provide comparable characteristics to those obtained with doped fibers. They have moderate spectral widths (typically 30nm) and a typical powers of about 500 μW, but which can be also as high as 2 mW (Fermionics).

Finally, the radiance B, which expresses the power emission per steradian and square meter, and is related the power per mode by $P_{mode} = B \lambda_0^2$ are useful parameters to compare the coherence quality of different sources. For a single transversal mode source at 1 μm with an output power P of 700 μW the radiance B is $7\ 10^4$ W/sr cm^2. For comparison, the radiance and the power per mode of a blackbody radiation at a temperature T $\approx$ 3000°K at $\lambda_0 = 1$ μm, are only B = 7 W/sr cm^2 and $P_{mode} = 70$ nW, respectively.

4 Fiber Laser Oscillators

Because of their low loss and long interaction length, doped-fibers enable efficient laser cavity construction, exhibiting higher pump confinement, higher gain, and lower threshold compared to bulk lasers. Pure single-frequency operation with narrow linewidth has been demonstrated several times in fiber oscillator designs [47] [48]. This includes linear, ring, and traveling wave resonators. Single frequency laser sources are of great importance in many applications. Small size linear cavity lasers based on distributed Bragg reflector (BDR), and more recently distributed feedback (DFB) fiber laser sources, consisting of π phase-shifted fiber Bragg gratings (FBG) written into rare-earth doped fibers, are now commercially available with narrow line widths (few tens of kHz). Communication systems using wavelength division multiplexing (WDM) or coherent detection are concerned to a large extent by the technological progress made in this field.

Sensing is another domain that requires narrow line sources. These sources are principally used for interrogation of distributed passive fiber Bragg gratings along a fiber. Polarimetric sensors based on active cavities with RF frequency readout have been demonstrated for lateral pressure measurement [49]. Fiber DFB lasers are currently investigated as active sensor element for strain, temperature and acoustic vibration measurement.

This chapter is devoted to specific fiber oscillators and lasers, providing background information and theoretical modeling of optical fiber components used for the elaboration of fiber laser sources. Some examples are treated more specifically, and experimental results are compared with theoretical predictions, in terms of efficiency, loss, and polarization. Finally, linewidth measurements of fiber DFB lasers were performed by measuring beat spectra between a DFB fiber laser and a Nd:YAG solid-state laser, under different pumping conditions.

4.1 Fiber laser component characteristics

Doped fiber technology has brought an awesome range of fiber based components, including directional couplers, fiber Bragg reflectors, isolators, all-fiber modulators etc. Among this non-exhaustive list, fiber Bragg reflectors are worth to be described, as they play an important role in the elaboration of fiber resonators. Another important feature of fiber based resonators is the birefringence of the guiding medium, which imposes the resonator two resonant polarizations, called eigen-polarizations. In the following, we first present the fiber Bragg reflector and then the effect of the birefringence in doped fibers.

4.1.1 Fiber Bragg gratings (FBGs)

Intra-core phase gratings, written in photosensitive fibers by a spatially varying pattern of ultraviolet (UV) light, have been developed for many applications in fiber optic communication and sensor systems. For short grating periods, resonant coupling occurs between core modes traveling in opposite directions. These reflection gratings, which are called fiber Bragg gratings (FBG), provide serious advantages over competing technologies. The spectral characteristics of different fiber grating types are theoretically investigated in [50]. Fiber photosensitivity and fiber grating fabrication technology are treated in several other publications, such as [51] [52].

Coupled-wave theory is a powerful tool to calculate optical interactions in spatially or temporally perturbed media [53]. In 1969, Kogelnik presented coupled-wave solutions for diffraction of light by thick hologram gratings [54]. Following [50], we summarize in this section the coupled wave equations for fiber Bragg gratings.

In the unperturbed single-mode fiber, of the two waves traveling in opposite directions are described by

$$\begin{aligned} E_S(z,t) &= \exp\left(j\left(\omega t + \beta_S z\right)\right) \\ E_R(z,t) &= \exp\left(j\left(\omega t - \beta_R z\right)\right), \end{aligned} \tag{4.1}$$

where $\beta_S = -\beta_R$ are the corresponding propagation constants. In ideal fibers, these two waves do not exchange energy. We assume the presence of the grating can be described by a perturbation

$$\delta n_{eff}(z) = \overline{\delta n}_{eff}(z)\left\{1 + \upsilon \cos\left(\frac{2\pi}{\Lambda} z + \phi(z)\right)\right\}, \tag{4.2}$$

of the effective index of refraction, where $\overline{\delta n}_{eff}$ is the DC index change (spatially averaged over a grating period), υ is the modulation depth of the index change, Λ is the nominal period, and $\phi(z)$ represents a chirp.

The presence of this perturbation causes two waves E_S and E_R to be coupled and exchange energy. The resulting solution for the mode propagation with perturbation is then written as the linear superposition

$$E(z,t) = S(z)E_S(z,t) + R(z)E_R(z,t), \tag{4.3}$$

where $R(z)$ and $S(z)$ are the z-dependent complex amplitudes of the backward- and forward-traveling waves. Figure 4.1 illustrates the coupling of an incident mode by a Bragg grating into the same mode traveling in opposite direction.

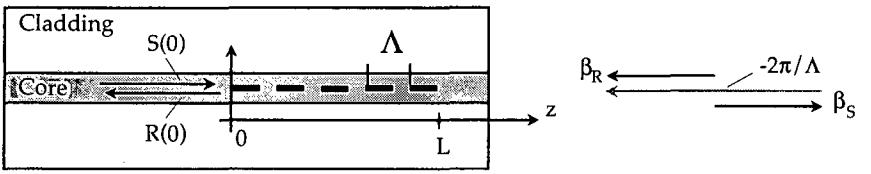

Fig.4 Fiber Bragg reflection grating of period Λ.

The complex amplitude R(z) and S(z) of the backward- and forward-traveling waves can thus be derived from the coupled-mode equation

$$\begin{aligned} \frac{dR(z)}{dz} &= i\acute{\sigma}R(z) + i\kappa S(z), \\ \frac{dS(z)}{dz} &= -i\acute{\sigma}S(z) - i\kappa^* R(z). \end{aligned} \tag{4.4}$$

Assuming that $\phi(\zeta) = 0$ (no chirp), $\acute{\sigma}$ represents the general self-coupling defined as

$$\acute{\sigma} = \sigma + \Delta k, \tag{4.5}$$

where σ is the DC coupling coefficient (period average) and Δk is the phase mismatch or the detuning defined as

$$\sigma = \frac{2\pi}{\lambda}\overline{\delta n}_{eff}, \text{ and } \Delta k = \frac{2\pi}{\Lambda} - \beta_R - \beta_S, \text{ respectively,} \tag{4.6}$$

And

$$\kappa = \kappa^* = \frac{\pi \overline{\delta n}_{eff}}{\lambda}, \tag{4.7}$$

is the AC coupling coefficient.

Form Eq. (4.5), we get that the maximum interaction occurs if $\hat{\sigma} = 0$. Since $\beta_S = -\beta_R = 2\pi/\lambda$, we get the familiar result

$$\lambda_B = 2\left(n_{eff} + \overline{\delta n}_{eff}\right)\Lambda \approx 2n_{eff}\Lambda. \tag{4.8}$$

for the design wavelength of the Bragg reflector.For wavelengths λ different from λ_B, the phase mismatch Δk can be expressed as

$$\Delta k = 2\pi\left(n_{eff} + \overline{\delta n}_{eff}\right)\left(\frac{1}{\lambda_B} - \frac{1}{\lambda}\right) \approx \frac{2\pi}{c} n_{eff}\left(\frac{1}{\lambda_B} - \frac{1}{\lambda}\right). \tag{4.9}$$

Equation (4.4), becomes a set of coupled first-order differential equation with constant coefficients, for which analytical solutions can be found, when appropriate boundary conditions are specified. Assuming $R(L) = 0$, the amplitude of the reflection coefficient $\rho = R(0)/S(0)$ becomes

$$\rho = \frac{-\kappa \sinh\left(\hat{s}L\right)}{\hat{\sigma}\sinh\left(\hat{s}L\right) + i\hat{s}\cosh\left(\hat{s}L\right)}, \text{ with } \hat{s} = \sqrt{\left(\kappa^2 - \sigma^2\right)}. \tag{4.10}$$

The power reflection coefficient (reflectivity) and phase of the reflection coefficient are

$$r = |\rho|^2 = \frac{\sinh^2\left(\hat{s}L\right)}{\cosh^2\left(\hat{s}L\right) - \frac{\hat{\sigma}^2}{\kappa^2}}, \tag{4.11}$$

$$\varphi_\rho = angle(\rho) = \arctan\left[\frac{\hat{s}}{\hat{\sigma}}\coth\left(\hat{s}L\right)\right]. \tag{4.12}$$

Finally, we introduce the group delay τ, which is the first derivative of the phase with respect to the frequency. We have

$$\tau = \frac{d\varphi_\rho}{d\omega} = -\frac{\lambda^2 n_{eff}}{2\pi c}\frac{d\varphi_\rho}{d\lambda}. \tag{4.13}$$

A typical example of power reflectivity r and group delay τ, for $\kappa L \approx 2$ and $\Lambda \approx 0.5\mu m$, is shown in Fig. 4.2. The length of the FBG is 15 mm.

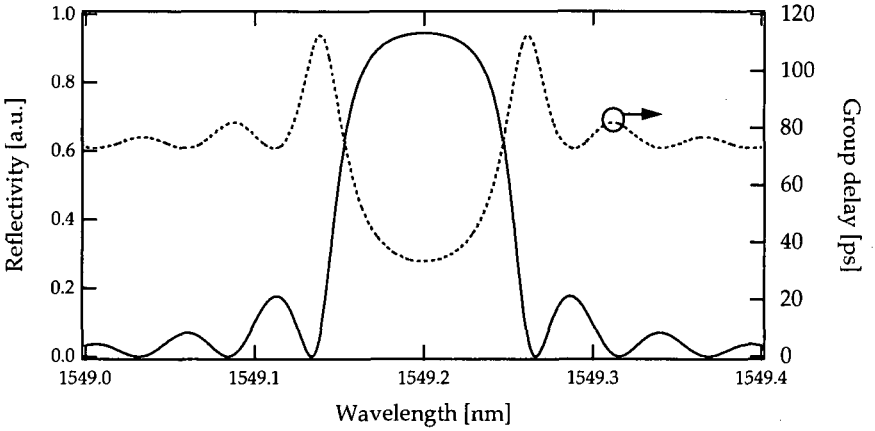

Fig. 4.2 Reflection spectrum and group delay versus wavelength for a 15 mm-long uniform FBG, with $\kappa L \approx 2$.

Compared to dielectric mirrors, the modulation of the index refraction is very small in FBGs. To achieve high reflectivity, long interaction length is therefore necessary for FBGs , making them somehow more dispersive than dielectric mirrors. This dispersion in FBGs can be exploited for sensing using a short active or passive Fabry-Pérot cavity. Such a sensor will be described the next chapter 5, and tested with a highly dispersive FBG.

4.1.2 Birefringence in standard Nd^{3+}-doped fiber

Doped fibers, and more generally standard optical fibers, with nominal circular symmetry about the fiber axis exhibit anisotropies due to imperfections introduced during the fabrication process. Thus, non-ideal fibers must be treated as birefringent materials. The fibers can be considered as a sum of many pieces of bimodal fiber with stochastically distributed birefringence. These polarization variations are analyzed and discussed in [55]. Since every piece of fiber is different and may vary with time, an ensemble average over the whole fiber length should be measured or calculated. The problem of mode coupling by random perturbations has been treated by Marcuse [56], and adapted to polarization mode analysis in [57].

We assume that a piece of loss-free birefringent fiber can be described by linear retarder plate followed by an optical activity α. The fast axis of the retarder plate is rotated by an angle θ with the Ox axis and the retardation is equal to δ. The Jones matrix representation of the fiber piece can be written according to [58],

$$M_i = R^{-1}(\theta_i)\, B(\delta_i)\, R(\theta_i)\, A(\alpha_i) = R^{-1}(\theta_i)\, B(\delta_i)\, R(\theta_i + \alpha_i), \tag{4.14}$$

where

$$A(\alpha)=\begin{pmatrix}\cos\alpha & \sin\alpha\\ -\sin\alpha & \cos\alpha\end{pmatrix}, \tag{4.15}$$

describes the rotation introduced by the optical activity α, and the product

$$R(\theta)\,B(\delta)\,R^{-1}(\theta)=\begin{pmatrix}\cos\theta & \pm\sin\theta\\ \sin\theta & \cos\theta\end{pmatrix}\begin{pmatrix}\exp(-j\delta) & 0\\ 0 & \exp(j\delta)\end{pmatrix}\begin{pmatrix}\cos\theta & \sin\theta\\ \pm\sin\theta & \cos\theta\end{pmatrix}, \tag{4.16}$$

corresponds to the equivalent birefringence retardation 2δ with its axis oriented at the angle θ with respect to the reference frame. As the birefringence varies statistically along the fiber, the Jones matrix representation, of an ensemble average over the whole fiber length, take the same form as M_i. We have

$$M=\prod_i M_i = R^{-1}(\theta)\,B(\delta)\,R(\theta+\alpha). \tag{4.17}$$

In an orthogonal right-handed Cartesian coordinate system, the electric field vector of a propagating monochromatic wave along the fiber is given by the two components E_x and E_y

$$\mathbf{E}(z,t)=\begin{bmatrix}E_x(z,t)\\ E_y(z,t)\end{bmatrix}=\begin{bmatrix}A_x\exp\left[j(\omega t-\varphi_x)\right]\\ A_y\exp\left[j(\omega t-\varphi_y)\right]\end{bmatrix}, \tag{4.18}$$

where $A_{x,y}$ and $\varphi_{x,y}$ represent the amplitude and the phase of the electric-field components along the x and y axes, respectively, and the element of the Jones vector

$$J=\begin{bmatrix}A_x\exp(j\varphi_x)\\ A_y\exp(j\varphi_y)\end{bmatrix}. \tag{4.19}$$

gives a complete information about the amplitude and the phase of the field components, hence the state of polarization (SOP) of the wave. We can introduce a single complex number χ resuming the SOP of the wave at any z-position along the fiber, defined as the ratio E_y/E_x between the phasor components of the Jones vector. We have

$$\chi=\frac{A_y}{A_x}\exp\left[j(\varphi_y-\varphi_x)\right]=\frac{A_y}{A_x}\exp\left[jk_0(\Delta n)z\right], \tag{4.20}$$

where Δn is the difference between the refractive index averaged over the fiber length, $k_0 = 2\pi\nu_0/c$ the wave number in the free space. We note B_f, the linear birefringence expressed as the difference between the refractive index of the equivalent zx and zy planes decomposition.

$$B_f = n_y - n_x = \Delta n \tag{4.21}$$

The value of linear birefringence B_f in fibers can range from 10^{-9} in low-birefringence (Lo-Bi) fibers to $B_f = 10^{-3}$ in high birefringence (Hi-Bi) fibers. Measurements of static birefringence can be accomplished by rotating polarizers and analyzers, supplemented by a Babinet-Soleil[1] compensator to enhance the performance of the measurement. With this setup the accuracy and sensitivity for retardation measurement is limited to about 0.2 rad for static birefringence. Improved sensitivity is obtained by modulating the birefringence, e.g. with a photo-elastic modulator [59]. We have used both to measure the birefringence in Nd^{3+}-doped fibers. The results are in good agreement, since the birefringence B_f was in the range of 10^{-6}, and thus accessible also by the first method. With the second method, five samples of each fiber have been measured to get an ensemble average. We found $B_f = 3.7\ 10^{-6}$, and $B_f = 8.8\ 10^{-6}$ for the fibers type Nd-160491 and Nd-100192B, respectively.

Control of the SOP of output signals is important in many applications, i.e. coherence communication using fiber amplifier [60]. The two normal mode components are coherently related as long as delay difference between their transit times is less than coherence time of the injected source. The maximum fiber length for which this coherence is hold, is approximately [61]

$$L_c \approx \frac{c\tau_c}{B_f}, \tag{4.22}$$

where, τ_c is coherent time, inversely related to the spectral width, and c has its usual meaning. For doped fiber having a birefringence in the range of $5\ 10^{-6}$, the corresponding values of L_c with 1 μm light sources, having spectral widths of 10 nm (superfluorescent fiber source), and 0.1 nm (fiber laser), are 20 m, and 2 km, respectively.

4.1.3 Polarization eigen-states in Fabry-Pérot fiber lasers

With reciprocal optical activity, the matrix representation of the total round trip through the same fiber is simply given by

---

[1] The compensator consists of a single mode fiber section clamped inside a fiber squeezer, which can be rotated about the fiber with respect of a left and a right fiber holder

$$M_c = S\,R^{\pm 1} B\,R\,A\,S\,A\,R\,B\,R^{-1}, \tag{4.23}$$

where

$$S = \begin{pmatrix} \pm 1 & 0 \\ 0 & 1 \end{pmatrix}, \tag{4.24}$$

is the matrix representation of an ideal mirror. The product of Eq. (4.23), which gives after expansion

$$M = \begin{pmatrix} \cos\theta & -\sin\theta \\ \sin\theta & \cos\theta \end{pmatrix} \begin{pmatrix} \exp(-j2\delta) & 0 \\ 0 & \exp(j2\delta) \end{pmatrix} \begin{pmatrix} \cos\theta & \sin\theta \\ -\sin\theta & \cos\theta \end{pmatrix}, \tag{4.24}$$

correspond to a linear retardation of 4δ with its axis orientated at an angle of θ. The eigen-values of this matrix are $\lambda_{1,2} = exp(\pm j2\delta)$ and the corresponding eigen-vectors are two orthogonal linear polarizations oriented at θ and $\theta+\pi/2$, respectively. Therefore two orthogonal modes, in free-loss birefringent cavity with reciprocal optical activity and ideal mirror, are always linearly polarized.

4.2 Single-mode fiber Fabry-Pérot oscillators

4.2.1 Fiber Fabry-Pérot oscillator with dielectric mirrors

The Fabry-Pérot laser, which consists of an active medium with mirrors at each end, is the most common laser design. The first reported device based on rare-earth doped-fibers was a cw Nd-doped fiber laser operated at 1088 nm [62]. Fiber ends were mounted against bulk dicroic mirrors. The threshold was remarkably low, at 100 μW of absorbed pump power. Laser oscillations occur when the gain equals the round-trip loss of the cavity. This means, that with a gain coefficient of 0.4 dB/mW, 1 mW of absorbed pump power is sufficient to reach the threshold in fiber cavities with total losses of 0.4 dB (10%).

We report a similar fiber laser fabricated with 1 m-long Nd-doped fiber (Tab. 2.2, type Nd-060592), using two dielectric reflectors having 99% and 90% of reflectivity at the input-end, and at the output-end fiber, respectively. Light at 805 nm from a diode laser was launched into the fiber, which gives laser emission at 1060 nm.

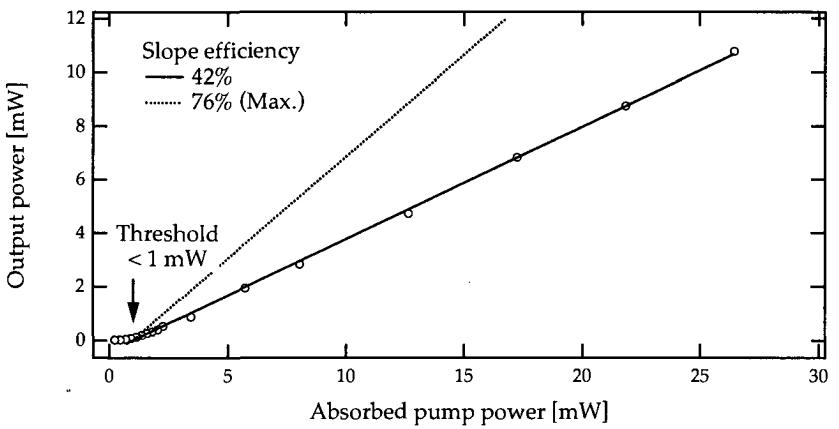

Fig. 4.3 Output power versus absorbed pump power for a Nd-doped fiber (Tab. 2.2, type Nd-060592). The slop conversion efficiency is 42% and the threshold is less than 1 mW of absorbed pump power.

The reflectors were sufficiently small (2x2mm) and thin (300 μm), to be glued at each fiber end facet. The measured output power as a function of the absorbed pump power in presented in Fig. 4.3. A slope conversion efficiency of about 42% has been reached. Higher conversion efficiency, approaching the quantum limit of $\lambda_{pump} / \lambda_{signal} = 76\%$, is

reported in the literature for fiber-end facets directly coated with highly reflective dielectric layers [63].

Above the threshold, when the transmission T_{out} of the output coupler is small, the two counter-propagating signal distributions become independent of z, and saturation terms are constant. Under this approximation, Digonnet shows that the laser output power P_{out} grows linearly with the absorbed pump powers P_{abs} [10]. This is confirmed by the result in Fig. 4.3. The slop conversion efficiency can be written as

$$\eta = \frac{P_{out}}{P_{abs} - P_{th}} = \frac{T_{out}}{\delta}\eta_{\lim}, \tag{4.25}$$

where P_{th} is the pump threshold, $\eta_{\lim}$ the quantum limit defined as the ratio $\lambda_{pump}/\lambda_{signal}$, and δ the cavity round trip loss.

There are mainly three sources of cavity losses: losses attributed to the ground state absorption, which are associated to the absorption coefficient α_s; losses, arising from the mirror transmissions, $-(1-R_1R_2)$, and losses including scattering and coupling losses at fiber-end and mirror interfaces δ_c. The round trip loss is then given by

$$\delta = 2d\alpha_s + \delta_c - (1 - R_1R_2), \tag{4.26}$$

where R_1 and R_2 are the mirror reflectivities. R_2 is taken as the output coupling mirror, and d is the fiber cavity length.

Assuming no signal ground state absorption (four-level systems), the losses originate essentially from the output mirror transmission and from mirror misalignments. These losses can be calculated with Eq. (4.25), from the measured slope efficiency η. Regarding to the reported result in Fig. 4.3, we have δ = 18%. Since the losses from output mirror transmission are about 11 %, we can deduce from (Eq. (4.26)) that the losses by mirror misalignment δ_c *are* about 7 %.

The threshold condition for a four-level fiber laser can be given by equaling the small-signal gain integrated along the round trip cavity with the total loss. We have according to Eq. (2.44)

$$\exp(2\Gamma_0 d) - 1 = G_0(d) - 1 = \delta. \tag{4.27}$$

For the Nd^{3+}-doped fiber used above, 0.4 dB/mW of small-signal gain has been measured in [24]. We can calculates pump threshold P_{th}, using Eq. (4.27) and the round trip loss d. We found P_{th} = 930 μW. This result correspond fairly to the measured value of less 1 mW, as shown in Fig. 4.3. On the other hand, Digonnet gives an expression of the pump threshold for lasers with a reasonably high gain per unit pump power and a small cavity loss

$$P_{th} = \frac{h\nu_p}{\sigma_s \tau} \frac{A_{eff}}{\eta_c} \frac{\delta}{2}. \tag{4.28}$$

where η_c the pump conversion efficiency and A_{eff} is thee effective mode area. An approximated calculus can be done by assuming A_{eff} equal to the core area equal (19.6 μm^2, for Nd-060592) and by taking the typical value of 0.6 for η_c, we find $P_{th} = 760\ \mu W$.

The fiber laser cavity used above support a large number of longitudinal modes. The resonance frequencies of the Fabry-Pérot are given by

$$\nu_m = \frac{c}{2n_{eff}d} m, \tag{4.29}$$

where m is an integer, n_{eff} is the effective fiber core refractive index, and d the cavity length. The spacing between the longitudinal modes is know as the free spectral range (FSR) and is given by

$$FSR = \frac{c}{2n_{eff}d}. \tag{4.30}$$

According to Eq. (4.30), the number of modes susceptible to oscillate depends on the spectral width of the gain and the fiber length d. This number can be strongly reduced by shortening the cavity length and using narrow bandwidth reflectors, such as FBG or bulk grating in Littrow configuration [64].

4.2.2 Fabry-Pérot laser with Bragg grating reflectors

Replacing bulk dielectric mirrors with fiber Bragg gratings, simplifies the construction and the application of fiber lasers. Short monolithic Fabry-Pérot laser can be built by fusion-splicing two fiber pieces containing the gratings reflectors to a short section of doped fiber. Of course, photosensitive germanium-doped active fibers, into which FBG are directly written, are preferable. Direct Bragg grating inscription enable precise cavity design. For spectral mode selection in coupled cavities [65] [66], fiber length is an important parameter, which can be mastered by this technique. Moreover, direct Bragg grating inscription in doped fiber enables distributed feedback (DFB). DFB fiber lasers are important devices, which operate robustly with narrow linewidth. They found application as sources or as sensing elements. In the following we shall present spectral and polarization properties of Fabry-Pérot fiber lasers with Bragg grating reflectors as mirrors.

4.2.2.1 Single-frequency operation

Single-frequency operation in Fabry-Pérot configuration is possible to achieve with short cavity lengths and highly selective bandwidth reflector like FBGs. An important

issue with single-mode lasers, however, is their polarization properties. Polarization mode discrimination is possible with pump polarization orientation. The threshold is maximum and the slope efficiency minimum for output polarization that is perpendicular to the pump polarization [67]. Near the laser threshold and for short cavity lengths, truly single frequency laser operation can be observed.

A short Fabry-Pérot cavity was built, using a 12-mm long highly doped neodymium-fiber (Nd-160491), as shown in Fig. 4.4. The feedback mirrors are realized by fusion splicing to the doped-fiber two fiber Bragg gratings FBG_1 and FBG_2, having power reflectivities of $R_1 = 92\%$ and $R_2 = 90\%$, respectively. The spectral responses of the Bragg reflectors were both centered at 1064.07 nm with a bandwidth of 0.1 nm (FWHM).

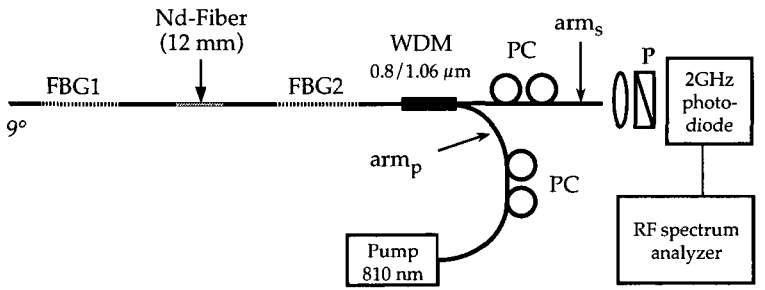

Fig. 4.4 Short Fabry-Pérot using a 12 mm long highly doped neodymium-fiber (Nd-160491) and identical fiber Bragg gratings (FBG_1 and FBG_2)

The cavity length was about of 55 mm, which yields with Eq. (4.26) of free spectral range (FSR) of 1.8 GHz. From a 810 nm diode laser, 50 mW pump power could be launched into the fiber laser through an 0.8/1.06 μm wavelength division multiplexer. The polarization of the pump at the input arm_p and the polarization of the signal from the output arm_s were controlled using all-fiber polarization controllers (PC in the Fig. 4.4). The output signal was detected with a 2 GHz-bandwidth InGaAs-photodiode, followed by a RF spectrum analyzer or an 8 GHz-FSR scanning Fabry-Pérot analyzer.

The measured laser output power is plotted in Fig. 4.5, as function of the absorbed pump power. The lasing threshold is achieved with 7.5 mW of absorbed pump, and the slope efficiency is about of 22%. This threshold is relatively high, because of the poor gain provided by the fiber. The small signal gain has been measured as 0.06 dB/1 mW of absorbed pump power. We have chosen this fiber because the short cavity length requires a highly absorptive fiber for the pump. The chosen fiber absorbs 470 dB/m at 805 nm.

Neglecting pump saturation, the 12-mm section absorbed about 70 % of the pump power (5.6 dB attenuation). High absorption means that the fiber is highly doped (10^4 ppm).

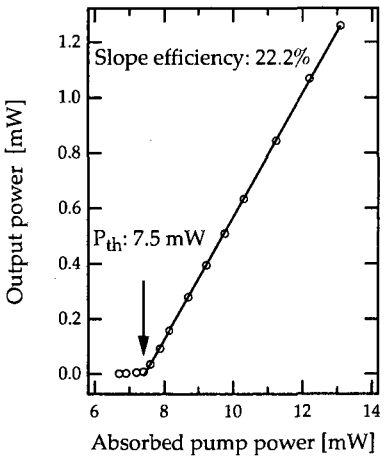

Fig. 4.5 Output power of a 55 mm long highly-doped Nd^{3+}-fiber laser

At high doping concentrations, however, clusters induce quenching, which reduce the gain. The tradeoff is between sufficient gain to achieve threshold and relatively low pump power. Although the FBG reflectors have 0.1 nm-bandwidth (FWHM), which corresponds to almost 20 FSR, the scanning Fabry-Pérot analyzer revealed only two longitudinal modes near the threshold and three modes at higher pump levels (launched pump power > 20 mW). We measured with the RF spectrum analyzer the first order longitudinal mode beat frequency (LMB) at 1814 MHz, in agreement with Eq. (4.30)

Polarization beat frequency between the eigen-polarization modes of the laser emission was investigated. In order to get beat frequency between polarization modes, assumed linear regarding to the theoretical prediction in 4.2.1, the orientation of the polarizer and the state of polarization of the output fiber arm_s (60 cm) was modified to get a maximal signal intensity in the RF spectrum analyzer. When the polarization was rotated by 45°, the beat signal tended to disappear, This observation however, can not confirm the theoretical prediction in 4.2.1, that the eigen-polarizations are linearly polarized, because of the change of the polarization introduced by the output fiber arms.

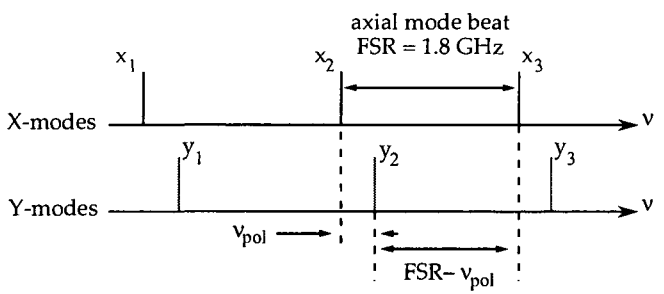

Fig. 4.6 Resonance frequencies of each eigen-polarization mode and their beat frequencies

The schematic representations of the three axial modes of the fiber laser for each eigen-polarization are shown in Fig. 4.6. We assume the same axial mode spacing (FSR) for the two polarization modes and we neglect the dispersion introduced by the Bragg grating reflectors. Polarization mode beat (PMB) frequencies appear at symmetric places ν_{pol} and $\nu - \nu_{pol}$, around adjacent axial or longitudinal mode beat (LMB) frequencies ν. As the laser is multi-modes (axial), PMB frequencies should appear at

$$\nu_{pol} = m(FSR) \pm \nu_{pol} = \nu_m \pm \nu_{pol}, \text{ with } m = 0, 1, 2. \tag{4.31}$$

The origin of the beat frequencies is summarized as couples of resonance frequencies, according to Fig. 4.6.

LMB frequency		PMB frequency				
ν_1	ν_2	ν_{pol}	$\nu_1 - \nu_{pol}$	$\nu_1 + \nu_{pol}$	$\nu_2 - \nu_{pol}$	$\nu_2 + \nu_{pol}$
(x_1,x_2) (x_2,x_3) (y_1,y_2) (y_2,y_3)	(x_1,x_3) (y_1,y_3)	(x_1,y_1) (x_2,y_2) (x_3,y_3)	(x_2,y_1) (x_3,y_2)	(x_1,y_2) (x_2,y_3)	(x_3,y_1)	(x_1,y_3)

Tab. 4.1 Summary of the origin of beat frequencies as couple of frequencies of Fig.4.6.

For m = 0, only positive value of $\Delta\nu_{pol}$ is taken into account. The polarization beat frequency can be approximate by [49]

$$\Delta\nu_{pol} = \frac{c}{2n_{eff}d}\frac{\Delta\phi}{2\pi} = (FSR)\frac{\Delta\phi}{2\pi}, \tag{4.32}$$

where $\Delta\phi$ is the relative phase shift induced by the birefringence in the cavity. At room temperature and without external perturbation on the fiber laser, we observed three PMB frequencies with the first PMB frequency at 53 MHz. The remaining two PMB frequencies (above 2.5 GHz) are truncated by the frequency band-bass of the detection.

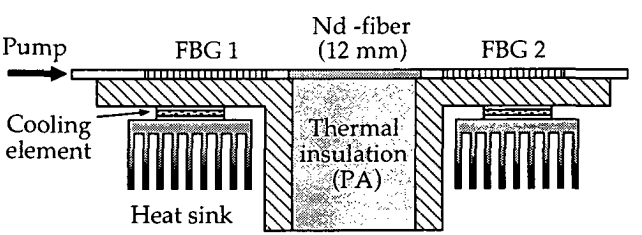

Fig. 4.7 Experimental structure with individual temperature control forth two gratings

The Bragg wavelength is affected by external perturbations, such as strain, pressure, or temperature. When the FBG is heated, the Bragg wavelength is shifted towards longer wavelengths. The shift is essentially caused by the change of refractive index and, to a slighter extent, by the linear thermal expansion of the optical fiber. Typically, a shift of 0.01 nm/°C is observed for gratings at 1.3 μm.

Using this property, we heated one of the two gratings to detune the reflection spectra of the two Bragg mirrors. As expected, detuning the reflection spectra produced a better spectral filtering of the laser emission. As shown in Fig. 4.8, the temperature of each fiber grating was controlled individually by Peltier cooling elements. The temperature of FBG1 could be changed from 10 °C to almost 65 °C. The temperature of FGB2 was kept at 21 °C. As shown in Fig. 4.8, when the spectral response of FBG1 was shifted, the laser was forced to operate within the common area of the two reflection spectra (dotted pattern).

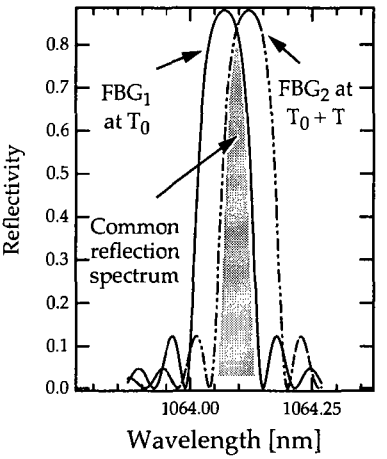

Fig. 4.8 Simulation of reflection spectra detuning due to thermal shift

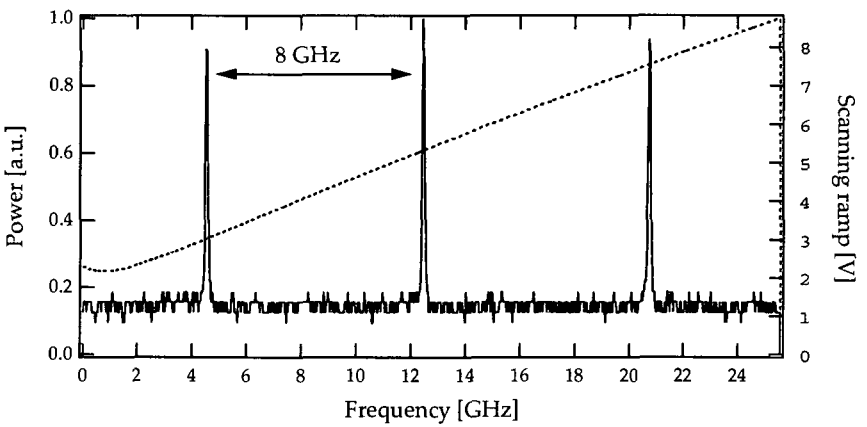

Fig. 4.9 Scanning Fabry-Pérot analysis (FSR = 8 GHz) showing single-frequency operation of the 55 mm long Nd^{3+}-fiber laser

The intersection point of the two reflection spectra gives the maximum reflectivity, from which the reflectivity decreases rapidly. We note that the top of the synthetic

spectrum becomes sharper and the cavity loss, which is a function of the reflectivity, becomes more significant with increasing shift. As the temperature on FBG1 increased, the number of modes (three at the beginning) decreased and reached one for a detuning of about 0.07 nm. Under this condition, no axial mode beating was observed in the electronic signal. The analysis with the 8 GHz scanning Fabry-Pérot (Fig 4.9) shows relatively stable single-frequency laser-operation. When the shift exceeds 0.07 nm, corresponding to a temperature-raise of 9°C, the laser stopped oscillating.

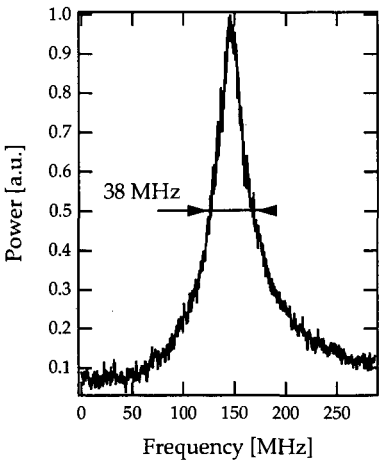

Fig.4.10 Scanning Fabry-Pérot analysis of one resonance. The measured linewidth is limited by the resolution of the scanning Fabry-Pérot

At this stage, however, one polarization mode beat frequency was still observed, revealing two eigen-polarizations. The 53 MHz difference between the two polarization modes was hardly resolved by the Fabry-Pérot analyzer of resolution of 38 MHz. Pure single-frequency (single-polarization) laser operation was obtained near the threshold with the help of the input pump polarization controller, which favors one of the two polarization modes in the cavity. The scanning Fabry-Pérot of one resonance is plotted in Fig. 4.10. The observed linewidth is limited by the resolution of the scanning Fabry-Pérot, which is about of 36 MHz (finesse ≈ 230).

Single polarization emission was verified by the absence of the polarization beat frequency in the photo-detector signal, monitored with the RF spectrum analyser. Pure single-frequency laser however, was difficult to maintain over periods of time longer than 3 to 5 seconds.

4.3 Distributed feedback (DFB) fiber laser

Contrary to the DBR laser geometry discussed in 1.2.2, the distributed feedback (DFB) consists of a doped fiber with a Bragg grating, into which π phase-shift is introduced at midway. The resulting DFB laser can operate robustly in a single axial mode. DFB lasers find applications as narrow sources for fiber communication or for interrogation of passive FBG sensors. They are now also investigated as active sensor elements [68]. Ytterbium doped DFB lasers operating at 1.06 μm with narrow linewidth emission became recently commercially available. In the context of coherent communication, fiber DFB lasers may replace bulk Nd: YAG lasers. However, their linewidth must be sufficiently stable and small, so that frequency locking between two lasers is possible.

4.3.1 Linewidth measurement of DFB fiber laser

Using a low frequency optical phase locked loop (OPLL), we measured beat spectra between a DFB fiber laser and a Nd: YAG solid-state laser and made comparison with the beat spectra obtained from two Nd: YAG lasers. The experimental set-up is shown in Fig. 4.11. To compensate for the wavelength mismatch between the Nd: YAG and the fiber lasers, we tuned the fiber lasers either by changing the temperature or by stretching the DFB fiber lasers.

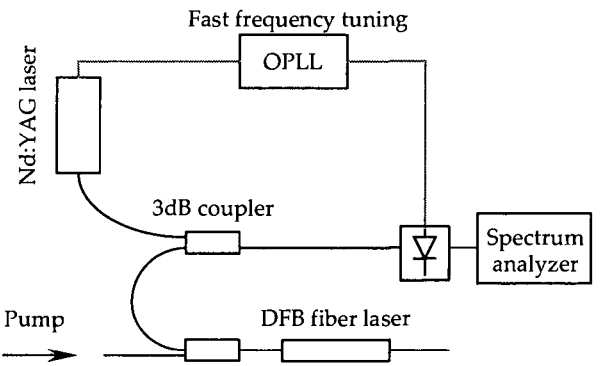

Fig. 4.11 Setup for DFB fiber laser linewidth measurement.

For comparison, we measured beat spectra between the Nd: laser available at IMT (Lightwave Technology model 125/6) and another Nd:YAG laser from Contraves Space AG. We measured also the beat spectrum between two Nd:YAG lasers of the same type, available from Contraves. In each case, the lasers are frequency locked, using an OPLL with 2.5 kHz bandwindth. By fitting a Lorentzian curve to the data, we obtained

a full width at – 3 dB of 9 kHz and 4.5 kHz, respectively. The results are shown in Fig. 4.12.

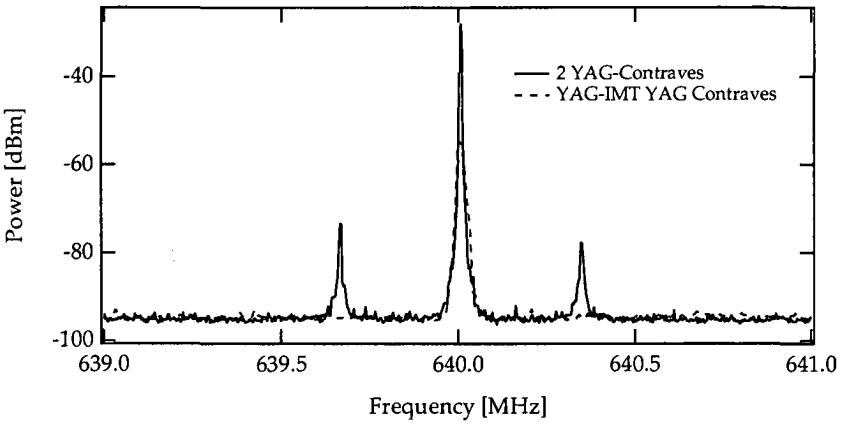

Fig. 4.12 Beat spectra obtained with two Nd:YAG lasers.

We used two different DFB ytterbium doped fiber laser (S/N IFL 1124 and S/N IFL 1125) manufactured by Ionas A/S, Denmark. Their linewidth is specified to be smaller than 50 kHz. In a first experiment, both DFB lasers were pumped at 977 nm with thermal stabilization of the pump wavelength. Laser 1125 was stretched, while laser 1124 was placed in an oven at a temperature of about 85 °C. They were frequency locked to the Nd:YAG laser available at the IMT.

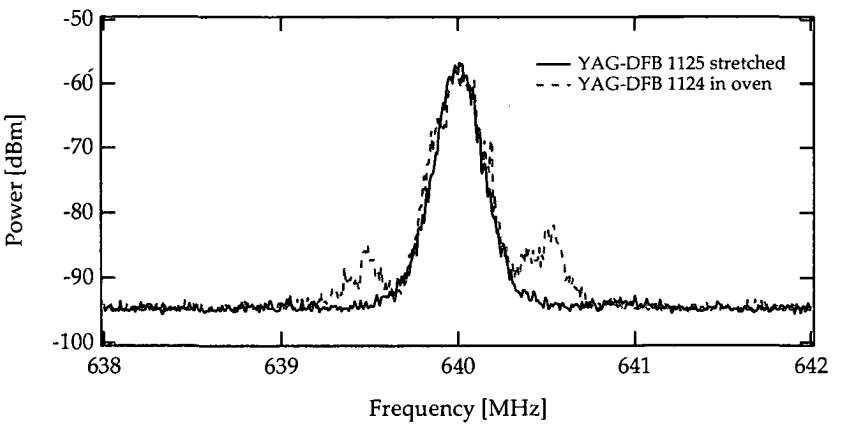

Fig. 4.13 Beat spectra for two different DFB fiber lasers with the same Nd:YAG laser. Tuning was realized by heating or stretching the DFB lasers 1124 and 1125, respectively.

Frequency noise in fiber lasers, and more especially in DFB lasers, is essentially attributed to pump fluctuation, and to acoustical vibrations [69]. Therefore, particular care has been taken to limit frequency noise due to acoustical vibrations. The resulting beat spectra are shown in Fig. 4.13. By fitting a Lorentzian line, we obtained a full width (– 3 dB) 80 kHz for the stretched laser 1125 and 100 kHz for the laser 1124 in the oven, respectively. These results confirm that the two fiber lasers are very similar and that tuning either by heating or stretching does not change the stability of the fiber lasers.

4.3.2 Influence of pump frequency stability versus DFB linewidth

Fluctuations in the pump intensity may cause laser intensity noise, which leads to frequency noise according to the frequency to intensity noise ratio at low frequency and according to the linewidth enhancement factor at frequencies close to the relaxation oscillation frequency ([70], pp. 46 - 52). Fluctuations of the pump center wavelength also lead to fluctuations in the pump conversion efficiency due to the wavelength dependence of the pump absorption. Until recently, available fiber pig-tailed pump diode lasers were not grating-stabilized. Although the temperature and the drive current were stabilized in our pump source, a typical value of 150 GHz (0.5 nm) instability, integrated over 60 sec, was observed. As ytterbium has a strong and narrow absorption, the laser fluctuations are significant when the pump wavelength fluctuates close to the peak absorption.

In order to investigate the effect of pump wavelength on the beat spectrum, we changed the pumping condition of the stretched laser 1125.

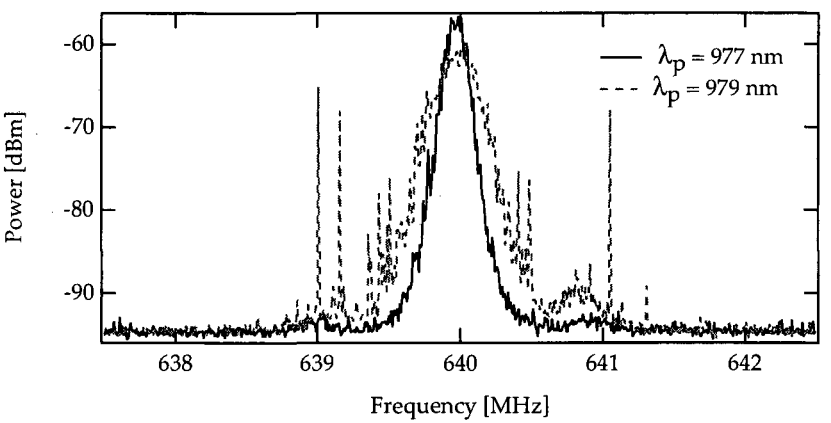

Fig. 4.14 Beat spectra of the same fiber laser 1125 and a Nd:YAG for two different pumping wavelengths.

By changing the pump power or the temperature of the pump diode, the pump wavelength could be shifted by several nm. We measured beat spectra for two different values of pump wavelengths, namely 977 nm and 979 nm. It is obvious from the results shown in Fig. 4.14, that the pumping condition has an influence on the laser linewidth.

In a second experiment, we pumped the stretched DFB laser with a 975 nm grating-stabilized pump laser diode. Such pump lasers are now commercially available at 980 nm and at 1480 nm, and they are used to pump low noise fiber amplifiers. We observed a significant narrowing of the linewidth beat spectrum between the DFB and the Nd:YAG laser. Compared to the 80 kHz linewidth obtained with a standard pump laser, we got 46 kHz linewidth using a grating stabilized pump laser. This linewidth corresponds fairly well to the specification of the DFB fiber laser by the supplier. Moreover, the beat spectrum with the grating-stabilized pump laser approaches the expected natural Lorentzian lineshape for laser emissions. For comparison, Fig. 4.15 shows the beat spectra obtained with the stretched DFB laser pumped with a standard laser diode (Fig. 4.14, λ_p = 977 nm) and the grating-stabilized laser diode, as well as the beat spectrum of 4.5 kHz obtained with two identical Nd:YAG lasers.

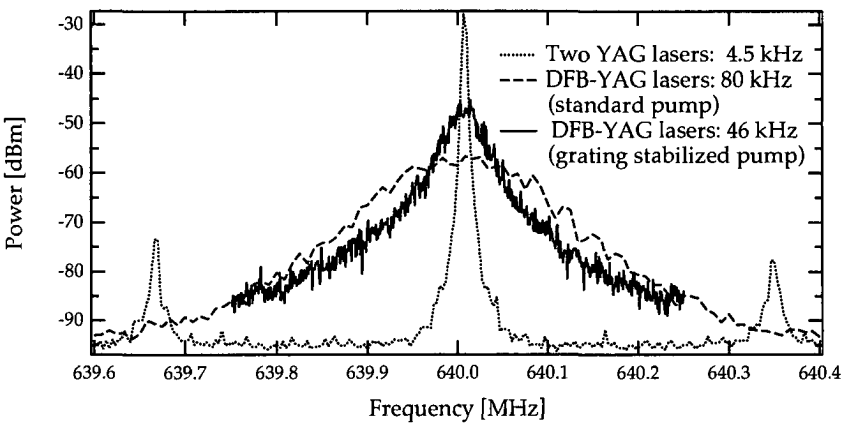

Fig. 4.15 Comparison of beat frequencies obtained for the DFB fiber laser with different pump diodes and for two Nd:YAG lasers.

For coherent communication, where master oscillators are locked together, the linewidth is an important parameter. Following a rule of thumb, the bandwidth of the OPLL regulation is given by the width of the beat spectra at 30 to 40 dB below the peak. The required bandwidths, according to Fig. 4.15, are 540 kHz, 270 kHz and 16 kHz at – 30 dB, for DFB fiber laser without grating, DFB fiber laser with grating stabilized pump source and Nd:YAG lasers, respectively.

Frequency stabilization of DFB fiber lasers with a bandwidth of 1 MHz seems to be difficult, and therefore DFB fiber lasers cannot replace directly Nd:YAG lasers. Moreover, we have demonstrated, by these experiments, that the intensity noise of the pump diode broadens the width of the beat frequency. Thus the pump stability may be an issue to get more stable DFB fiber laser for coherent communication. On the other hand, the piezoelectric coating used for the phase modulator in an all-fiber MOPA [43] may be a solution for fast tuning of the laser frequency. Though not demonstrated yet, this approach seems to fulfil the requirements for coherent communication systems. In addition, the linewidth of commercially available fiber lasers is continuously decreasing (15 kHz has been announced recently by Ionas). Although it is not straightforward to replace the narrow linewidth and stable Nd:YAG lasers by DFB fiber lasers in the context of high bandwidth coherent communication systems, it might become feasible in the near future.

5 Fabry-Pérot Fiber Laser Sensor using FBGs

Innovation and inventiveness in optical fiber sensors have reached a first culminating point in the end of the 1970s with the development of multitude fiber sensor devices ([32], vol. IV). Since the mid 1980s, fiber amplifiers and fiber gratings with the help of general improvements in laser diode, detector, all-fiber components, have boosted even more innovation within the optical fiber sensors than initially expected. Fiber Bragg gratings (reflective gratings) are already used as remote elements for strain and temperature measurements by monitoring the reflected wavelength [71]. More recently, fiber Bragg gratings (FBGs) embodied in doped-fibers, as DBR and DFB fiber lasers, are investigated as active fiber sensor elements [72] [73].

We report in this chapter the application of a dual polarization Fabry-Pérot fiber laser as pressure and temperature sensor. The cavity is formed using a narrow bandwidth uniform FBG (0.08 nm) and a 2 nm bandwidth linearly chirped FBG. By measuring the polarization beat frequency, unidirectional pressure applied to the fiber can be measured. On the other hand, temperature applied on the narrow bandwidth FBG changes the wavelength of the laser emission. As the phase response of the chirped FBG is wavelength dependent, the change of the laser emission leads to a change of the cavity round-trip phase shift. The change of the round trip phase shift is determined, by measuring the longitudinal mode beat frequency (LMB). Therefore, this configuration enables simultaneous pressure and temperature with RF frequency readout, i.e. by measuring simultaneously the longitudinal and the polarization mode beat (PMB) frequencies.

5.1 Polarimetric pressure measurement with a short Fabry-Pérot fiber laser

We propose in this section a polarimetric Nd^{3+}-doped fiber laser sensor which measures the transverse force applied to the fiber. The force generates a change of the birefringence, revealed by the change of the beat frequency between the two orthogonal polarized laser modes (see 4.2.2.1). Polarimetric sensors using fiber lasers with dielectric mirrors and DFB fiber lasers have been reported in the literature [49] [74].

For our experiment we used the same fiber laser and the same setup as described in section 4.2.2. As a reminder, the laser is approximately 60 mm long and consists of a 12 mm long highly doped neodymium-fiber (Nd-160491) which is fusion spliced to two identical and uniform fiber Bragg gratings. As shown in Fig. 5.1, 20 mm of the uncoated part of the fiber (central part) was inserted between two parallel plates. The top-plate can be loaded with different weights from 1 g to several kg to generate a uniform transversal pressure along the fiber. This pressure is applied essentially on the uncoated doped-fiber and on the splicing points. The gratings were not squeezed, and their temperatures were maintained around 21 °C by the Peltier elements.

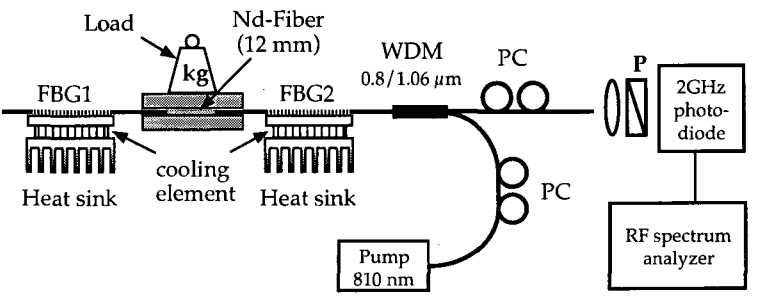

Fig. 5.1 Experimental setup of the polarimetric fiber laser sensor. 20 mm of the uncoated fiber section is squeezed between two plates.

When an optical fiber is squeezed between two parallel plates, the stress distribution adds linear birefringence to the core of the fiber. The light that propagates in a stressed fiber section can be separated into two linear eigen-polarizations orientated parallel and perpendicular to the direction of the force. For a distributed force F/l along the stressed fiber section, the induced birefringence is given by [75]

$$\Delta\beta = \frac{8Ck}{\pi D}\frac{\Delta F}{l}, \tag{5.1}$$

where, C is the stress-optic coefficient (C = 3.7 10^{-12} m^2/N for silica), k is wave-number, D is fiber diameter a is the core diameter.

In order to operate the fiber laser as a sensor, we measured the polarization mode beat (PMB) frequency as a function of the lateral force applied to the uncoated fiber section. As presented in 4.22, the change of the PMB frequencies can be measured with a RF spectrum analyzer. Without external perturbation on the fiber laser, we observed the first PMB frequency at 53 MHz. In order to start with a PMB frequency near zero, we compensate this inherent birefringence with bias weights. Thus we did load the fiber laser by several weights from 1 g to 400 g. As shown in Fig. 5.2, the PMB frequency, starting from 12.1 MHz, grows linearly with the applied weights.

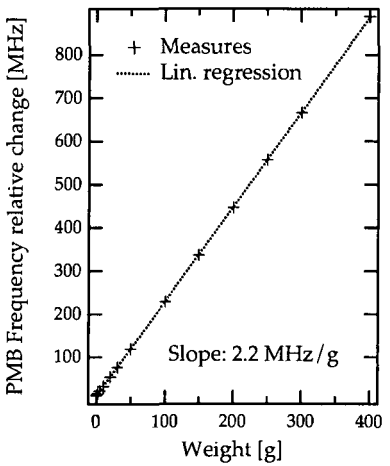

Fig. 5.2 PMB frequency versus applied weight. The sensitivity is 2.2 MHz/g. The resolution is better than 1g

The measurement was made with a resolution of 1 MHz on the RF spectrum analyzer, and 1 g applied as lateral pressure on the fiber laser was readily resolved. By a linear regression we found a sensitivity of 2.21 MHz/g. the accumulated phase difference between the two polarization modes for a round trip pass through the resonator is

$$\Delta\varphi = 2lk\Delta n = 2l\Delta\beta = \frac{32Cl}{\lambda D}\frac{\Delta F}{l} = \frac{32gC}{\lambda D}\Delta m. \tag{5.2}$$

where l is the squeezed fiber length, m is the mass of the load and g is the gravitation constant. The theoretical sensitivity of the polarization beat frequency with the mass m, is derived from Eqs. (5.1) and (4.32). we have

$$S_{\nu_{pol}} = (FSR)\frac{1}{2\pi}\left(\frac{\Delta\varphi}{\Delta m}\right) = (FSR)\frac{16gC}{\pi\lambda D}. \tag{5.3}$$

where l is the fiber section on which the pressure is applied, and g = 9.81 m/s^2 is the gravitation constant. Using D = 125 μm, λ = 1.06 μm, and C = 3.7 10^{-12} m^2/N, we calculated a sensitivity of 2.53 MHz/g. The measured value of 2.21 MHz/g in Fig. 5.2 is in good agreement with the theoretical one. The 2.21 MHz change of the beat frequency induced by a mass change of 1 g, represents a phase change in the laser of approximately 8.2 mrad.

5.2 Fabry-Pérot fiber laser sensor using a chirped FBG

One of the more recent advances in optical fiber sensing has been to use FBGs as passive transducer elements, interrogated by a broadband light source or tunable external-cavity laser. Another approach is to incorporate the FBGs into an active cavity as frequency-selecting element [76]. When the laser oscillates, the center reflection is continuously tracked. Short Fabry-Pérot cavity generally oscillates with few modes yielding to better resolution. We propose here a sensing system, where one of the two FBGs constituting the laser cavity plays the role of the transducer element.

5.2.1 Sensor principle

The principle of the sensor is schematically presented in Fig. 5.3. The idea is to use a pair of a narrow and a broad bandwidth FBGs. We assume that the external perturbation is applied only to the narrow bandwidth FBG, resulting in a detuning between the reflectivity spectra of the two FBGs. As shown in Fig. 4.12, each FBG is characterized by a group delay which is wavelength dependent. The detuning forces the laser to oscillate at different frequencies essentially dictated by the group delay of the broadband FBG. The change of the group delay produces a change of the optical path length in the cavity, measured through the longitudinal mode beat frequencies.

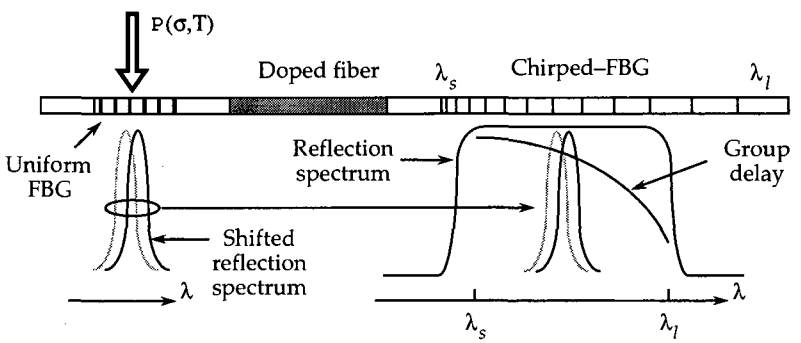

Fig. 5.3 Fiber laser cavity using a uniform, and a chirped FBG.

From the group delay defined in Eq. (4.13), we can introduce the total optical path length

$$L_{BG}(\lambda) = \frac{c}{n_{eff}} \tau_g(\lambda). \tag{5.4}$$

seen by the reflected light in the grating (forward and backward). As the round trip-path length of light in the FBG Fabry-Pérot cavity is a function of the phase dispersion of the gratings, we can determine the spectral mode spacing of the cavity. For a cavity containing two different fiber Bragg gratings, FBG1 and FBG2, we have

$$FSR_{BG}(\lambda) = \frac{c}{n_{eff}\left(2L_o + L_{BG1}(\lambda) + L_{BG2}(\lambda)\right)}. \tag{5.5}$$

L_{BG} can be considered as an additional path length in the cavity, which will depend on the spectral position of the resonance. We assume that the laser resonances are concentrated inside the reflection bandwidth of the narrow bandwidth FBG, near the maximum reflectivity. We propose to use a chirped FBG (CFBG) as the broad bandwidth FBG. CFBG are specially designed for chromatic dispersion cancellation in optical fiber communication. The dispersion introduced by the grating can vary from a few tens of ps/nm to more than 500 ps/nm, corresponding to a linear group delay of 1000 ps inside a reflection bandwidth of 2 nm.

There are two possibilities to couple the CFBG to the doped fiber of the laser cavity; from its shorter or longer wavelength side. In the first case the cavity will be shorter at shorter emission wavelengths and longer at longer emission wavelengths. Conversely, in the second case the cavity will be shorter at longer emission wavelengths and shorter at longer emission wavelengths.

5.2.2 Characterization of the chirped FGB

Before assembling the laser cavity, we characterized the reflectivity and the phase of the linearly chirped fiber Bragg grating (CFBG) provided by Highwave Optical Technology (France). The reflectivity of the CFBG is centered at 1549.3 nm and the reflection bandwidth is about 0.8 nm (FWHM). The length of the grating was approximately 12 cm, encapsulated in a temperature compensate-package of 20 cm length.

The phase response of the chirped fiber Bragg grating (CFBG was measured with a Michelson interferometer, shown in Fig. 5.4. An Ag-coated mirror and the CFBG constitute the reflectors of the interferometer. The dispersion of the metallic mirror and the optical fiber material is ignored compared with the dispersion introduced by the CFBG. The position of the metallic mirror is set arbitrary near half the CFBG length. The wavelength was scanned with a tunable external cavity laser diode (Photonetics). The tuning speed was about 10 ms/nm. For the detection, we used a 2 GHz InGaAs photodiode (Hewlett-Packard), and the detection was triggered on the tuning start signal.

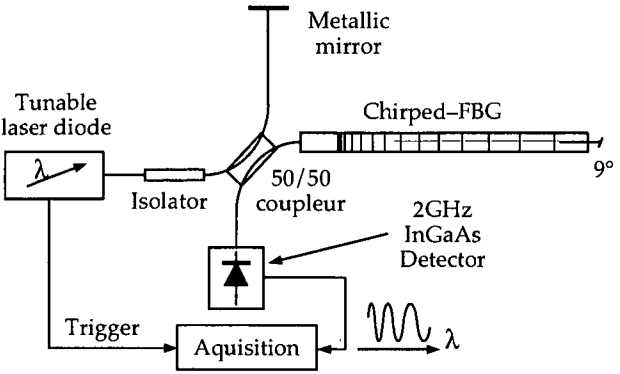

Fig 5.4 Phase response of a chirped FBG using a tunable laser diode source in a Michelson interferometer arrangement.

The response from the Michelson interferometer is shown in Fig. 5.5. The balance of the optical path length between the reference arm and the arm containing the CFBG is obtained for a wavelength value of about 1549.6 nm. We assumed that the scanning was linear in the time within wavelength range used for the measurements.

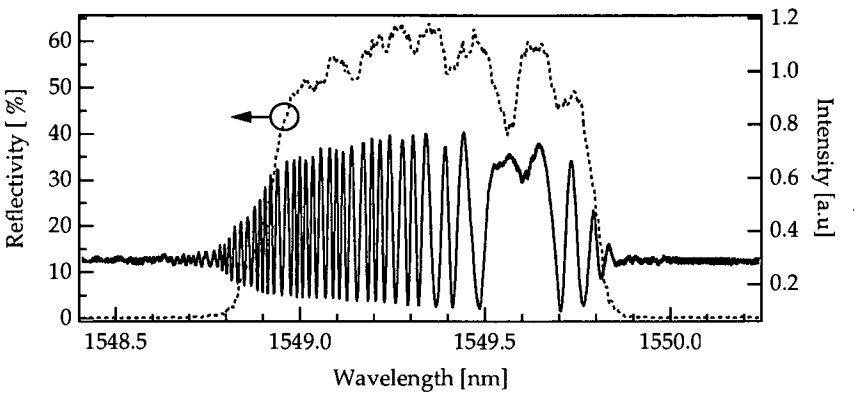

Fig. 5.5 Response of the Michelson interferometer as function scanned wavelength. The reflectivity was measured using the setup of Fig. 5.4 without the metallic mirror.

We report in Fig. 5.5 also the reflectivity of the CFBG, which was measured realized using the same setup of Fig. 5.4, but without the metallic mirror. The results show clearly the poor reflectivity of the CFBG (max. 64 %) and an important dip at 1549.6 nm, with only 39% reflection. This poor reflectivity generates important cavity losses, which must be compensated by the gain of the doped fiber.

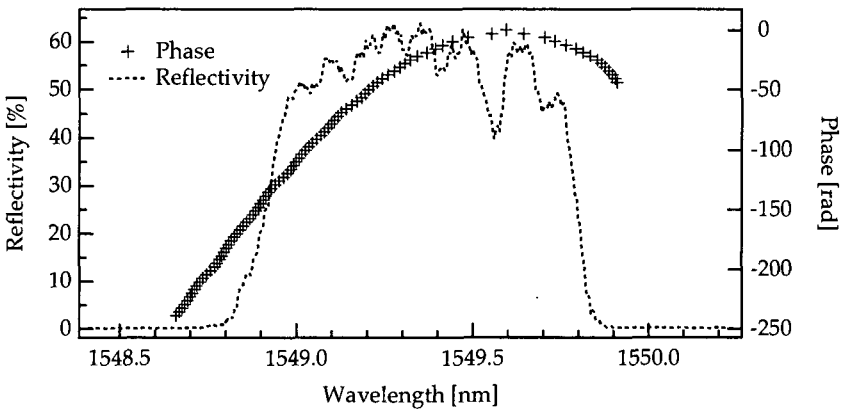

Fig. 5.6 Reconstructed phase versus wavelength.

From the interferometric response in Fig. 5.5, we can reconstruct the accumulated phase by counting the π phase changes, given by consecutive maxima and minima of the intensity of the interferogram. The zero-phase is taken at the wavelength for which the two arms of the interferometer are balanced. The result is shown as crosses in Fig. 5.6. The spectral reflectivity is added to visualize the position of the phase curve with respect to the reflectivity. 3rd degree polynomial function was fitted to the reconstructed phase (Fig. 5.7). From this fit, the group delay was calculated using Eq. (4.13). The result is shown in Fig. 5.7 as dashed line. It is in good agreement with the specification provided by the supplier (gray line).

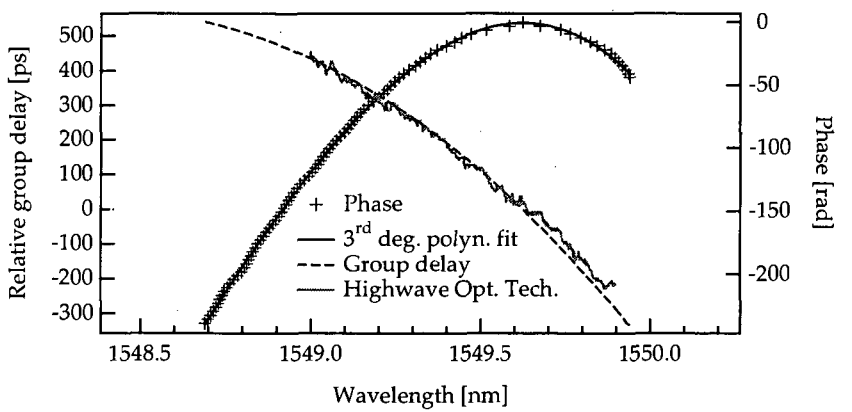

Fig. 5.7 Calculated group delay from the 3rd degree polynomial fit of the reconstructed phase. For comparison the group delay provided by the supplier (Highwave Optical Technology) is also shown.

5.2.3 Spectral variation of the narrow FBG versus temperature

To characterize the thermal dependence of the reflection spectrum of the narrow FBG, we changed the temperature of the narrow bandwidth grating using the Peltier element (Fig. 5.1). For increasing temperature the reflection spectrum of FBG_1 shifts toward longer wavelengths. We measured the shift of the wavelength at the maximum reflection for temperatures from 5°C to almost 60 °C. The results are presented in Fig. 5.8. Linear regression fits well the data and gives a sensitivity of the center wavelength versus temperature of 11.1 pm/°K. This thermal sensitivity will be used in the simulation to convert the wavelength dependence of the group delay to a temperature dependence. We report in Fig. 5.9 the measured reflection spectra of the CFBG and of the narrow bandwidth FBG for three different temperatures. We realized the measurement with 1 pm resolution tunable external-cavity laser.

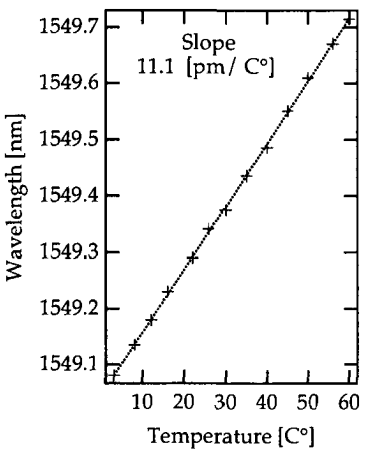

Fig 5.8 Center wavelength of FBG_1 (Fig. 5.1) versus applied temperature

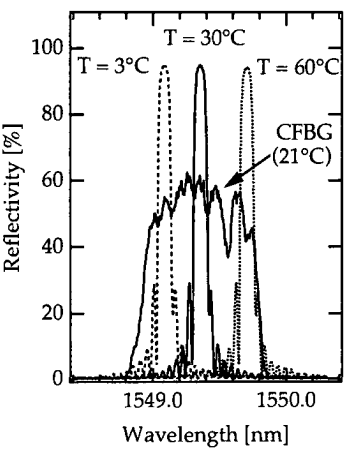

Fig. 5.9 Reflection spectra of the narrow FBG for different temperatures and the reflection spectrum of the CFBG

5.2.4 Simulation of the sensor properties

Knowing the group delay introduced by the CFBG as a function of the wavelength and using Eq. (5.4) and Eq. (5.5), we can calculate the corresponding longitudinal mode (LMB) frequency. The required active fiber length to compensate the cavity losses depends on the small signal gain provided by the doped fiber. This minimum length of the doped fiber fixes the minimum length of the cavity. The LMB frequencies have been calculated for different lengths L_0 (cavity length without gratings).

Since the laser emission is fixed by the spectral position of the narrow bandwidth grating and therefore by the applied temperature, we can convert the wavelength-dependence of the LMB frequency into a temperature-dependence. Figure 5.8 a) and 5.8 b) represent the different LMB frequencies versus temperature for shorter and longer wavelength side coupling of the CFBG to the doped fiber, respectively. These curves show clearly that the measurement sensibility is higher for short cavities. Therefore the cavity length is an important parameter, which must be optimized as a function of the cavity losses and the gain of the doped fiber.

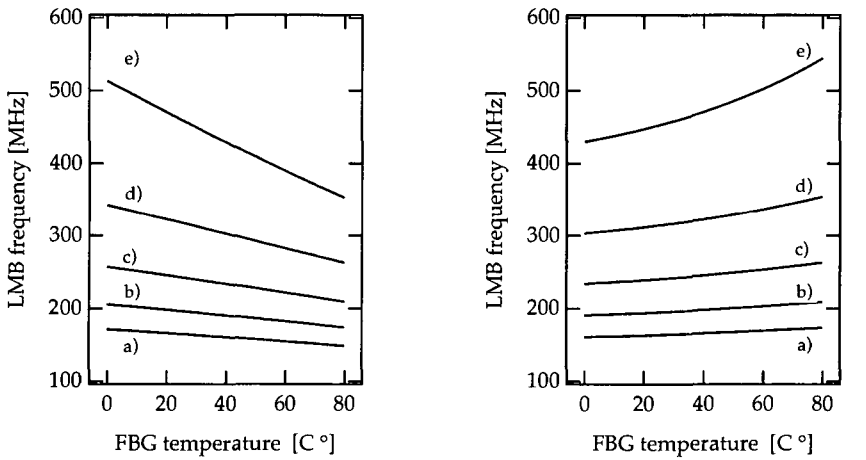

Fig. 5.10 Fiber laser LMB frequency for different cavity lengths L_0 : a) 60 cm, b) 50 cm, c) 40 cm, d) 30 cm, and e) 20 cm and for two CFBG-assembling configurations: A) is for the shorter and B) for the longer wavelength side of the CFBG towards the laser cavity

As curves of Fig. 5.10 for the CFBG-assembling configuration (A), seams to be more linear than for the configuration (B), we spliced the doped fiber to the shorter wavelength side of the CFBG.

5.2.5 Required fiber laser gain

As shown in Fig. 5.9, the CFBG has a poor reflectivity, with a maximum of 64 % around 1549.2 nm and quite large ripples. There is also a hole in the spectrum with a minimum reflection of 39% around 1549.5 nm. We assume that the losses are essentially due to the mirror reflections. According to the assumption, we get form Eq. (4.26) for the total loss of the cavity $\delta = 1-(R_{NFBG}R_{CFBG})$. The laser is assumed to operate always at the maximum reflectivity of the narrow bandwidth FBG (R_{NFBG} = 95%). For the worst case, minimum

reflectivity of the CFBG (R_{CFBG} = 39%), we have almost 63% of reflection losses. If we add losses caused by the splices (doped fiber connection to the FBGs) of 6% we get a total loss of approximately 66% (-4.7 dB).

The laser was built with an Er^{3+}-doped fiber using the $^4I_{13/2}$ -> $^4I_{15/2}$ transition at 1550 nm. Commercially available Er^{3+}-doped fibers co-doped with Yb^{3+}, like fiber types EY 304 and EY 105 (Tab. 2.2), are useful when strong pump absorption at 980 nm is needed. These fibers have gains at 1550 nm (bleached fiber) of 7 dB/m and 16 dB/m respectively and an absorption at pump wavelength (980 nm) of 540 dB/m and ~900 dB/m, respectively. This means that the 100 mW available pump power can only invert a few centimeters of the doped fiber. If we assume that 10 cm and 5 cm are completely inverted, we get only 0.7 dB to 0.8 dB of gain, which is far from the gain required to compensate the losses of – 4.7 dB in our cavity. Such fibers would be ideal for short cavity laser with very low losses. Finally the solution was to use highly doped Er^{3+} fibers without Yb^{3+} co-dopant. High Erbium concentration allow sufficient gain and sufficient long pump interaction in the fiber. The fiber type Er123 (Tab. 2.2) fulfilled the minimum gain requirement for our fiber laser. This fiber has a gain of 21 dB/m at 1550 nm with 27dB/m pump absorption at 980 nm. We used 30 cm long piece of this fiber to build the fiber laser cavity. The available gain is thus 7 dB and almost 9 dB of the pump light are absorbed.

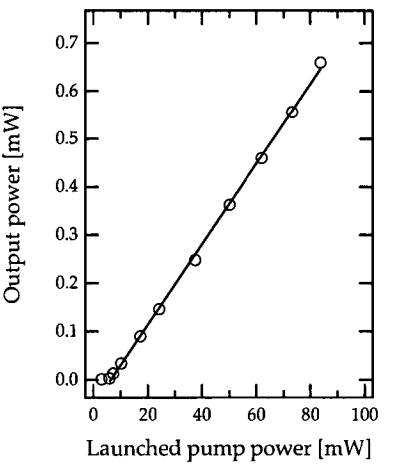

Fig. 5.11 Output power of the fiber sensor versus launched pump power

The corresponding fiber laser with the two FBGs started oscillating at 9 mW launched pump power, as see in Fig. 5.11. The differential pump conversion is about 0.9 %. A maximum output power of 0.7 mW was reached for 90 mW launched pump power.

The fiber laser resonances were analyzed with a scanning Fabry-Pérot (FSR = 25 GHZ). The results are presented in Fig. 5.12. The scanning revealed four pairs of axial modes, with a frequency spacing of 186.1 MHz, corresponding to a temperature of the narrow bandwidth FBG of 23.5°C. According to Eq. (4.30) the cavity length is to be 55 cm (30 cm of doped fiber). Each pair of resonances consisted of two polarization modes imposed by the intrinsic birefringence of the cavity. These polarization modes are spaced by 50.2 MHz, which can be reduced to almost 20 MHz by compensating

partially the birefringence of the cavity by bias weights. Since the intrinsic birefringent of the laser components have arbitrary orientation, it was not possible to compensate completely this residual birefringence.

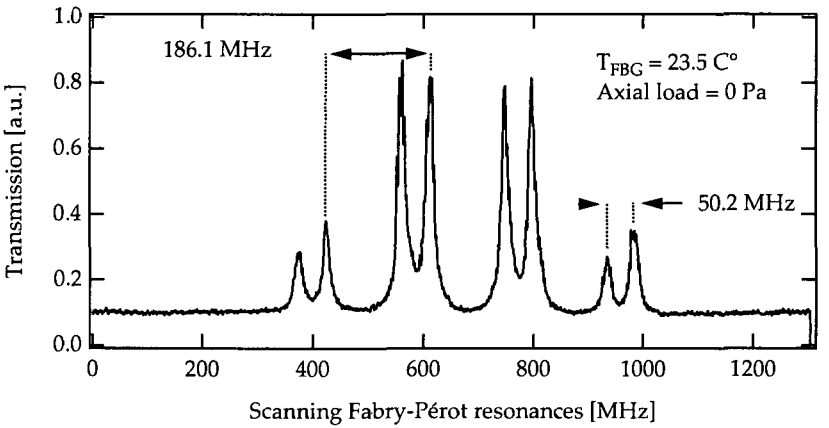

Fig. 5.12 Laser emission analyzed with a scanning Fabry-Pérot (FSR = 25 GHZ). There are four pairs of axial modes with a spacing of 186.1 MHz, corresponding to a temperature on the narrow bandwidth FBG of 23.5°C. Each pair of polarization modes is spaced by 50.2 MHz.

5.2.6 Temperature measurement by cavity round-trip phase shifting

According to the simulations in 5.2.4, we tried to reproduce the change of the optical phase shift introduced by the detuning of the reflection spectra of the two fiber gratings. The experimental setup is shown in Fig. 5.13.

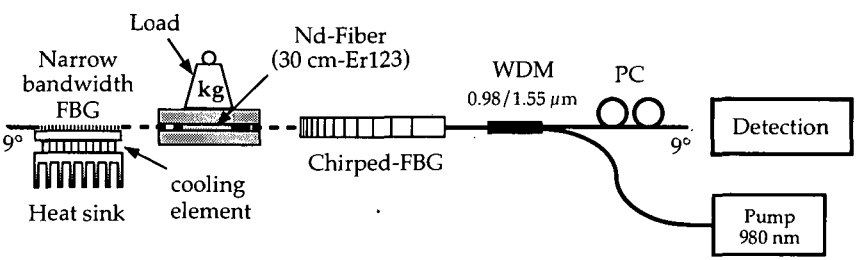

Fig. 5.13 Experimental setup with a 30 cm long Er^{3+}-doped fiber (Er123) spliced to a narrow bandwidth FBG and to a chirped FBG. The temperature of the narrow bandwidth FBG is controlled by a Peltier-element.

The temperature of the narrow bandwidth FBG is controlled by a Peltier-element from 5°C to almost 70 °C. A small fiber section of the cavity (20 mm) can be squeezed between two parallel plates. This mount will be used in the following to measure simultaneously lateral pressure and the temperature.

The temperature changes of the narrow bandwidth FBG produce changes of the emission wavelengths due to the shift of its reflection spectrum. The reflection of the chirped FBG is large enough to always match the reflection spectrum of the narrow bandwidth FBG in the range of the temperature measurement (5°C to 60°C). As the phase dispersion of the chirped FBG is wavelength dependent, the optical path length in the cavity changes with the applied temperature on the narrow bandwidth. As a consequence, the longitudinal mode beat (LMB) frequency changes with temperature.

We report in Fig. 5.14 the LMB frequency as a function of the temperature applied to the narrow bandwidth FBG. The thermal dependence of Bragg wavelength was measured in 5.2.3 as 11.1 pm/K°. The simulated LMB frequency shift with temperature, calculated with Eq. (4.30), fits quite well the measured values.

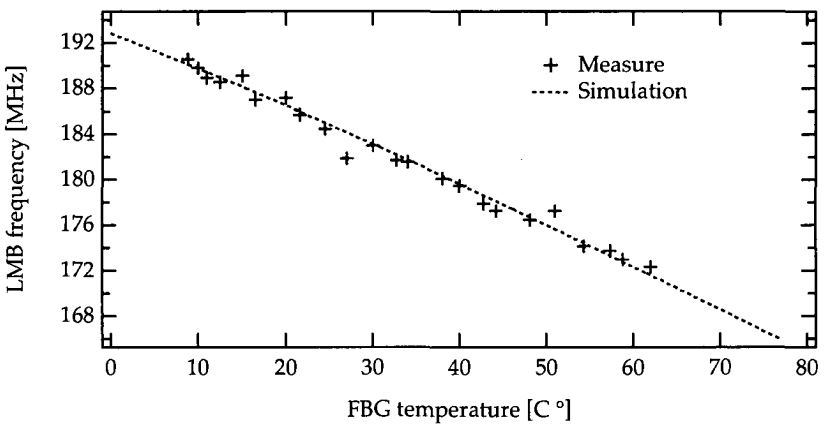

Fig. 5.14 LMB frequency shift as a function of the temperature applied on the narrow bandwidth FBG. The CFBG is maintained at room temperature (22°C)

The LMB frequency variations were measured with a sensitivity of about 348 kHz/°C. The group delay variations are specified to be 20 ps (maximum peak-to-peak ripples) by the supplier. In terms of LMB frequency, this corresponds to variations of about 380 kHz, which limits therefore the accuracy to approximately 1 °C. To get 0.1 °C accuracy, the group delay ripples should be reduced at least at 2 ps (peak-to-peak).

5.2.7 Simultaneous pressure and temperature measurements

DFB fiber laser as polarimetric sensors for strain measurement, supplemented by optical spectrum analyzer for temperature measurements, has been already investigated in [73]. We demonstrate here the feasibility of a simultaneous measurement of the pressure and temperature with direct RF readout for the two measurements

First we study the influence of the lateral pressure and the temperature variations on the longitudinal and polarization mode beat frequencies, respectively. Figure 5.15 displays the polarization beat frequency variations for three different loads applied to the fiber in the cavity (Fig. 5.13). In this example, the temperature of the narrow bandwidth FBG is maintained constant at T = 55°C. This figure shows clearly that the lateral pressure does not influence the longitudinal mode beat frequency, which remains at 174 MHz for the different tested loads.

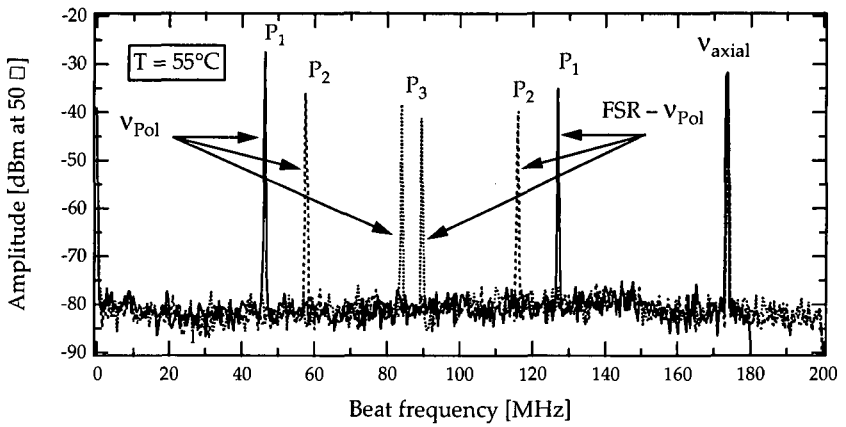

Fig. 5.15 Beat frequencies measured for three different loads (P_1, P_2, P_3) applied to the fiber in the cavity. The temperature on the narrow bandwidth is maintained constant at 55 °C. The longitudinal mode beat frequency (ν_{axial}) remains constant at 174 MHz

In the second experiment, we have changed the temperature of the narrow bandwidth FBG, whereas the load on the fiber cavity was maintained constant. The result is reported in Fig. 5.16 for two different temperatures (10° and 55°C). As expected form Eq. (4. 32), the polarization mode beat (PMB) frequency is proportional to the change of the free spectral range (FSR), which can be expressed in terms of a LMB frequency change. For temperatures varying from 10°C to 55°C, the sensitivity is found to be 348 KHz/°C

Shortening the length of the cavity would have the advantage to improve the sensitivity of the laser sensor to pressure and thermal variations. The simulation displayed in Fig. 5.10 A) shows a sensitivity of about 1.75 MHz/°C for a cavity length of L_0 = 20 cm.

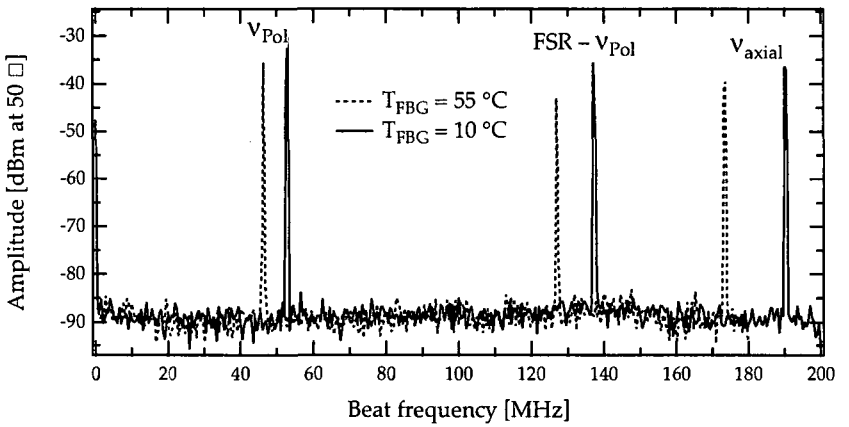

Fig. 5.16 Measured LMB and PMB frequencies for two different temperatures (10 °C and 55 °C) of the narrow bandwidth FBG. The load was constant.

Shortening the cavity length to 5 cm might even become feasible for mirror losses of less than 16 % (Typically for R_1 =95% and R_2 = 90%). Therefore at this cavity length, the fiber laser would become a very sensitive temperature and pressure sensor.

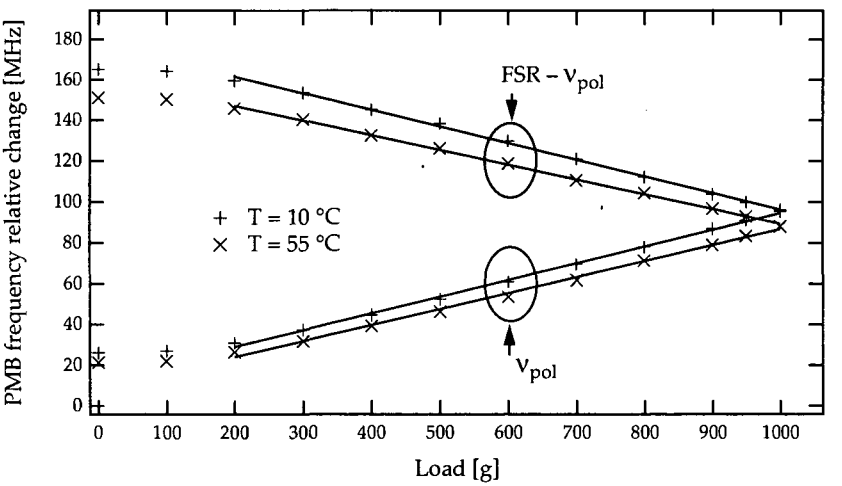

Fig. 5.17 Beat frequencies of two consecutive PMB frequencies (ν_{pol} and FSR – ν_{pol}) versus applied load.

Finally, we measured the PMB frequency for increasing loads to the fiber and for different temperatures. We have reported in Fig. 5.17 two consecutive PMB frequencies, represented by ν_{pol} and FSR – ν_{pol}. The non-linearity observed for loads < 200 g is due to the soft acrylic coating of the fiber, which had not been removed in this experiment. As seen from Fig. 5.17, the range within which the PMB frequency is determined without ambiguity is limited to the half value of the free spectral range of the cavity. For dual-polarization single-frequency lasers, this limit does not exist, since there is no axial mode beat. In this case however, the change of the cavity length as a function of the temperature can not be monitored with a RF spectrum analyzer. Therefore, combined fiber laser pressure and temperature sensor wit RF read out requires at least two axial modes with two polarizations.

In the ideal short cavity sensor with no residual birefringence, the pressure can be readily deduced knowing the value of the LMB frequency. This means also that the LMB frequency of the laser sensor must be calibrated at a given temperature. Without calibration, the sensor will only measure relative changes of temperature.

6 Summary and Conclusion

The recent technical progresses in optical amplifiers and lasers based on rare-earth doped fibers, supplemented by fiber based components, have stimulated a new look in active fiber design. As the demand of the information capacity is rapidly growing, most the recent developments in optical fiber devices (sources, amplifiers) are devoted to the field of optical communication operating between 1.3 and 1.55 μm. Sensing with active fiber devices is another domain, which regains interest. Fiber Bragg gratings (FBGs) are without doubt important fiber-optic devices, which boosts the sensor-market. Combined with doped fibers, FBGs allow fiber laser designs, which can be used as active sensor devices.

The motivation for this work was to provide some basic understanding of the spectral properties of light sources and lasers using rare earth doped fibers. Interesting approaches have been found for the realization of broad and narrow bandwidth light sources. Finally, combined pressure and temperature sensor with direct RF readout using a fiber Fabry-Pérot laser with a uniform and a linearly chirped Bragg grating has been demonstrated.

Broadband light sources are useful to interrogate distributed sensor systems or for low coherence interferometry. Combining different type of Nd^{3+}-doped, Er^{3+}-doped and Yb^{3+}-doped to get fiber sources have been investigated. With an appropriate combination we have demonstrated a 70 nm bandwidth (FWHM) fiber source emitting around 1.06 μm a single transverse mode with a power of about 100 μW. Spectral filtering before high power amplification rather than at the output, is another interesting approach to achieve broadband emission with high power. First, a long Yb^{3+}-doped fiber was pumped from both fiber ends. Since the pump power of the two pump sources is rapidly absorbed, a part of the filter length, located approximately in the middle, remains unpumped and acts as a spectral filter. Second, a metal-coated long period fiber grating was used as spectral filter between two Er^{3+}-doped fibers. With the first approach, we obtained about 90 nm bandwidth with a single transverse mode

output power up to 120 μW. With the second approach, using the loss filter, we reached an output power of 0.85 mW with a spectral width of 50 nm.

There are many applications that require single frequency laser operation. As the field of fiber laser is too large to encompass all possible design consideration in a single text, only the linear Fabry-Pérot cavity and its application has been considered in this thesis. Short cavity Fabry-Pérot lasers can be easily fabricated by written Bragg mirrors directly into the fiber. However, narrow linewidth operation is difficult to obtain even for short cavities. A Fabry-Pérot cavity was built, using a 12 mm long highly doped neodymium-fiber and two narrow bandwidth (0.1 nm) fiber Bragg gratings. By tuning one of the two gratings single longitudinal mode laser emission was obtained. However due to the birefringence of the doped fiber, the longitudinal resonance was split into two linear eigen-polarization modes. Pure single-frequency (single-polarization) laser operation was obtained near threshold by controlling the pump power polarization, which favors one of the two polarization modes. However, single frequency fiber lasers, with distributed Bragg reflectors, suffer from longitudinal mode hopping. They are therefore not recommended as wavelength tunable lasers.

In view to replace single frequency Nd:YAG lasers as master lasers for coherent intersatellite communication, we investigate the tunability and linewidth of available Nd^{3+}-doped fibers with distributed feedback (DFB) Bragg gratings. For this purpose, the fiber lasers were locked by an optical feedback loop to a narrow bandwidth (4.5 kHz) Nd:YAG laser. Beat frequency measurements revealed that amplitude noise of the pump laser may broaden the DFB laser emission. Finally, we got a linewidth at -3dB of 46 kHz (FWHM). Although it is not yet good enough to replace the Nd:YAG, it might become feasible in the near future. Indeed, the linewidth of commercially available DFB fiber lasers is continuously decreasing (15 kHz has been announced recently by Ionas).

We have reported in the last chapter investigation to use short Fabry-Pérot fiber lasers as polarimetric pressure sensors. Any mechanical perturbation of the fiber in the cavity introduces birefringence. This birefringence manifests itself as a change of the beat frequency between the polarization modes of the laser. In the first experiment, we measured the lateral pressure with a sensitivity of 2,2 MHz/g, a resolution of 1g and a dynamic range of 1:400 limited by the free spectral range of the laser cavity.

Inspired by the observation made during this first experiment, we proposed a new concept for a combined temperature and pressure sensor with a direct RF read out. The fiber laser cavity consists of a standard narrow and chirped broad bandwidth fiber Bragg gratings (FBGs). Polarization beat frequency monitors the lateral pressure applied to the fiber in the cavity. Temperature changes of the narrower bandwidth FBG

produce a change of the oscillation wavelength, which is transformed into a change of the free spectral range of the laser cavity by the phase dispersion of the chirped FBG. As a consequence the longitudinal mode beat (LMB) frequency can be used to monitor the temperature changes of the narrower bandwidth FBG. The feasibility of this concept has been verified with a Er^{3+}-doped fiber of 55 cm cavity length operating at 1.5 μm. The temperature was measured with a sensitivity of about 350 kHz/°C. The group delay variations of the chirped FBG are specified by the supplier to be 20 ps (maximum peak-to-peak ripples). In terms of LMB frequency, this corresponds to variations of about 380 kHz by a variation of about 1 °C on the narrow FBG. Thus, the quality of the chirped FBG limits the accuracy of the temperature sensor to about 1 °C. The group delay ripples should be reduced at least at 1 ps (peak-to-peak) to enable measurement with 0.1 °C resolution.

Shortening the cavity length would provides two major improvements:

- Increased sensitivity for the pressure and temperature measurement
- Reduced number of axial modes in the cavity, leading to a more accurate read out of the beat frequencies.

In addition, the group delay of the chirped FBG can be designed in order to compensate exactly the non-linearity response of the LMB frequency shift and the same sensor configuration can be used for strain measurement when an adequate transducer is mounted on the narrow bandwidth FBG. Since the chirped FBG is used as the reference of the system, a good mechanical and thermal stability of the chirped FBG is required. Naturally, there are still a large number of points that are not treated in this thesis. They include the thermal birefringence compensation techniques, laser mode stability, and the role of the FBG dispersion on the linewidth of the beat frequencies, among other subjects. The rapid innovations and improvements in the field of optical fiber components will certainly render this design concept applicable in future development woks in the optical fiber laser sensor domain.

7 Acknowledgements

First of all, I would like to express my sincere gratitude to Prof. René Dändliker, director of my thesis. His commitment to this work and his constant advice and encouragement have been of invaluable help to me.

I am grateful to Prof. Hans Peter Hertzig, Prof. Willy Lüthy and Prof. René-Paul Salathé for their critical review of this work as members of the jury.

My especial thanks go to Etienne Rochat who was intimately involved with the realization of this work. I have appreciated his tough criticism and helpful suggestions.

I am grateful to Yves Salvadé for providing me valuable suggestion, notably for the dispersion characterization of fiber Bragg gratings. I also thank Hubert Brändle who gave me the opportunity to use the facilities of the ABB research center at Baden-Dättwil, otherwise a part of this work could not have been realized.

Many colleagues have also contributed in their different ways to the realization of this work and I thank them all. I would like to thank more particularly Marcel Groccia, not only for his technical support, but also for the friendly discussions we often had during these four years. Special thanks to Caspar Bijleveld and Omar Manzardo for their helps and supports during the redaction of this thesis. More generally, I would like to thank all my colleagues and the secretaries for their contribution to the pleasant atmosphere in the institute.

Finally, I am especially indebted to my parent for their permanent support during my studies. My thanks and affection go to Wieslawa, my wife, for her encouragement and for her admirable patience during this work.

K. S. Haroud

8 References

[1] T. H. Maiman, "Stimulated Optical Radiation in Ruby," *Nature*, vol. 187, pp. 493 – 494, 1960.

[2] E. Snitzer, "Optical Maser Action of Nd^{3+} in a Barium Crown Glass," *Phys. Rev. Letters*, no. 7, pp. 444, 1661.

[3] C. J. Koester, and E. Snitzer, "Amplification in a Fiber Laser," *Appl. Optics*, no. 3, pp. 1182, 1964.

[4] MacChesney, *et al.*, "Preparation of low optical fibers using simultaneous vapor phase deposition and fusion," *Int. Congr. Glass (Kyoto, Japan) 10th Tech. Diag.*, no. 6, pp. 40 – 44, 1974.

[5] R. J. Mears, *et al.*, "Low–noise Erbium–doped fiber amplifier operating at 1.54 μm," *Electron. Lett.*, vol. 22, no. 3, pp. 159 – 162, 1987.

[6] R. Szweda, "Fiber Bragg gratings win ground in telecommunications and sensors," *Opto-Laser Europe, Jully*, pp. 43 – 47, 2000.

[7] P. W. France, "Optical fiber lasers and amplifiers," *Blackie, London*, 1991.

[8] E. Desurvire, "Erbium–doped fiber amplifiers Principles and Applications," *John Wiley &Sons, New York*, 1994.

[9] M. J. F. Digonnet, "Rare earth doped fiber lasers and amplifiers," *Marcel Dekker, Inc. New york – Basel – Hon kong*, 1993.

[10] M. J. F. Digonnet, and C. J. Gaeta, "Theoretical analysis of optical fiber laser amplifiers and oscillators," *Opt. Lett.*, vol. 24, no. 3, pp. 333 – 342, 1985.

[11] M. J. F. Digonnet, "Theory of Superfluorescent Fiber Lasers," *J. Lightwave Technol.*, vol. LT–4, no. 11, pp. 1631 – 1639, 1986.

[12] EDFAdisign, "www.optiwave.com/edfa.html," *by Optiwave corporation*, 1997.

[13] S. Zemon, *et al.*, "Characterization of Er^{3+}–doped glasses by fluorescence line narrowing," *J. Appl. Phys.*, vol. 69, no. 10, pp. 6799 – 6811, 1991.

[14] P. R. Morel, A. Woodtli, and R. Dändliker, "Characterization of the fluorescent lifetime of doped fiber by using the frequency transfer function," *J. Lightwave Technol.*, vol. 14, pp. 739–742, 1996.

[15] B. J. Ainslie, S. P. Craig, and S. T. Davey, "The absorption and fluorescence spectra of rare earth ions in silica–glass monomode fiber," *J. Lightwave Technol.*, vol. 6, no. 2, pp. 287–293, 1988.

[16] A. W. Snyder, and J. D. Love, "Optical Waveguide Theory," *Chapman and Hall, London*, 1983.

[17] G. S. Ofelt, "Intensities of crystal spectra of rare earth ions," *J. Chem. Phys.*, vol. 37, no. 3, pp. 511, 1962.

[18] W. L. Barnes, P. R. Morkel, and J. E. Townsend, "Detailed characterization of Nd^{3+}–doped SiO_2–GeO_2 glass fiber lasers," *Opt. Commun.*, vol. 82, pp. 282 – 288, 1991.

[19] A. Yariv, "Optical Electronics in Modern Communication," *Oxford University Press, New York*, 1997.

[20] A. Yariv, "Quantum Electronics," *Third edition, John Wiley & Sons*, 1988.

[21] A. E. Siegman, "Lasers," *University Science Books, Mill Valley, California*, 1986.

[22] W. H. Press, *et al.*, "Numerical Recipes, The Art of Scientific Computing," *Cambridge University Press, New York*, 1986.

[23] M. J. F. Morkel, M. C. Farries, and S. B. Poole, "Spectral variation of excited state absorption in neodymium doped fiber lasers," *Opt. Commun.*, vol. 67, pp. 349 – 352, 1988.

[24] E. Rochat, A. Woodtli, and R. Dändliker, "Excited–state absorption and gain measurement at 1.3 μm in Nd^{3+}," *J. Lightwave Technol.*, vol. 15, pp. 1573 – 1577, 1997.

[25] C. Ghisler, *et al.*, "Up-conversion cascade laser at 1.7 nm with simultaneous 2.7 nm lasing in Erbium ZBLAN fiber," *Electron. Lett.*, vol. 31, pp. 373 – 376, 1995.

[26] H. M. Pask, *et al.*, "Ytterbium–Doped Silica Fiber Lasers: Versatile Sources for the 1–1.2 μm Region," *IEEE J. Select. in Topics Quantum Electron.*, vol. 1, no. 1, pp. 2–13, 1995.

[27] W. L. Barnes, *et al.*, "Er^{3+}-Yb^{3+}- and Er^{3+}-doped fiber lasers," *J. Lightwave Technol.*, vol. 7, pp. 1461 –1465, 1989.

[28] M. E. Fermann, *et al.*, "Efficient operation of an Yb–sensitized Er fiber laser at 1.56 μm," *Electron. Lett.*, vol. 24, pp. 1135 –1136, 1988.

[29] D. C. Hanna, *et al.*, "Efficient and tunable operation of Tm–doped fiber laser," *Opt. Commun.*, vol. 75, pp. 283 –286, 1990.

[30] W. L. Barnes, and J. E. Townsend, "Highly tunable and efficient diode pumped operation of Tm^{3+} doped fiber lasers," *Electron. Lett.*, vol. 26, pp. 746 – 747, 1990.

[31] C. C. Culster, S. A. Newton, and H. J. Shaw, "Limitation of rotation sensing by scattering," *Opt. Lett.*, vol. 5, no. 11, pp. 488 – 490, 1980.

[32] J. Dakin, and B. Culshaw, "Optical Fiber Sensors: Application, Analysis, and Future Trends," *Artech House, Boston – London*, vol. IV, 1997.

[33] P. R. Morkel, "Wavelength stability of Nd^{3+}doped fiber fluorescent source," *Electron. Lett.*, vol. 26, pp. 873 – 875, 1990.

[34] K. Haroud, E. Rochat, and R. Dändliker, "A broad–band superfluorescent fiber laser using single–mode doped silica fiber combinations," *IEEE J. Quantum Electron.*, vol. 36, no. 2, pp. 151 – 154, 2000.

[35] A. M. Vengsakar, "Long-period fiber grating as band-rejection filters," *J. Lightwave Technol.*, vol. 14, pp. 58 – 65, 1996.

[36] H. S. Kim, *et al.*, "All-fiber acousto-optic tunable notch filter with electronically controllable spectral profile," *Opt. Lett.*, vol. 22, no. 19, pp. 1476 – 1478, 1997.

[37] R. Paschotta, *et al.*, "Efficient Superfluorescent Light Sources with Broad Bandwidth," *IEEE J. Select. in Topics Quantum Electron.*, vol. 3, no. 4, pp. 1097 – 1999, 1997.

[38] K. Inoue, T. kominato, and H. Toba, "Tunable Gain Equalization using Mach-Zehnder Optical Filter Amplifiers," *IEEE Photon. Technol. Lett.*, vol. 3, no. 8, pp. 718 – 720, 1991.

[39] N. Takano, *et al.*, "Silica-based Integrated Optic Mach-Zehnder Multi/Demultiplexer Family with Channel Spacing of 0.01-250 nm," *IEEE Journal on Selected Area of Communication*, vol. 8, no. 6, pp. 1120 – 1127, 1990.

[40] C. W. Hodgoson, and A. M. Vengsarkar, "Spectrally shaped high-power Amplified Spontaneous Emission sources incorporating long period Gratings," *Optical Fiber Communication conference, OFC'96,* 1996.

[41] A. M. Vengsarkar, *et al.*, "Long-Period Fiber Grating-based Gain Equalizer," *Opt. Lett.*, vol. 21, pp. 336 – 338, 1996.

[42] S. G. Grubb, *et al.*, "1.3 μm cascaded Raman Amplifier in Germano-silicate Fibers," *Proc. Optic. Amplifier Meet., CO, Aug.* 3 – 5, *Post-deadline Paper PD3,* 1994.

[43] D. Costantini, "Novel optical Fiber Components based on Thin-Film Coating and Intra-core Fiber Grating," *Thesis, Federal Institute of Technology of Lausanne EPFL, Switzerland,* 2000.

[44] A. Yu, and M. J. O'Mahony, "Analysis of dual-stage erbium-doped fiber amplifiers with passive equalization filters," *IEEE Proc. Optoelectron.*, vol. 146, no. 3, pp. 153 – 158, 1999.

[45] L. A. Wang, and C. D. Chen, "Comparison of efficiency and output power of optimal Er-doped superfluorescent fiber sources in different configurations," *Electron. Lett.*, vol. 33, no. 8, pp. 703 – 704, 1997.

[46] F. A. Flood, and O. K. Tonguz, "Comparison of Gain Equalization Strategies for Erbium-doped Fiber Amplifier Chains," *Journal of Optical Communications,* vol. 17, no. 3, pp. 89 – 94, 1996.

[47] Y. Cheng, *et al.*, "Stable single -frequency traveling-wave fiber loop laser with integral saturable- absorber-based tracking narrow-band filter," *Opt. Lett.*, vol. 20, no. 8, pp. 875 – 877, 1995.

[48] G. A. Ball, and W. W. Morey, "Continuously tunable single-mode erbium fiber laser," *Optics Letter,* vol. 17, no. 6, pp. 420 – 422, 1992.

[49] H. K. Kim, and S. K. Kim, "Polarimetric fiber laser sensors," *Opt. Lett.*, vol. 18, no. 4, pp. 317 – 319, 1993.

[50] T. Erdogan, "Fiber Grating Spectra," *J. Lightwave Technol.*, vol. 15, no. 8, pp. 1277 – 1294, 1997.

[51] K. O. Hill, *et al.*, "Photoensitivity in Optical Fibers," *Annu. Rev. Master. Sci.*, pp. 125 – 157, 1993.

[52] K. O. Hill, and G. Meltz, "Fiber Bragg Grating Technology Fundamental and Overview," *J. Lightwave Technol.*, vol. 15, no. 8, pp. 1263 – 1276, 1997.

[53] R. Dändliker, "Coupled Waves: A Powerful Concept in Modern Optics," *SPIE*, vol. 3190, pp. 279 – 288, 1997.

[54] H. Kogelnik, "Coupled Wave Theory for Thick Hologram Gratings," *Bell System Tech. J.*, vol. 48, pp. 2909 – 2947, 1969.

[55] T. Imai, and T. Mastumoto, "Polarization Fluctuation in a Single-Mode Optical Fiber," *J. Lightwave Technol.*, vol. 6, no. 9, pp. 1366 – 1375, 1988.

[56] D. Maruse, "Coupled-mode theory for anisotropic optical wave-guides," *Bell Syst. Tech. J.*, vol. 54, pp. 985 – 995, 1975.

[57] I. P. Kaminow, "Polarization in Optical fiber," *IEEE J. Quantum Electron.*, vol. QE-17, no. 1, pp. 15 – 22, 1981.

[58] R. M. A. Azzam, and N. M. Bashara, "Ellipsometry And Polarized Light," *NH PL*, 1986.

[59] A. J. Barlow, "Optical-Fiber birefringence Measurement Using a Photo-Elastic Modulator," *J. Lightwave Technol.*, vol. LT-3, no. 1, pp. 135 – 145, 1985.

[60] E. Rochat, *et al.*, "Fiber amplifier for coherent space communication," *IEEE J. Select. in Topics Quantum Electron.*, 2000.

[61] S. C. Rashleigh, and R. Ulrich, "Polarization mode dispersion in single-mode fibers," *Opt. Lett.*, vol. 3, pp. 60 – 62, 1978.

[62] R. J. Mears, *et al.*, "Neodymium-doped silica single-mode fiber lasers," *Electronic letters*, vol. 21, no. 17, pp. 738 – 740, 1985.

[63] M. Shimizu, H. Suda, and M. Horigushi, "High-efficient Nd-doped fiber lasers using direct-coated dielectric mirrors," *Electron. Lett.*, vol. 23, no. 15, pp. 768 – 769, 1987.

[64] J. Morel, "Study of the coherent coupling of fiber lasers by use of an intracavity phase grating," *Thesis, Institue of Microtechnology (IMT), University of Neuchâtel, Switzerland*, 1994.

[65] S. V. Chernikov, J. R. Taylor, and R. Kashyap, "Coupled-cavity erbium fiber lasers incorporating fiber grating reflectors," *Opt. Lett.*, vol. 18, no. 23, pp. 2023 – 2025, 1993.

[66] P. Barnsley, "Fiber Fox-Smith resonators: application to single-longitudinal-mode operation of fiber lasers," *J. Opt. Soc. Am. A*, vol. 5, no. 8, pp. 1339 – 1346, 1988.

[67] J. T. Lin, *et al.*, "Polarization effects in fiber lasers," *Proceedings of European Conference on Optical Communication*, vol. 1, pp. 107 – 112, 1987.

[68] J. T. kringlebotn, *et al.*, "Er^{3+}:Yb^{3+}-codoped fiber distributed-feedback Laser," *Opt. Lett.*, vol. 19, pp. 2101 – 2103, 1994.

[69] S. W. L. vseth, *et al.*, "Fiber DFB Lasers used as Acoustic Sensors in Air," *Appl. Optics*, vol. 38, pp. 4821 – 4830, 1999.

[70] E. Ronnekleiv, "Fiber DFB Laser for Sensor Applications," *Thesis at Norvegian University of Science and Technology (NTNU)*, 1999.

[71] A. D. Kersey, *et al.*, "Fiber Grating Sensors," *J. Lightwave Technol.*, vol. 15, no. 8, pp. 1442 – 1463, 1997.

[72] A. D. Kersey, and W. W. Morey, "Multiplexed Bragg Grating Fiber-Laser Strain-Sensor System with Mode-Locked Interrogation," *Electron. Lett.*, vol. 29, no. 1, pp. 112 – 114, 1993.

[73] O. Hadeler, *et al.*, "Polarimetric Fiber Distributed Feedback Laser Sensor for Strain and Temperature Measurement," *Appl. Optics*, vol. 38, pp. 1953 – 1959, 1999.

[74] J. T. Kringlebotn, W. H. Loh, and R. I. Laming, "Polarimetric Er^{3+}-Doped Fiber Distributed-Feedback Laser Sensor for Differential Pressure and Force," *Opt. Lett.*, vol. 21, no. 22, pp. 1869 – 1871, 1996.

[75] Y. Namihira, M. Kudo, and Y. Mushiaka, "Effect of Mechanical Stress on the Transition Characteristics of the Optical Fibers," *Trans. IECE Jpn.*, vol. 60-C, no. 107, 1977.

[76] A. D. Kersey, and W. W. Morey, "Multielement Bragg Grating based Fiber-Laser strain sensor," *Electron. Lett.*, vol. 29, pp. 964, 1993.